MECHANICAL TEXTURING OF MICROPOROUS SURFACES TO ENHANCE POOL BOILING HEAT TRANSFER

A Dissertation
Presented to
The Academic Faculty

by

Minseok Ha

In Partial Fulfillment
of the Requirements for the Degree
Doctor of Philosophy in the
George W. Woodruff School of Mechanical Engineering

Georgia Institute of Technology
May 2018

MECHANICAL TEXTURING OF MICROPOROUS SURFACES TO ENHANCE POOL BOILING HEAT TRANSFER

Approved by:

Dr. Samuel Graham, Advisor
School of Mechanical Engineering
Georgia Institute of Technology

Dr. Dennis Hess
School of Chemical & Biomolecular Engineering
Georgia Institute of Technology

Dr. Yogendra Joshi
School of Mechanical Engineering
Georgia Institute of Technology

Dr. Jacopo Buongiorno
Nuclear Science and Engineering
Massachusetts Institute of Technology

Dr. S. Mostafa Ghiaasiaan
School of Mechanical Engineering
Georgia Institute of Technology

Date Approved: [March 23, 2018]

ACKNOWLEDGEMENTS

I would like to thank my thesis advisors Dr. Samuel Graham for taking the time to guide me through my graduate research. I would also like to thank my thesis reading committee, Dr. Yogendra Joshi, Dr. S. Mostafa Ghiaasiaan, Dr. Dennis Hess, and Dr. Jacopo Buongiorno for their guidance and expertise. I would also like to thank my fellow graduate students for their warm friendships. I would also like to thank my family who has helped support me through all these years at Georgia Tech.

TABLE OF CONTENTS

LIST OF TABLES

LIST OF FIGURES

SUMMARY

Boiling heat transfer is one of the most promising solutions for the thermal management of systems that require high heat flux removal, presenting orders of magnitude higher heat transfer coefficient than forced liquid convection. Two important aspect of boiling heat transfer is critical heat flux (CHF) and heat transfer coefficient (HTC), and increasing CHF and HTC has been a subject of research for several decades. One of the highest CHFs is seen with microporous surfaces among various surface features, however, there is a tradeoff between CHF and HTC with respect to the microporous coating thickness. The thick coatings show an increase in CHF and a decrease in HTC while the thin coatings show opposite trend. For that reason, optimal coating thickness has been studied, which maximizes HTC, to be 2-4 times of particle diameter for the coatings sintered with spherical particles. Nonetheless, since the optimal thickness has relatively low CHF compared to thick microporous coatings, maximizing both CHF and HTC using the microporous surfaces is investigated in this study. This is conducted through experimental investigation of pool boiling characteristics on microporous surfaces for DI water by leveraging the theories from previous studies. After then, a better understanding on boiling mechanism of the microporous surfaces is provided.

Firstly, plain microporous surfaces are studied, which have a uniform coating thickness without patterns. The present experimental data with variation of the coating thickness are compared to previous theories—viscous-capillary model as well as hydrodynamic instability model, however, none of them properly predicts the CHF. The viscous-capillary model predicts the heat flux that initiates vapor layer in the microporous

coatings, which is frequently confused with CHF. Therefore, we define it as the vapor-layer heat flux to distinguish it from CHF. The hydrodynamic instability model predicts the upper limit of CHF, which is enabled by the modulation of the vapor-jet through pores. Through the analysis using a thermal resistance model, it is shown that vapor layer forms and grows in the microporous coatings, inducing large thermal resistance and degrading the HTC with increased heat flux. The CHF on the microporous surfaces practically occurs by the dry out of the microporous coatings since the modulation of vapor-jets through the pores does not occur anymore as the vapor fills the microporous coatings. The optimal thickness is thought to be the maximum thickness that does not hold the vapor layer in it.

The vapor layer removal was studied by fabricating straight vapor channels in the microporous coatings. A parametric experimental study shows that both CHF and HTC are enhanced by increasing the channel depth as well as by decreasing the channel pitch. The maximum enhancement is achieved to be 3547.5 kW/m^2 in CHF and 89.9 $kW/(m^2K)$ in average HTC for DI water at 50 kPa, increasing the CHF by 347 % and the average HTC by 307 % compared to those of the flat surfaces. Nonetheless, the characteristics of the vapor-layer growth are seen in the boiling curve even with the channel fabrication. Viscous-capillary analysis shows that the vapor-layer growth is caused by the pressure drop of vapor flow through pores as well as by the acceleration pressure drop due to phase change, which were not considered in previous studies. Enhanced structures are suggested to achieve a further enhancement in HTC by preventing the vapor-layer growth, which is done by fabricating additional vapor channels in the solid surfaces beneath the microporous coatings. No sign of the vapor-layer growth is seen with the enhanced structure, validating the analysis.

Although the hydrodynamic instability analysis is believed to provide the upper limit of CHF, a comparison between the theory and the experiment with the straight vapor channels is not available since the wavelength of the vapor-jet is not well defined. Therefore, investigation of the hydrodynamic instability limit is conducted using hole-type vapor channels. Also, a triangular unit cell is suggested through understanding of Zuber's model, which theoretically increases the CHF by 15.5% compared to a conventional square unit cell. It is experimentally shown that the hydrodynamic instability limit is achievable using optimal hole size, which develops a proper wavelength in the view of hydrodynamic instability as well as prevents the vapor-layer growth in the view of viscous-capillary flow. The optimal hole size is determined to be 1.65 mm for the pitch of 2.4 mm in this study, and the enhancement is achieved to be 3802.7 kW/m^2 in CHF and 175.3 kW/m^2K in average HTC for DI water at 1 atm, increasing the CHF by 265 % and the average HTC by 426 % compared to those of the flat surfaces respectively. A triangular unit cell manifests its effectiveness by presenting the experimental CHF that exceeds the limit of the conventional model by 12 %. Also, the experimental value only shows 3 % discrepancy with the model using a triangular unit cell, therefore, the hydrodynamic instability limit is believed to be reached.

Hysteresis in boiling curve of microporous surfaces with respect to heat flux is caused by the vapor-layer growth, which degrades HTC when the heat flux decreases. Since the power fluctuates rather than monotonically increases in practical cooling application, the removal of the vapor layer is critical to prevent the degradation in HTC during a decrease in the heat flux. The wettability of the microporous surfaces has an insignificant effect on the boiling characteristics, but a further investigation is required to

help understanding. The Bond number analysis shows that the vapor-layer growth typically occurs regardless of the working fluid type during boiling heat transfer on the microporous surfaces.

CHAPTER 1. INTRODUCTION

Thermal management of the high power electronics has become more challenging with continued increases in functionality and power density. With this rapid growth of electronic technologies, conventional cooling techniques have severely limited the design and form factor of devices in order to accommodate thermal management solutions especially when there is a need to handle high heat fluxes. In general, high heat flux removal requires the application of efficient heat spreading or high convective heat transfer coefficients that can minimize the temperature rise in the samples. To this end, two phase cooling is one of the most promising solutions to address the need for high heat flux cooling as it provides convective heat transfer coefficients in excess of 100 kW/(m^2K), which is orders of magnitude larger than single phase liquid convection [1] due to the latent heat of vaporization of the heat transfer fluid. Because of such a high heat transfer coefficient, the techniques like pool boiling are already widely used in a variety of industrial applications such as heat exchangers, power generation, and cooling of high-power electronics.

1.1 Pool Boiling

Pool boiling refers to the process in which the heating surface is submerged in a large body of stagnant liquid and the relative motion of vapor bubble and its surrounding liquid is primarily due to the buoyancy effect of vapor [2]. The characteristic of boiling heat transfer is typically represented by the plot of heat flux as a function of superheat, also known as boiling curve. The superheat, ΔT, indicates the temperature of the heater surface that exceeds the saturation temperature of the working fluid. Typical boiling curve for

water at 1 atm is shown in Figure 1, and different boiling regimes may be delineated as free convection, nucleate boiling, transition boiling, and film boiling [1].

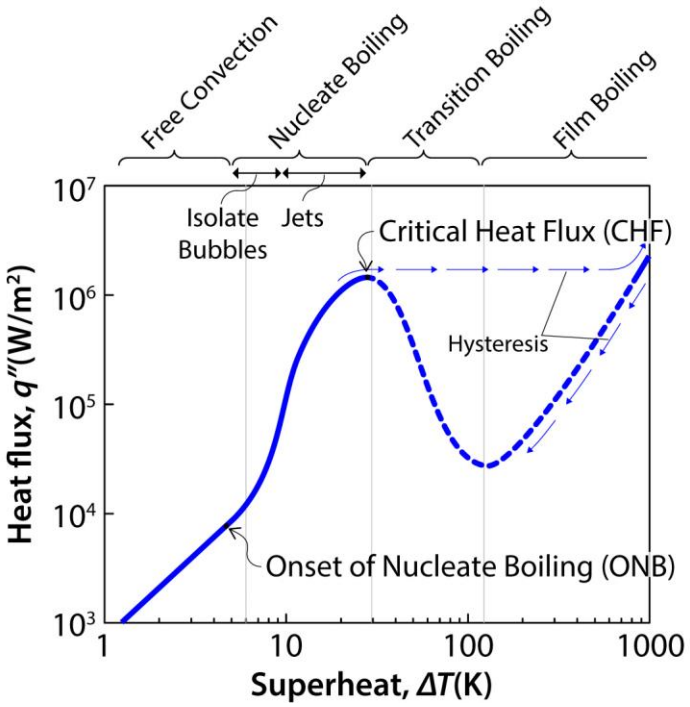

Figure 1 – Typical boiling curve for water at 1 atm. This figure is reproduced from the reference [1].

One important aspect of boiling heat transfer is the critical heat flux (CHF), which is the largest heat flux during nucleate boiling before advancing to transition and film boiling. After this point a vapor blanket is formed on the heater surface that causes a drastic increase in the temperature of the heater surface along the hysteresis curve. For that reason, thermal management systems incorporating boiling heat transfer is required to operate at a heat flux much lower than CHF in order to prevent the catastrophic system failure. Another important aspect is the boiling heat transfer coefficient (HTC) which is the ratio of heat flux to superheat. For thermal management, it is desired to obtain a low superheat to maximize HTC and to limit device junction temperature. Thus, methods to enhance pool

boiling heat transfer have been the subject of research for several decades. While the physical mechanisms of boiling heat transfer are still not understood well, experimental studies have shown that the enhancement in boiling heat transfer can be achieved by the modification of the heater surface characteristics [3] as well as of the working fluid properties [4, 5]. Recent studies are focused on the modification of the heater surface characteristics because the working fluids are frequently determined by the specific application as well as because the boiling heat transfer can be significantly enhanced by the surface modification.

1.1.1 Boiling Heat Transfer Enhancement with Surface Modifications: Experiments

Surface modification for boiling heat transfer enhancement includes roughness [6-8], wettability [7, 9-11], nanostructures [8, 12-14], microstructures [15-17], and hierarchical structures [18-21] that are any combination of those modifications. While heat transfer coefficient is also very important aspect of the boiling heat transfer, most studies have focused on CHF only. This is because the convective coefficient of the boiling heat transfer is already higher than that of forced liquid convection, and because only a rough comparison is possible since the large uncertainty is introduced in estimating the heat transfer coefficient. The result of some recent experimental studies on CHF enhancement for water by surface modification is shown in Figure 2. The studies on surface roughness, wettability, and nanostructures are categorized into the same group since the effect of them is difficult to isolate. The square symbol represents the experiments with flat horizontal heaters while the circle symbol does the experiments with wire heaters. The normalized enhancement was computed as the ratio of the measured experimental CHF to a reference CHF. A reference CHF was obtained from Zuber's correlation [22] for the flat heaters, and

from the experimental results for the wire heaters. The surface modification presented an enhancement in CHF by 1.4 to 3.2 times compared to that of the flat surfaces, and generally microstructures and hierarchical structures show a larger enhancement than nanostructures or changes in wettability.

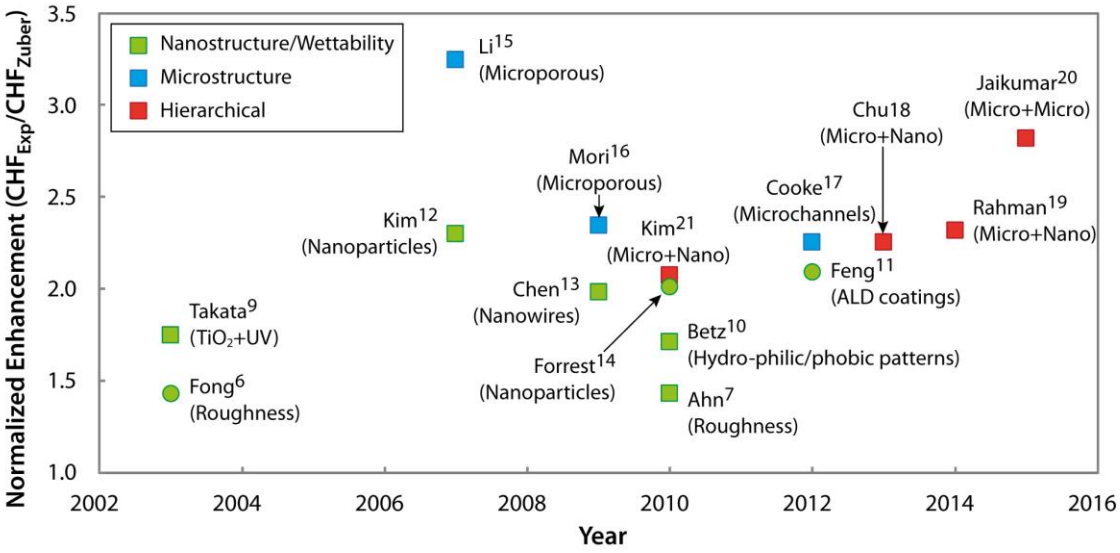

Figure 2 – Some recent experimental studies on CHF enhancement for DI water through the heater surface modification. Studies [6, 7, 9-21] are referenced.

Nanostructures have been intensively studied over a decade not only in boiling heat transfer but also in many other fields. While early studies presented that nanofluids [23-25] enhances CHF significantly, Kim *et al*. [26] revealed that the nanoparticle deposition is the main reason of the CHF enhancement, which occurs during boiling for nanofluids. Kim *et al*. [12] also conducted a detailed study using nanoparticles, and concluded that the enhancement was achieved due to the increase in surface wettability and capillarity, presenting a CHF of 2550 kW/m^2. All the results introduced in this chapter are for DI water at 1 atm unless otherwise specified. Chen *et al*. [13] presented an enhancement in CHF to a level of 2200 kW/m^2 using nanowires fabricated with Si and Cu. Forrest *et al*. [14]

employed stable nanoparticle coatings utilizing a layer-by-layer (LbL) assembly technique, presenting 1735 kW/m^2 in CHF. The wettability of the surfaces also affects the boiling characteristic: Jo *et al*. [27] reported that hydrophilic surfaces cause a delay in the onset of nucleate boiling (ONB) and an increase in CHF while hydrophobic surfaces show an opposite trend. Takata *et al*. [9] presented that superhydrophilic TiO_2 surfaces activated by UV light enhance CHF up to 1940 kW/cm^2. Betz *et al*. [10, 28] showed that the selective coatings on the heater surfaces with hydrophilic and hydrophobic patterns enhance CHF up to 1900 kW/m^2, observing that the bubble nucleation and growth mostly occurs on the hydrophobic surface and the bubble departure size is affected by the patterns. Feng *et al*. [11] employed Al_2O_3 coating using atomic layer deposition (ALD), and showed that increases CHF as the coating thickness increases up to 20 nm, achieving a value of 1200 kW/m^2. Nanostructures alter the roughness and the wettability of the surfaces, and often accompany nanoporosity as well. Since it is not clear which characteristic plays major roles in the enhancement, O'Hanley *et al*. [8] conducted a study to separate the effects of wettability, porosity, and roughness on the CHF. They concluded that the wettability has little effect and the wettability combined with nanoporosity has the large effect while the surface roughness has no effect on CHF within the limit of their experimental data, presenting a value of 1617 kW/m^2 for the nanoporous hydrophilic coatings.

One of the highest CHF enhancements has been reported by Li and Peterson [15] to a level of 3600 kW/m^2 using microporous surfaces that were fabricated by sintering a copper wire mesh (56μm in wire diameter). They conducted a parametric study in terms of coating thickness as well as porosity and pore size of the mesh. Among them, the coating thickness shows an obvious trend that CHF increases and HTC decreases with an increased

coating thickness. Thus, maximizing both CHF and HTC has not been observed. Mori and Okuyama [16] presented the CHF enhancement using porous plates that have an array of holes by attaching it to the heater surfaces, up to 2500 kW/m^2. Cooke and Kandlikar [17, 29] presented an enhancement in CHF using microchannels to be 2690 kW/m^2. Ramaswamy *et al*. [30-32] and Ghiu and Joshi [33] conducted experimental studies using porous surfaces created by an array of rectangular channels for dielectric fluid and showed that the bubble departure size is related to the enhancement.

The combination of surface modifications, also known as hierarchical structures, such as nanostructures on microstructures is of interest for further improvement of boiling heat transfer. Launay *et al*. [34] studied microchannels coated with carbon nanotubes (CNTs) for PF5060 and DI water, and observed an enhancement in HTC at low heat flux. McHale *et al*. [35] studied microporous surfaces coated with CNTs, and reported an enhancement in CHF by 45% for HFE-7300 while no enhancement for DI water. Rahman *et al*. [19] studied microposts coated with nanostructures by biotemplating, and reported an enhancement in CHF up to 2570 kW/m^2. Dhillon *et al*. [36] studied micropillars coated with nanograss, and reported an enhancement in CHF up to 2000 kW/m^2. Jaikumar *et al*. [20] presented an enhancement in CHF to be 3130 kW/m^2 using microchannels coated with microporous layers.

Overall, the experimental studies have presented that a large enhancement can be achieved by surface modification using microstructures, nanostructures, and coatings that enhance fluid-surface interactions through increased wettability. Moreover, hierarchical surfaces may induce a further enhancement. Nonetheless, not many studies are available

on the physical mechanism of the boiling characteristics, which is essential for further enhancement. We will review them in the next subsection.

1.1.2 An Enhancement with Surface Modifications: Theory

The efforts to understand the physics of boiling and its impact on CHF and HTC have been a subject since the beginning of the pool boiling study. The conventional hydrodynamic instability model [22, 37], also known as Zuber's correlation, explains CHF well for flat surfaces in terms of working fluids, given as Eq.1.1:

$$q''_{CHF} = K \times h_{fg} \rho_v^{1/2} \left[\sigma g \left(\rho_l - \rho_v \right) \right]^{1/4} \qquad \text{(Eq.1.1)}$$

where K is $\pi/24$ or 0.131 by Zuber's derivation, h_{fg} is latent heat of vaporization, ρ is density, σ is surface tension, g is gravitational acceleration, and the subscripts, l and v, denote liquid and vapor phase, respectively. For water at 1 atm, Zuber's correlation predicts CHF = 1107.5 kW/m^2. Lienhard and Dhir [38] presented the correlation to predict CHF with respect to the shape and the size of heater by modifying Zuber's correlation. However, Zuber's correlation does not account for the surface characteristics since Eq.1.1 is a function of the working fluid properties.

Kandlikar [39] developed the CHF model that account for the wettability (or the contact angle). The correlation was derived using vapor momentum analysis, resulting in the same form as Eq.1.1 but different K value as Eq.1.2:

$$K = \left(\frac{1+\cos\beta}{16} \right) \left[\frac{2}{\pi} + \frac{\pi}{4} \left(1+\cos\beta \right) \cos\psi \right]^{1/2} \qquad \text{(Eq.1.2)}$$

where β is the receding angle and ψ is the inclination angle of the surface (i.e., ψ = 0 for a horizontal upward facing surface). The CHF prediction as a function of the receding contact angle, β, is shown in Figure 3 for a horizontal surface (ψ=0) for water at 1 atm. The model generally agrees with the experimentally reported values in that hydrophilic surfaces presents high CHF and that hydrophobic surfaces does low CHF. However, the model cannot capture the effect of the structured surface that presents very low apparent or no measurable contact angle.

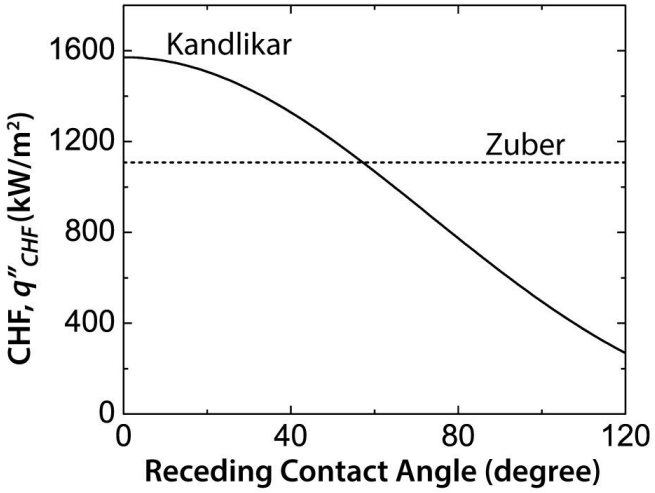

Figure 3 – CHF prediction as a function of receding contact angle by Kandlikar [39] for water at 1 atm. A horizontal surface (ψ=0) was assumed, and Zuber's prediction is referenced.

The refined model was suggested by Chu *et al*. [40] with the consideration of surface features given as Eq.1.3:

$$K = \left(\frac{1+\cos\beta}{16}\right)\left[\frac{2\left(1+r\cos\theta\right)}{\pi\left(1+\cos\beta\right)} + \frac{\pi}{4}\left(1+\cos\beta\right)\cos\psi\right]^{1/2} \qquad \text{(Eq.1.3)}$$

where β is the apparent contact angle, θ is the receding contact angle on the corresponding smooth surface, and r is the roughness ratio. The model explains the effect of the surface

roughness especially when the receding contact angle, β, approaches 0, which is typically shown in microstructures with superhydrophilic coatings. Chu's correlation predicts that CHF monotonically increases as the density of the surface increases. However, Dhillon *et al*. [36] reported that the optimal density of the surface microfeatures exists to enhance the CHF through the experimental and the theoretical study.

Among a variety of explanations to understand the enhancement using surface features, the explanation that the CHF enhances via capillary wicking has been widely discussed recently [19, 36, 41]—the rapid rewetting of the heater surface after bubble departure delays the vapor layer formation on the heater surfaces and increases CHF. A wickability model was suggested by Rahman *et al*. [19] by relating the wicking (or liquid imbibition) characteristic to the CHF as given Eq.1.4:

$$q''_{CHF} = q''_{CHF,Zuber}\left[1+\frac{\dot{V}''_o\rho_l}{\rho_l^{1/2}\left[\sigma g\left(\rho_l-\rho_v\right)\right]^{1/4}}\right] \qquad \text{(Eq.1.4)}$$

where $q''_{CHF,Zuber}$ is the CHF estimated using Zuber's correlation in Eq.1.1. $\dot{V}_o''$ is the wicked volume flux determined experimentally by measuring the flow of liquid from a capillary tube onto the textured surface [19, 41]. The model stats that CHF increases as the wicked volume flux increases. However, the model relies on experimental data and no physical mechanism was provided although analytical estimation of the wicked volume flux is available for the simple parametric textures [3].

Dhillon *et al*. [36] proposed a coupled thermal-hydraulic model by postulating that the CHF occurs when a heating time scale is smaller than a rewetting time scale. The model

explains the effect of surface texture density on CHF, presenting the existence of maxima in CHF enhancement. Figure 4 shows the CHF as a function of the surface microfeature density: Micropillars of 10 μm width and 12.75 μm height were used, and the spacing between the micropillars was varied. The enhancement was maximized around the spacing of 20 – 30 μm according to Dhillon *et al.*'s study while Chu's correlation predicts a monotonic increase in CHF with a decreased micropillar spacing. The study also presented that the nanograss fabrication on the microfeatures results in additional enhancement in CHF.

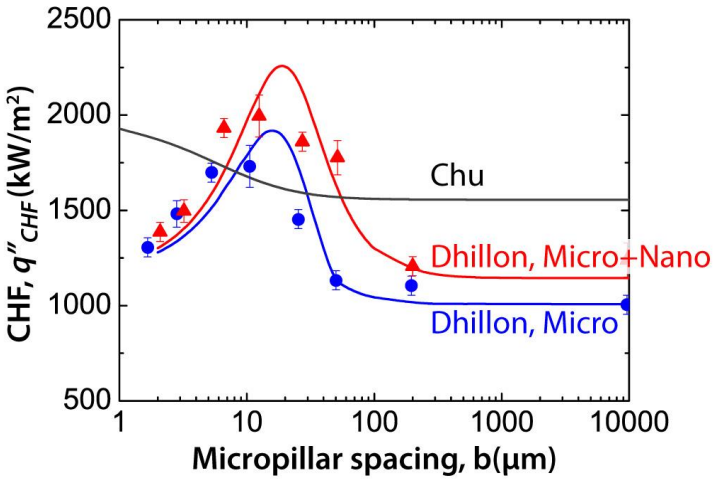

Figure 4 – CHF as a function of the density of the surface microfeatures. The lines represent the models and symbols represent the experimental data. Chu's model [40] was computed using Eq.1.3, and Dhillon's model and data were reproduced from the reference [36].

So far, the following constitutes a generally accepted understanding of boiling enhancement: High wettability (or small contact angle) enhances CHF while it slightly lowers HTC. CHF is enhanced as surface roughness increases, but optimal density exists that maximize CHF. Liquid imbibition (or wickability) plays an important role to enhance CHF, which can be improved using nanoporosity. While the physical mechanisms of the

nanostructures, roughness and wettability on the CHF enhancement have been actively studied, the mechanism of the microstructures, typically larger than tens of microns, is one of the least understood areas. For the microchannels, no correlation exists to predict CHF although the enhancement is believed due to the extended surface as well as the increased nucleation sites provided by the channel fabrication [29]. For microporous surfaces, two different studies are available to predict CHF through the analysis of the viscous-capillary flow [42, 43] and hydrodynamic instability [44]. The details of the studies will be reviewed in Chapter 3.

1.2 Objective and Organization of Thesis

Microporous coatings are widely used in the application to the cooling of high power electronics such as heat pipes and vapor chambers due to their superior wicking characteristic. Also, one of the highest CHFs ever reported [15, 45] is very attractive for the pool boiling application such as direct immersion cooling. However, microporous surfaces may also induce a very large surface superheat (>100°C) which is not desirable for the cooling application. While the understanding of the CHF is key to enhancing boiling heat transfer, a comprehensive understanding is not yet available. The objectives of this study are to explore the critical factors that govern the enhancement in pool boiling on the microporous surfaces and to augment theoretical approaches to help capture these effects in microporous surfaces. Experimental investigation of the boiling curve for DI water will be conducted with the microporous surfaces sintered using spherical copper powder. The results will be compared with the existing theories, and a better understanding will be provided by combining those theories. Based on the understanding, the enhanced structures will be suggested, which present an increase in CHF and a decrease in surface superheat.

The thesis is organized into 8 chapters. Chapter 1 presents a brief overview of pool boiling heat transfer and the boiling heat transfer enhancement through the heater surface modification. The experimental method is given in Chapter 2, and the boiling mechanism on the plain microporous surfaces is studied in Chapter 3. Based on the understanding, an enhancement is studied in Chapter 4 and Chapter 5 by patterning the plain microporous surfaces. Chapter 4 presents the patterns using straight channels and provides an analysis in the view of the viscous-capillary flow. Chapter 5 presents the patterns using hole channels, more focusing on the hydrodynamic instability. Through Chapter 3 and Chapter 5, a detailed background of the existing theories and experimental efforts are given in the beginning of each chapter, followed by the present experimental results and discussions. Chapter 6 presents other important aspects of the boiling characteristics of microporous surfaces such as the effect of wettability change. Lastly, Chapter 7 provides conclusions and outlines proposed future work.

CHAPTER 2. METHODS

In this chapter, we provide a description of how our reference microporous samples were fabricated and tested. Uncertainties in the measurements were taken into account, but discussed in detail in the appendix B and referenced in this chapter where appropriate.

2.1 Sample Fabrication and Characterization

Microporous surfaces were fabricated by sintering copper powder (Alfa Aesar, 11070, spherical, -100 mesh, 99.5% purity) on a copper substrate (OFHC, 2 cm^2 circular disk). The powder was used after sorting to a range of 125 – 150 μm in diameter with sieves (-100+120 mesh). The copper substrate and powder were placed in a graphite mold, and sintering was performed in a vacuum furnace (<10 mTorr) using the temperature and gas profile shown in Figure 5. The vacuum was released after the sample was cooled down to 30°C to prevent oxidation.

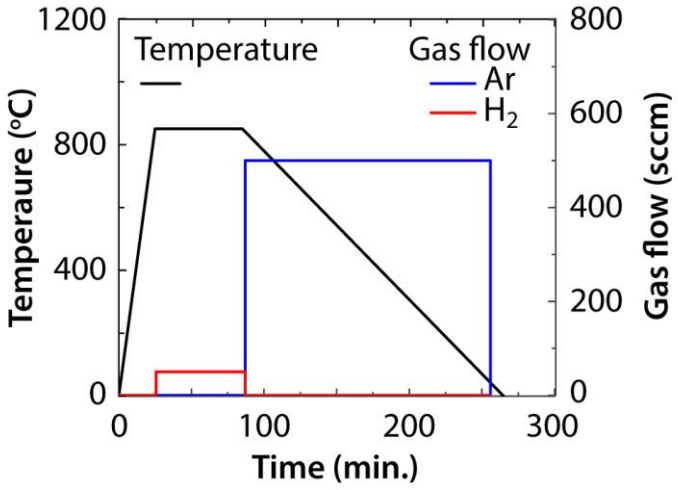

Figure 5 – The temperature and the gas flow profile of the sintering process.

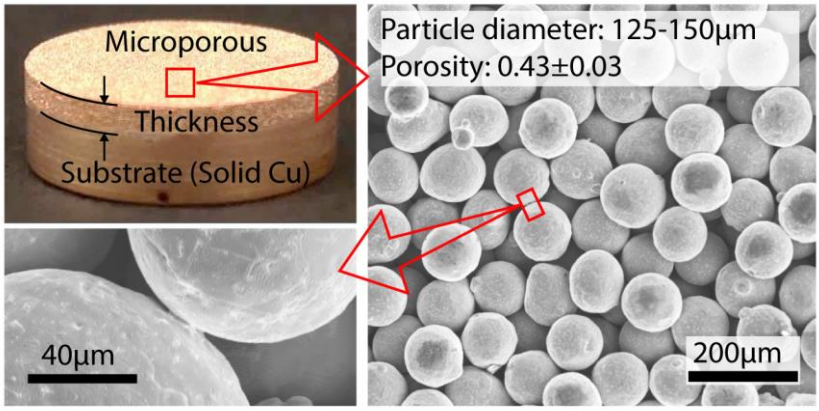

Figure 6 – A sample image of 1.5 mm thick microporous coating and SEM images of the sintered copper powder.

A sample of 1.5 mm microporous coating thickness is shown in Figure 6. The average neck diameter between the particles was measured to be 5 – 10 μm. The porosity, ε, was estimated to be 0.43 ± 0.03 using the mass and the volume of the microporous coatings by Eq.2.1 and Eq.2.2:

$$\varepsilon = 1 - \frac{\rho_{Porous}}{\rho_{Cu}} \qquad \text{(Eq.2.1)}$$

$$\rho_{Porous} = \frac{4m_{Porous}}{\pi d^2 \delta} \qquad \text{(Eq.2.2)}$$

where m_{Porous} is the mass of the microporous coatings or the mass of the powder used in the sintering, d is the sample diameter, and δ is the thickness of the microporous coating, and ρ_{Cu} is the copper density, 8.96 g/cm^3. The uncertainty of the porosity was computed by the propagation of the measurement uncertainties: namely the uncertainties of the powder mass, the diameter of the microporous coatings, and the thickness of the microporous coatings. The details of the uncertainty analysis are shown in Appendix B.1. The thermal conductivity of the microporous coating, k_{eff}, was measured by a steady-state method using

a one-dimensional reference bar, which was designed based on ASTM E 1225-87 (see Figure 7). The thermal conductivity was estimated by the heat flux and temperature gradient across the sample to be around 40 W/(mK). A sample of the microporous coating without a copper substrate was fabricated and used for the measurement. A constant pressure, 650 kPa, was applied to reduce contact resistance, and no additional attempt was made to correct for contact resistance.

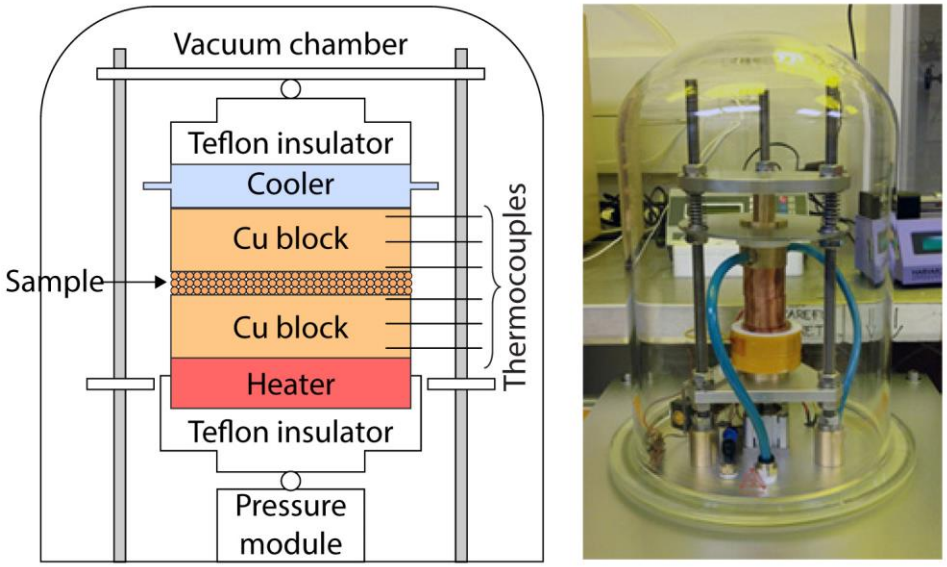

Figure 7 – A schematic and picture of the experimental setup for the thermal conductivity measurement.

2.2 Pool Boiling Experiment

2.2.1 Experimental Setup

A stainless-steel pool boiling chamber was built that was sealed with O-rings as shown in Figure 8, which allows the experiment for a variety of working fluids at different saturation pressure. DI water was used for the working fluid in this study. Saturation conditions were attained by controlling the temperature and the pressure of the chamber

using immersion heaters, a heat exchanger, and a pressure regulator (solenoid valve) that is connected to a vacuum pump. The pressure inside of the chamber was maintained within ± 0.2 kPa throughout the experiment, being monitored using a pressure transducer. Also, the temperature of the working fluid near the sample was maintained within ± 0.1°C while the temperature of the entire working fluid was maintained within ± 1°C, being monitored using three thermocouples.

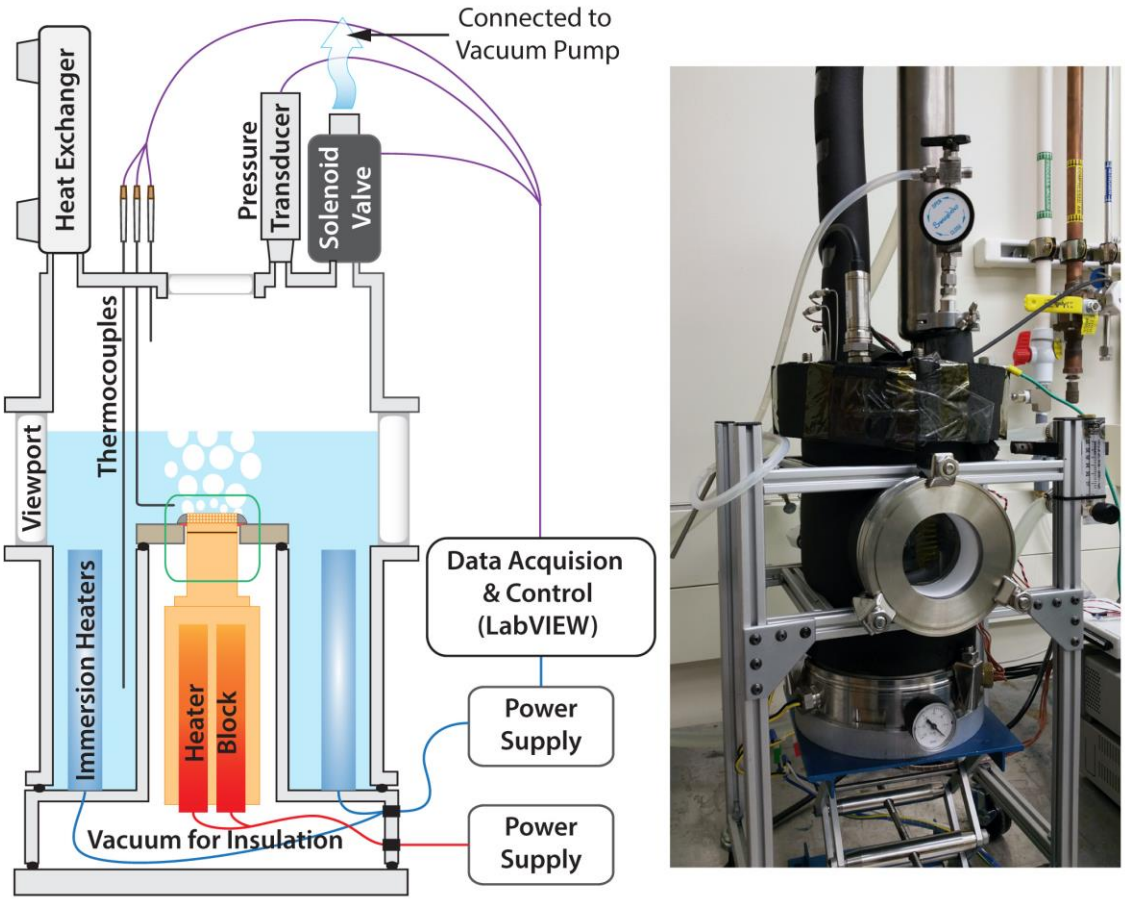

Figure 8 – A schematic and a picture of the pool boiling experimental setup.

Heat flux was generated using a copper block with cartridge heaters, and one-dimensional heat flux was obtained through a copper rod (OFHC, 2cm^2 of heat flux area) mounted on the heater block. The enclosure of the heater block was evacuated to low

vacuum (< 1 kPa) to prevent convection heat loss. The view ports were placed in front and rear of the chamber for the visual observation as well as the high-speed imaging of the bubble growth and departure. The system control and the data acquisition were performed using a National Instruments DAQ system and LabVIEW software. The calibration of the thermocouples was performed periodically using OMEGA CL122 Block calibrator while the pressure transducer was used as calibrated by the vendor.

2.2.2 Experimental Procedure

A sample was mounted on the copper rod using Ga-In-Sn liquid metal as a thermal interface material (TIM) as shown in Figure 9. Shear slip of the sample was prevented by wrapping the sample and the copper rod together with Kapton tape. The sample was surrounded by the PEEK lid and the gap was sealed with Epoxy and RTV sealant. Although the liquid metal is slightly corrosive to copper, it does not affect the heater surface and the experiment due to the sealing.

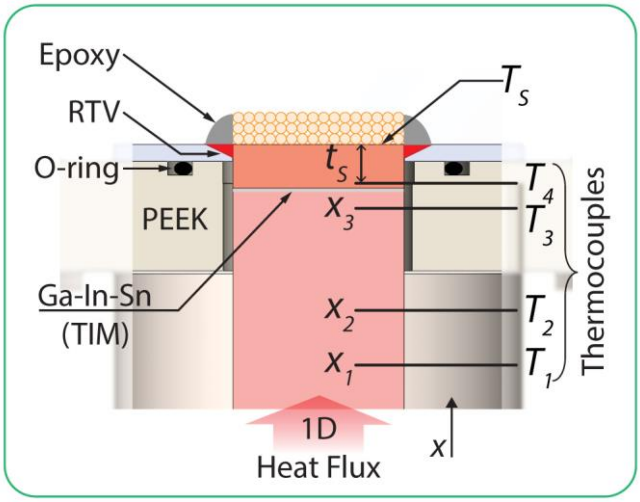

Figure 9 – A schematic of the mounted sample.

After the installation of the sample, the chamber was evacuated first and then filled with DI water. The degassing of DI water was conducted in the chamber by boiling it from low pressure (< 5 kPa) to above the atmospheric pressure with frequent release of the vapor. During the degassing process, the heat flux was also applied to the sample until nucleate boiling occurs to remove the trapped air that may exists on the surface. After this procedure, the inside of the chamber was maintained at the saturation temperature and pressure for one hour so that the sample was cooled down and reached steady-state.

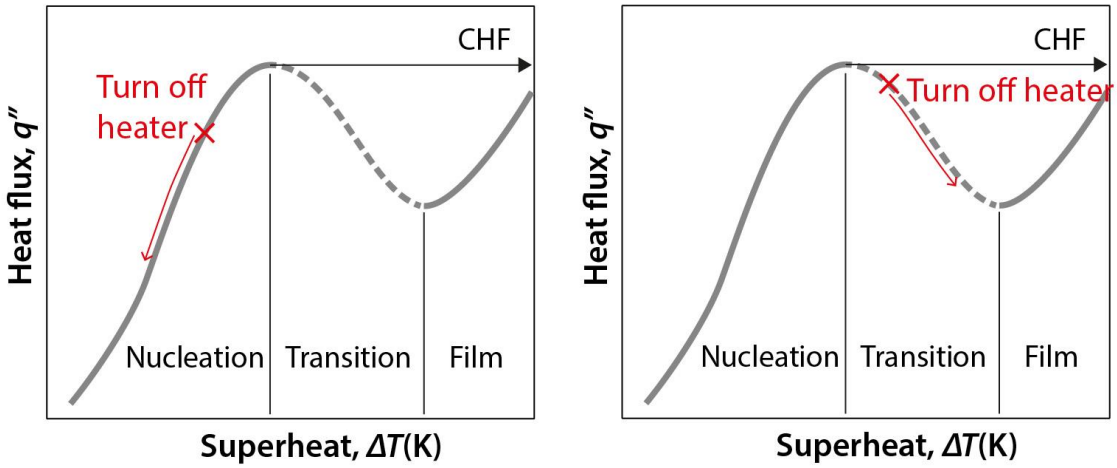

Figure 10 – Experimental determination of CHF.

The experiment was conducted by increasing the heat flux in steps of 50 kW/m^2 with 5-minute interval until CHF was reached. The CHF was determined experimentally with the criterion shown in Figure 10. If the sample heater was turned off during nucleate boiling, the surface superheat decreased with a decreased heat flux. However, if the heater was turned off during transition boiling, the surface superheat increased with a decreased heat flux. Therefore, the CHF was determined to be the largest heat flux during nucleate boiling before advancing to transition boiling. To prevent the failure of the system after

reaching CHF, nitrogen gas was blown to the heater surface to agitate the formation of the vapor film as well as to increase the pressure inside the chamber, and thus the CHF.

2.2.3 Data Reduction

For the estimation of the heat flux through the sample, three T-type thermocouples (0.5 mm in sheath diameter) were placed in the copper rod with 5 – 8 mm spacing, measuring temperatures, T_1, T_2 and T_3 (see Figure 9). With the assumption of one-dimensional heat flux, which is validated by finite element analysis shown in Figure 12, the heat flux can be computed by the simple linear regression analysis as given in Eq.2.3 and Eq.2.4:

$$q'' = -k_{Cu} a \qquad \text{(Eq.2.3)}$$

$$a = \frac{\sum_{i=1}^{n} x_i T_i - \frac{1}{n}\sum_{i=1}^{n} x_i \sum_{i=1}^{n} T_i}{\sum_{i=1}^{n} (x_i)^2 - \frac{1}{n}\left(\sum_{i=1}^{n} x_i\right)^2} \qquad \text{(Eq.2.4)}$$

where k_{Cu} is the thermal conductivity of copper, a is the temperature gradient, x_i is the position of the thermocouple, and T_i is the temperature at the position x_i. n is 3 since the temperature was measured at three positions. For the thermal conductivity of copper, a temperature dependent value was used as shown in Appendix A.1 since the temperature varies from 80°C to over 300°C. For the temperature, 20 data points were taken at the steady-state condition, and the average of them was used. The surface superheat, ΔT, was determined from the temperature at bottom of the microporous coating, T_S, which was estimated from T_4 and the heat flux as shown in Eq.2.5:

$$\Delta T = T_S - T_{sat} = \left(T_4 - \frac{q'' t_s}{k_{Cu}} \right) - T_{sat} \quad \text{(Eq.2.5)}$$

where t_s is a distance from the position of T_4 to the bottom of the microporous coatings, and T_{sat} is a saturation temperature. A heat transfer coefficient, h, was computed by dividing the heat flux by the corresponding superheat as Eq.2.6:

$$h = \frac{q''}{\Delta T} \quad \text{(Eq.2.6)}$$

The uncertainties were computed by the propagation of the measurement uncertainties which were due to the thermocouple reading and thermocouple position as well as the thermal conductivity of copper. The details of the uncertainty analysis are shown in Appendix B.2.

2.2.4 Validation of the Setup and Reference Test

To validate the experimental setup, a pool boiling experiment on a flat copper surface was conducted and compared to the reference values. A flat copper surface was prepared by polishing the surface using Logitech PM5, and the surface characteristics of the sample are shown in Table 1. The experiment was conducted for DI water at three different pressure, 50 kPa, 7 5kPa, and 1 atm. Figure 11 shows the measured boiling curves, and HTC as a function of heat flux for each pressure.

Table 2 compares the present experimental CHFs to those by Zuber's correlation (Eq.1.1). The present experimental result agrees well with Zuber's prediction, presenting less than 6% discrepancy. The experimental CHFs on a flat Cu surface for water at 1atm has been reported [20, 46, 47] to be 1160 – 1497 kW/m^2. The present result is smaller than those values, rather close to the CHFs on Si or SiO_2 surfaces [8, 13, 18], 820 – 1070 kW/m^2. The possible reason is the small surface roughness of the present sample since the CHF decreases as the surface roughness becomes smaller [6, 48].

Table 1 – The surface characteristic of the flat copper sample. The roughness parameters were measured using Olympus LEXT 3D material confocal microscope, and the contact angle using Ramé-hart 250 goniometer.

Surface roughness parameters			Static contact angle
Ra (μm)	***Rq (μm)***	***Rz (μm)***	
0.03 ± 0.01	0.04 ± 0.01	1.0 ± 0.2	80° ± 0.5°

Table 2 – The saturation temperatures of water and CHFs at 50 kPa, 75 kPa, and 1 atm. The present experimental result and Zuber's prediction using Eq.1.1 are compared.

Pressure	T_{sat} (°C)	CHF		
		Experiment (kW/m^2)	Zuber's (kW/m^2)	Discrepancy (%)
50 kPa	81.32	793.2 ± 49.8	827.6	4.2
75 kPa	91.86	947.7 ± 52.4	979.3	3.2
1 atm	100	1042.0 ± 53.8	1107.5	5.9

The experimental results present that CHF and HTC increases as pressure increases. Based on the Zuber's correlation in Eq.1.1, the largest contribution in CHF change with respect to the pressure change is made by the vapor density (or the specific volume of the vapor). Therefore, the increase in CHF at high pressure can be explained by the reduction in the vapor-jet size, which results in the delay in Kelvin-Helmholtz (KH) instability. The details of hydrodynamic instabilities will be discussed in Chapter 3 and Chapter 5.

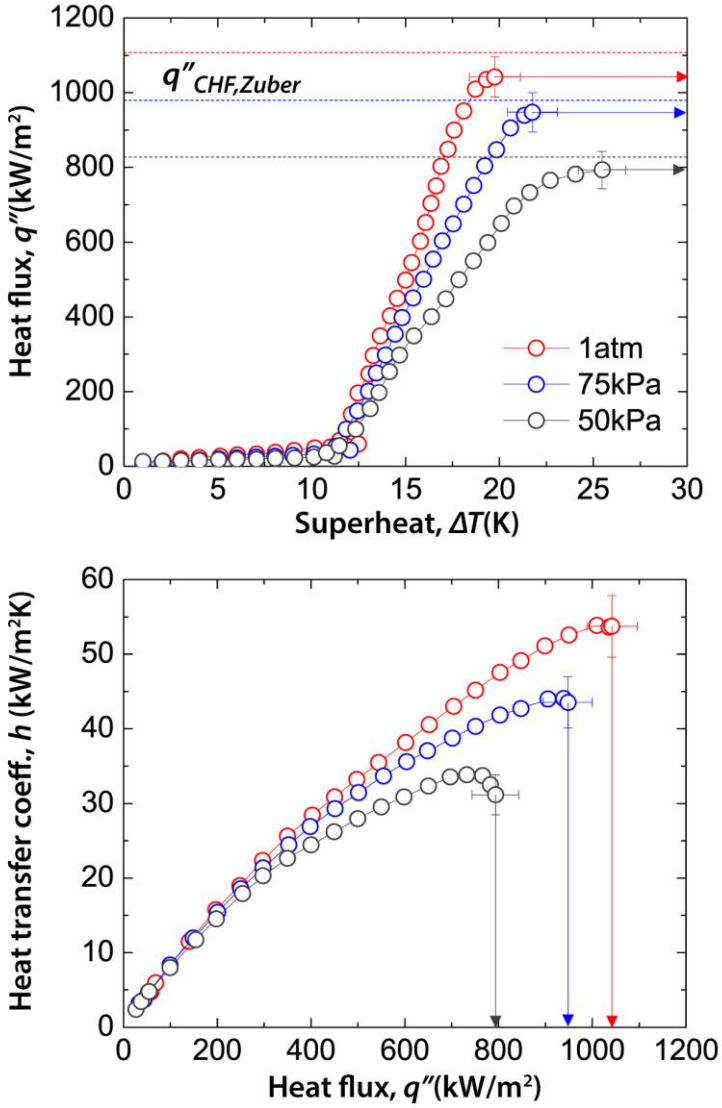

Figure 11 – Boiling curves and HTC of the flat surfaces. The arrows denote that CHF was reached. The dotted lines represent the CHF computed using Zuber's correlation.

For all pressures, ONB occurred at almost the same superheat, around 11 – 12 K. The bubble nucleation typically started from the edge of the sample, which is affected by the sealing of the Epoxy and RTV. However, the nucleation at the edge showed a low frequency of the bubble departure, and therefore has little effect on the boiling curve at high heat flux and CHF. Nonetheless, since it still affects the boiling characteristic around ONB, in this study we will more focus on nucleate boiling and CHF rather than ONB.

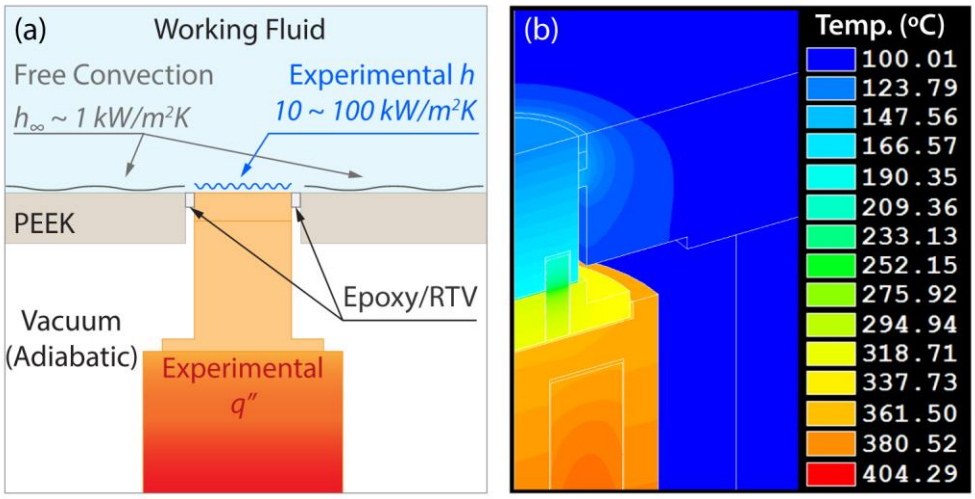

Figure 12 – A simulation to estimate the heat leakage through the Epoxy and RTV sealing: (a) Boundary conditions and (b) a simulation result of a flat surface for DI water at 1 atm using the experimental value of h = 52 kW/(m^{2}K) and q'' = 1042 kW/m^2.

The heat leakage through the contact between the sample and the sealant was estimated by a simplified FEM simulation. The experimental heat flux and HTC were used as boundary conditions. The simulation condition is shown in Figure 12: The sample side was contacted to Epoxy and RTV over the sample perimeter, and the contact width of each material was assumed to be 1.0 mm respectively. A free convection near a forced convection, 1 kW/(m^{2}K), was assumed on the PEEK surface that was exposed to water, and an experimental HTC was applied on the heater surface. The heat flux corresponding to the experimental HTC was applied to the heater rod. A result of the simulation is shown in Figure 12. The heat leakage through the contact was computed to be less than 0.4 % of total heat flux, and therefore, was neglected.

CHAPTER 3. POOL BOILING CHARACTERISTICS OF PLAIN MICROPOROUS SURFACES

In this chapter, we analyze the pool boiling characteristics of the reference microporous surfaces that have uniform thicknesses, which will be called as plain microporous surfaces. These surfaces will be contrasted against microporous surfaces with patterns that will be discussed in Chapter 4 and Chapter 5.

3.1 Background

The physical mechanisms of the surface characteristics on boiling heat transfer have been studied regarding wettability [39], surface roughness [40], and wickability [19]. The optimal density of micropillars was studied through thermal-hydraulic analysis [36]. Despite those previous studies, the boiling characteristics of microporous surfaces are far different from those of the flat surfaces or the solid surfaces with a few microns of pillars, and may not strictly follow the lesson learned from those studies. In general, three different mechanisms have been suggested to explain the nature of CHF in microporous layers, which are given below.

3.1.1 Viscous-Capillary Analysis

Udell [42] as well as Lu and Chang [43] estimated the applied heat flux that initiates the formation of a vapor layer at the bottom of the microporous coating (when heated from bottom). The viscous flow of liquid and vapor phases is related to the capillary pressure to predict the formation of this layer. A one-dimensional viscous-capillary analysis was

conducted by taking the *x* coordinate along the microporous thickness with the origin at the bottom of the microporous coatings (see Figure 13).

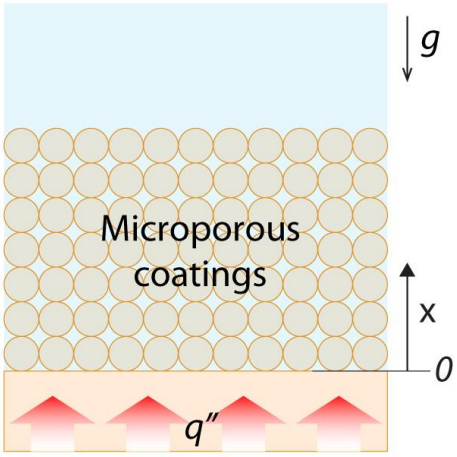

Figure 13 – Geometry used in the viscous-capillary analysis

Assuming that vapor is generated at the bottom of microporous coatings and the liquid and vapor flow is laminar, the pressure drop across the microporous coating is given using Darcy's law as Eq.3.1:

$$-\nabla p = \frac{\mu}{\kappa} u + \rho g \qquad \text{(Eq.3.1)}$$

where p is pressure, μ is dynamic viscosity, κ is permeability, u is velocity, ρ is density, and g is gravitational acceleration. The mass balance between liquid and vapor phase is given as Eq.3.2:

$$\rho_l u_l + \rho_v u_v = 0 \qquad \text{(Eq.3.2)}$$

where the subscripts, *l* and *v*, denote liquid and vapor phase respectively. The heat flux is the energy used in vapor generation, given as Eq.3.3:

$$q'' = \rho_v u_v h_{fg} \quad \text{(Eq.3.3)}$$

where h_{fg} is the latent heat of vaporization. The capillary pressure, p_c, is defined as Eq.3.4:

$$p_c = p_v - p_l \quad \text{(Eq.3.4)}$$

Solving the pressure drop equation of each phase using Eq.3.1, incorporating Eq.3.2 – Eq.3.4 gives the following relationship in Eq.3.5:

$$-\frac{dp_c}{dx} = \frac{q''}{\kappa h_{fg}}\left(\frac{\nu_v}{\kappa_{rv}} + \frac{\nu_l}{\kappa_{rl}}\right) - \left(\rho_l - \rho_v\right) g \quad \text{(Eq.3.5)}$$

where ν is the kinematic viscosity and κ_{rv} and κ_{rl} is the relative permeabilities of the liquid and the vapor. This equation shows that the heat flux that can be sustained in the microporous surface during boiling is a function of permeability and capillary pressure gradient along the coating thickness. The capillary pressure, p_c, and the relative permeabilities, κ_{rv} and κ_{rl}, can be expressed as a function of the relative liquid saturation, *Se*, which is the pore volume occupied by liquid over the total pore volume. The heat flux of the vapor-layer formation is determined by finding the heat flux at which *Se* is 0 at the bottom of the microporous coating (x = 0). The details of the analysis are shown in Appendix C. The point at which the vapor layer formed was referred to be CHF or dryout heat flux in these studies.

Fukusako *et al.* [49] conducted an experiment using packed beds of spherical particles, glass and steel with diameters in the range of 1.1 mm – 16.3 mm for R11 and water, and reported that the shape of the boiling curve was significantly altered with respect to the particle size as the peak of the curve diminishes with the small particles (see Figure

14). Since the heat flux for the small particles monotonically increased over 200°C in their experiment, they stated that that film boiling directly follows nucleate boiling without transition boiling. Kaviany [50] employed the experimental results by Fukusako *et al.* and presumed that the CHF of the microporous surfaces is the heat flux at the slope-change, which is predicted by Udell's correlation. Kaviany also generalized the boiling behavior using the concept of Bond number, *Bo*, which is a dimensionless number measuring the importance of body force to surface tension. We will discuss the effect of Bond number in Chapter 6.3.

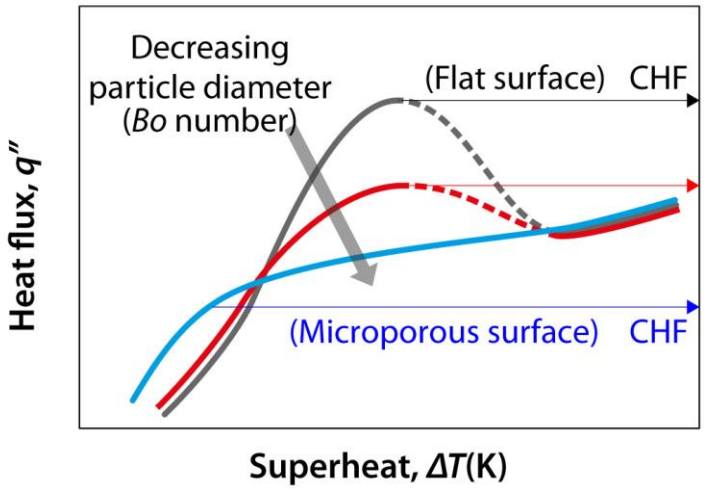

Figure 14 – Effect of the particle size on the boiling curve of packed beds of spherical particles. The curve is depicted based on the experimental results of Fukusako *et al.* [49].

3.1.2 Hydrodynamic Instability Analysis

Polezhaev and Kovalev [44] stated that hydrodynamic instability determines the CHF of microporous surfaces as it does for the flat surfaces. Therefore, they also stated that the CHF is predicted using a modified Zuber's correlation as shown in Eq.3.6:

$$q''_{CHF} = 0.52\varepsilon^{2.28} h_{fg} \left(\frac{\sigma \rho_v}{r_{br}} \right)^{1/2} \quad \text{(Eq.3.6)}$$

where ε is the porosity and r_{br} is the breakthrough radius. Eq.3.6 is valid for the porosity of 0.26 – 0.48. Although the derivation was not clearly explained in their study, it is thought to be derived from the experimental estimation of either the wave length or the vapor-jet diameter on the microporous surfaces. Since the breakthrough radius is determined experimentally, and the value for the present structures is not well known, we will consider the three possible cases: Liter and Kaviany [51] simply assumed that it is a half of the particle diameter, d_p, in Eq.3.7. A half of the hydraulic diameter, $d_h/2$, in Eq.3.8 and the effective radius [52] in Eq.3.9 are also reasonable assumptions.

$$r_{br} \sim 0.5 d_p \quad \text{(Eq.3.7)}$$

$$r_{br} \sim \frac{d_h}{2} = \frac{\varepsilon}{3(1-\varepsilon)} d_p \quad \text{(Eq.3.8)}$$

$$r_{br} \sim r_{eff} = 0.21 d_p \quad \text{(Eq.3.9)}$$

3.1.3 Effect of the vapor layer

Li and Peterson [15] conducted experimental study using sintered wire meshes and presented CHF. They stated that the formation of the vapor layer in microporous coatings plays an important role in the boiling heat transfer on the microporous surfaces. The schematic in their study implies that the CHF is the dryout of the microporous coatings although they did not explicitly state it.

All three explanations account for some aspects of the boiling mechanism on microporous surfaces, however, a full understanding is not yet available. In this study, we

will combine those theories to help explain phenomena in pool boiling on microporous surfaces, leading to a better understanding in how to enhance pool boiling heat transfer.

3.2 Procedure, Result and Discussion

3.2.1 Experiment in Variation of Thickness of Microporous Coatings

Since the viscous-capillary model is a function of the thickness of the microporous coatings while the hydrodynamic instability model is not, an experimental pool boiling study was conducted to compare those two models against samples with different coating thicknesses. Five different thicknesses were examined as shown in Table 3. The samples were fabricated by sintering spherical particles (Cu, 125 – 150 μm in the particle diameter) to be 15.95 cm in the sample diameter (2 cm^2 of the area). The thermal conductivity and the average porosity was measured to be 40 W/(mK) and 0.43 ± 0.03, respectively. The pool boiling experiment was conducted using DI water at 50 kPa (T_{sat} = 81.3°C). The details of the sample fabrication and the experimental procedure is shown in Chapter 2. The CHF was determined as with the criterion shown in Figure 10.

Table 3 – The sample specification and the uncertainties. U_ξ is the measurement uncertainty of ξ.

Sample	Diameter $d_s \pm U_{ds}$ (mm)	Thickness $\delta \pm U_\delta$ (mm)	Mass $m_s \pm U_{ms}$ (g)	Porosity, ε
2.0mm Porous	15.95 ± 0.05	1.95 ± 0.05	2.000 ± 0.020	0.43 ± 0.02
1.5mm Porous	"	1.47 ± 0.05	1.500 ± 0.020	0.43 ± 0.02
1.0mm Porous	"	0.98 ± 0.04	1.000 ± 0.020	0.43 ± 0.03
0.5mm Porous	"	0.49 ± 0.03	0.500 ± 0.020	0.43 ± 0.04
0.3mm Porous	"	0.30 ± 0.02	0.300 ± 0.020	0.43 ± 0.05

While the vapor escape through the side of the microporous coatings was dominant in the previous study [15], the vapor escape through the thickness of the microporous coatings is noticeable in the present study. The discrepancy is believed due to the difference in the sample size—2 cm^2 in the present study and 0.64 cm^2 in the previous study, which is related to the length of vapor-flow path. In this study, the side of the microporous coating was sealed to mimic an infinite microporous surface. While all samples were prepared and installed through the same procedure, the boiling characteristics varies from sample to sample due to the random packing of the particles. In this study, we tested more than three samples for each case to ensure the trend were correct and used a representative result in the analysis. An example of the raw data is shown in Appendix D.

The experimental result of the microporous surfaces with different coating thicknesses is shown in Figure 15. The microporous surfaces show much earlier ONB, 2 – 4 K, compared to that of the flat surfaces, 11 – 12 K, which is believed due to the pores in the microporous coatings providing an active nucleation sites [53, 54]. Despite the similar behavior at low heat flux (< 200 kW/m^2), the boiling curves at high heat flux significantly differ from each other. As the thickness increases, the CHF increases along with a significant rise in the surface superheat, in agreement with a previous experimental study [15]. The CHFs of 0.3 mm and 1.5 mm microporous coatings are 1469.0 kW/m^2 and 1888.9 kW/m^2, showing a 85 % and a 138 % increase respectively compared to that of the flat surface. However, the superheats at CHFs of the thick coatings (1.5 mm and 2.0 mm) exceed 110 K, which results in even lower HTCs at high heat flux (> 500 – 600 kW/m^2) than that of the flat surface. The average HTCs of 0.3 mm and 1.5 mm microporous coatings are 105.0 $kW/(m^2K)$ and 25.4 $kW/(m^2K)$, showing a 375 % and a 14.9 % increase

respectively compared to that of the flat surface. For the 2.0 mm porous coatings, the experiment didn't reach CHF due to the limitation of the experimental setup (melting temperature of the Epoxy and PEEK). Since thick microporous coatings present low HTCs (or large superheat), an optimal thickness has been studied [43, 55, 56], which maximizes the heat transfer coefficient. The studies experimentally determined the optimal thickness to be 2 – 4 times the particle size for the sintered porous surface using spherical particles, which corresponds to the 0.3 mm and 0.5 mm microporous coatings in the present experiment.

For the validation of the present experiment, the values of the present CHFs were compared to the reference value [57] as shown in Table 4. The direct comparison is not available since the parameters of the microporous coatings are different as well as the experimental pressure is different. However, when considering 31% increase in CHF from 50 kPa to 1 atm on the flat surfaces from Table 2, the discrepancy shown in Table 4 is within a reasonable range, and therefore it is believed to measure the correct CHFs.

Table 4 – CHF comparison between the reference values [57] and the present measured values. Since the reference only tested the samples around optimal thickness, the present results around the optimal thickness were compared.

	Reference at 1 atm		**Present at 50 kPa**	
Porosity	0.63	0.66	0.43	
Avg. particle size, d_p (μm)	25	67	138	
Coating thickness, δ (μm)	94	296	300	500
Ratio, δ / d_p	3.8	4.4	2.2	3.6
Measure CHF (kW/m^2)	~1750	~2100	1469	1528

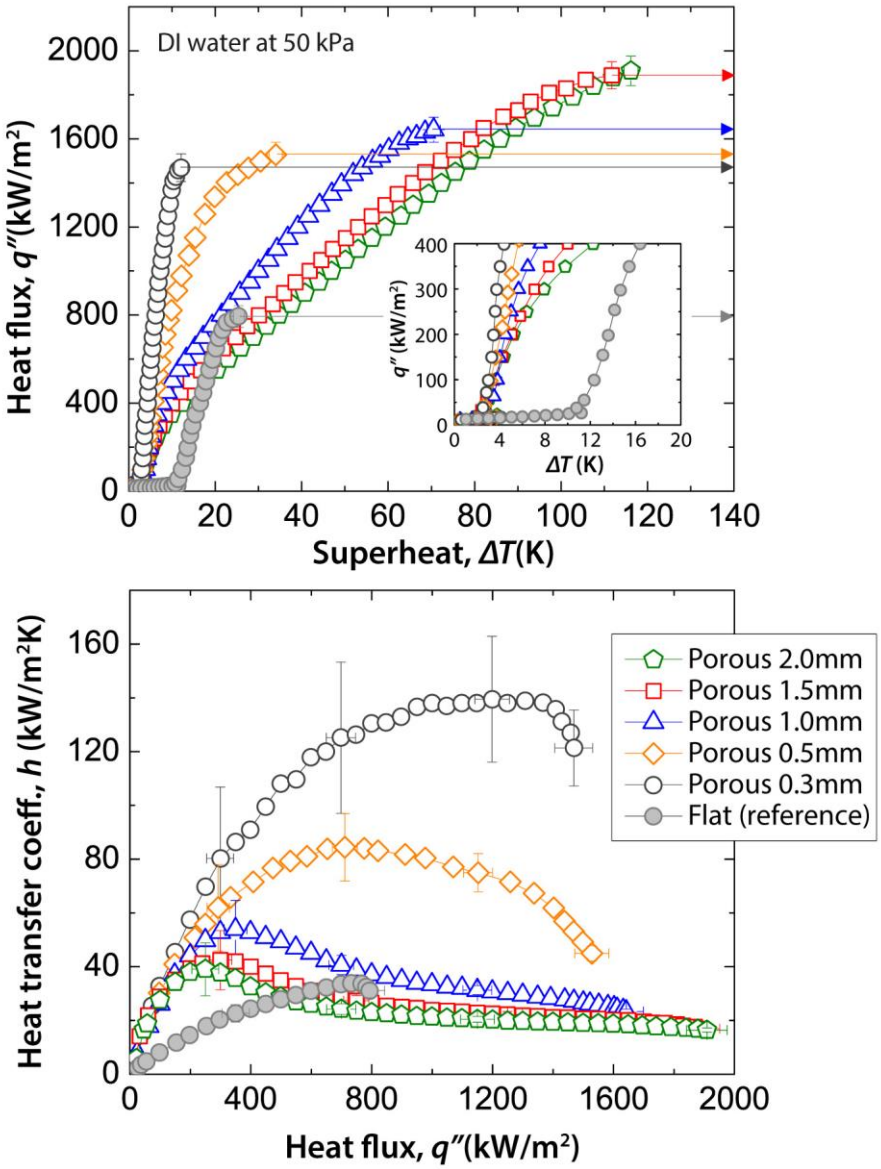

Figure 15 – Boiling curves and HTC of the microporous surfaces with different coating thicknesses. The experiment was conducted for DI water at 1atm, and the arrows denote that CHF was reached.

3.2.2 Comparison between Models and Present Experiment

The models and the experimental results were compared to determine their agreement with the physical response of our microporous coatings. Figure 16a compares the models to the present data for DI water at 50kPa. The range in the CHF by the

hydrodynamic instability model is due to the ambiguity in the breakthrough radius from Eq.3.7 – Eq.3.9. Neither of the models predicted the experimental CHFs well: The hydrodynamic instability model does not depict the thickness dependency shown in the experimental CHFs, overestimating the CHF by 1.5 – 3 times. The viscous-capillary model shows an inverse trend to the experimental CHFs with respect to the coating thickness, underestimating CHF by an order of magnitude for the thick microporous coatings (≥ 1.0 mm). The discrepancy is also observed with respect to a different working fluid. Figure 17 compares the models to the data taken from reference [45], in which the experiment was conducted for FC72 at 1atm. The uncertainties in the values by the viscous-capillary model were caused by the unknown viscosity of vapor phase of FC72 (see Appendix A2). The measured CHFs are larger than the viscous-capillary model but smaller than the hydrodynamic instability mode.

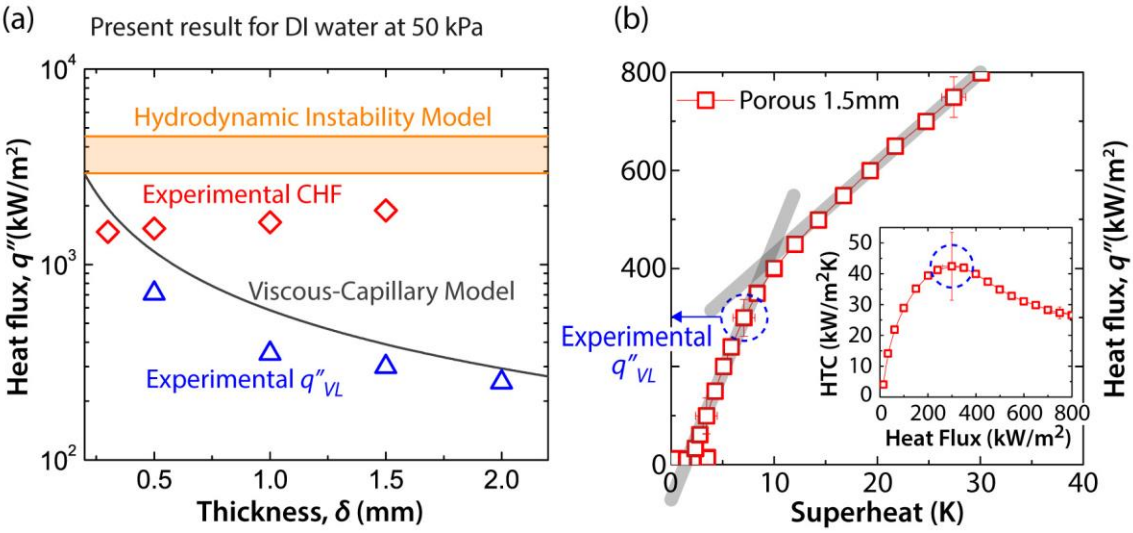

Figure 16 –(a) A comparison between the models and the present experimental results, and (b) an experimental estimation of vapor-layer heat flux from the boiling curve for 1.5 mm thick coatings.

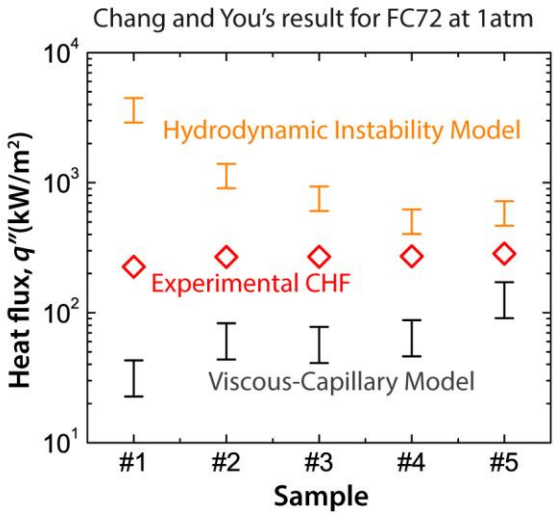

Sample	#1	#2	#3	#4	#5
Particle dia. d_p (μm)	2	10	20	45	70
Porosity, ε	0.48	0.41	0.40	0.40	0.47
Thickness δ (μm)	30	50	100	200	250

Figure 17 – A comparison between the models and the experimental results for FC72. The experimental data was taken from Chang and You's study [45].

The viscous-capillary model appears to resemble the heat flux at the point of the slope change (q''_{VL}) in the boiling curve and heat transfer coefficient curve (Figure 16b), and the values are in the same order of magnitude. In previous studies [49, 50], the change in slope in Figure 16b was stated to be due to film boiling, and therefore the heat flux at the slope change was determined to be the CHF. In the present study, however, transition boiling was clearly observed at much higher heat flux, and the maximum heat flux before advancing to the transition boiling was determined to be CHF. The slope change is believed due to the formation of a vapor layer at the bottom of the microporous coatings, and more discussion will be provided later. Therefore, the heat flux at the slope change should be distinguished from CHF, and defined as the vapor-layer heat flux, q''_{VL}, in this study.

3.2.3 Viscous-Capillary Flow Aspect: Vapor-layer Heat Flux

A vapor-layer heat flux as a function of the microporous coating thickness with different porosities as well as different particle sizes was computed by Udell's [42] and Lu

and Chang's correlation [43] (see Figure 18). Possible reasons of the discrepancy between the model and the experimental data would be either an overestimation of the porosity for the present samples or an incorrect use of a pore size distribution index—infinity was assumed in the Udell's correlation while two was suggested for a typical porous medium [43, 58]. The vapor-layer heat flux with respect to the thickness, the porosity, and the particle diameter is intuitively expected: The permeability increases as the porosity and the particle size increases, and the pressure drop of the flow decreases with an increased permeability according to Darcy's law. Therefore, large vapor-layer heat flux is expected with an increased permeability due to the ease of the vapor escape. Although it is not well understood whether the flow through the pores is laminar or turbulent, the effect of turbulent flow is only noticeable in thin coating thickness with the large particle size in Figure 18. For a very thick microporous coating, the vapor-layer heat flux is no longer a function of the coating thickness, which is shown for a thickness around 50 cm to 1 m in Figure 18, and the Udell's correlation is simplified to be a closed form solution as Eq.3.10:

$$q''_{VL} = \frac{\kappa h_{fg}\left(\rho_l - \rho_v\right) g}{\nu_v}\left[1+\left(\frac{\nu_l}{\nu_v}\right)^{\frac{1}{4}}\right]^{-4} \qquad \text{(Eq.3.10)}$$

The thickness that can be considered as very thick (less than 2% discrepancy with the prediction by Eq.3.10) is 106.1cm for the present structure—0.43 of the porosity and 137.5 μm of the particle diameter, and 35.4 cm for 0.43 of the porosity and 400 μm of the particle diameter. Therefore, an analysis with Eq.3.10 may not be useful for the practical cooling application, and confusion with CHF [50, 51] should be avoided since it predicts the vapor-layer heat flux.

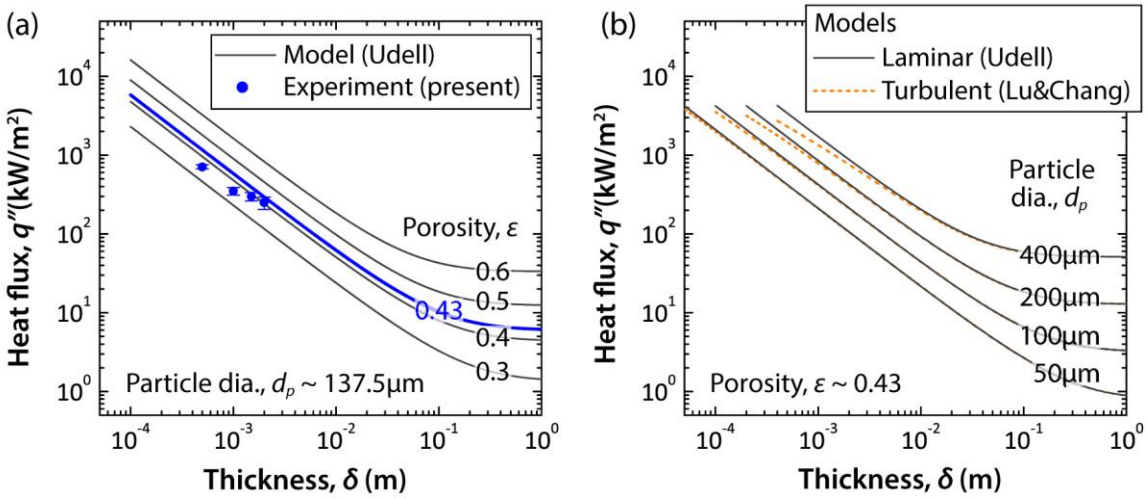

Figure 18 –(a) A vapor-layer heat flux as a function of the coating thickness with different porosities, and (b) a vapor-layer heat flux as a function of the coating thickness with different particle sizes. A laminar model was computed by Udell's correlation [42] and a turbulent model by Lu and Chang's [43] (a pore size distribution index = ∞). The water properties at 50 kPa were used.

3.2.4 Hydrodynamic Instability Aspect

The hydrodynamic instability model predicts that the CHF is independent of the thickness of the microporous coatings, being 2929.0 – 4519.5 kW/m^2 for the present sample (ε = 0.43 and d_p = 137.5μm) using Eq.3.6. Although the model overestimates the CHF, the higher CHF on microporous surfaces compared flat surfaces can be partially explained using the model (Figure 19). Zuber's correlation in Eq.1.1 and Polezhaev's correlation in Eq.3.6 can be rewritten in terms of vapor-jet diameter, D, as shown in Eq.3.11 – Eq.3.13:

$$q''_{CHF} = \frac{\pi}{8} h_{fg} \left(\frac{\sigma \rho_v}{2D} \right)^{1/2} \qquad \text{(Eq.3.11)}$$

$$D = \frac{9}{2} \left[\frac{\sigma}{g\left(\rho_l - \rho_v\right)} \right]^{1/2} \quad \text{for flat surfaces} \qquad \text{(Eq.3.12)}$$

$$D = \frac{r_{br}}{2}\left(\frac{\pi}{4.16\varepsilon^{2.28}}\right)^2 \qquad \text{for microporous surfaces} \qquad \text{(Eq.3.13)}$$

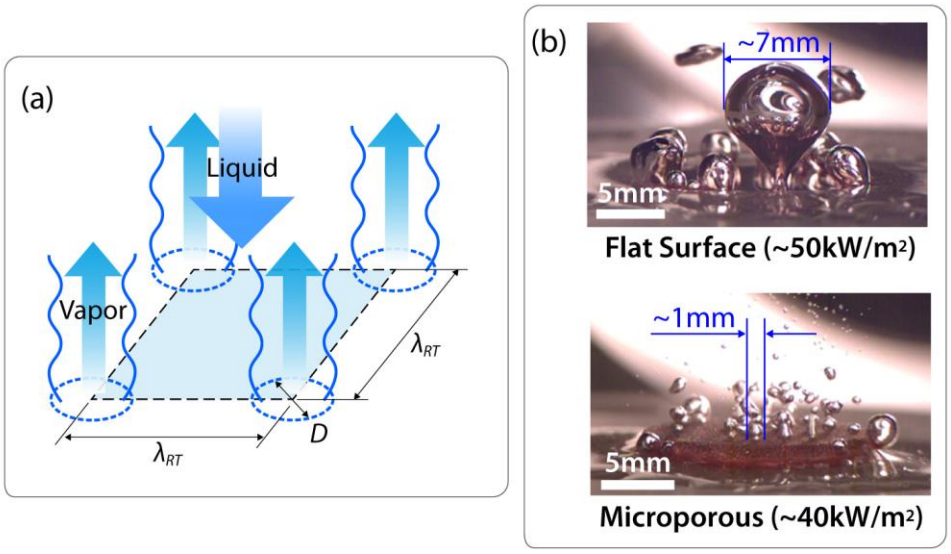

Figure 19 –(a) A schematic of the unit cell of hydrodynamic instability model, and (b) high-speed imaging of the bubble departure diameters.

In the study of Liter and Kaviany [51], Eq.3.11 – Eq.3.13 were presented in terms of the Rayleigh–Taylor (RT) wavelength, λ_{RT}, which is the distance between the vapor-jets (Figure 19a). In this study, however, we will use the vapor-jet diameter, which is simply assumed to be a half of the RT wavelength, due to the easiness of the comparison in the bubble size. Eq.3.11 explains that a higher CHF is achievable with smaller vapor-jet diameter. For water at 50 kPa, the jet diameters are estimated to be 11.5 mm on the flat surface and 0.38 – 0.92 mm on the microporous surface, theoretically. An experimental observation also provided a comparable size in Figure 19b: The bubble departure size on the microporous surface was less than 1 mm while that on the at surface varied 3 – 7 mm (the bubble departure sizes at low heat flux are presented for a clear visualization).

Therefore, a higher CHF is enabled on microporous surface due to the smaller vapor-jet size, which is caused by the modulation of the vapor through the pore network.

3.2.5 Present Explanation – Vapor layer growth

Based on this understanding, the pool boiling mechanism on microporous surfaces can be explained as follows: Until the heat flux reaches the vapor-layer heat flux, q''_{VL}, bubble nucleation mostly occurs at the bottom of the porous coatings due to higher superheat at the interface between the microporous and solid surfaces. This is also true for the heat transfer coefficient—which is supported by the experimental observation that the initial boiling characteristics ($h < 200$ kW/m^2) are almost the same regardless of the coating thickness (Figure 15). The vapor layer forms within the microporous coating and grows gradually due to viscous-capillary flow, resulting in a slope change in the boiling curve and eventually a large surface superheat at CHF.

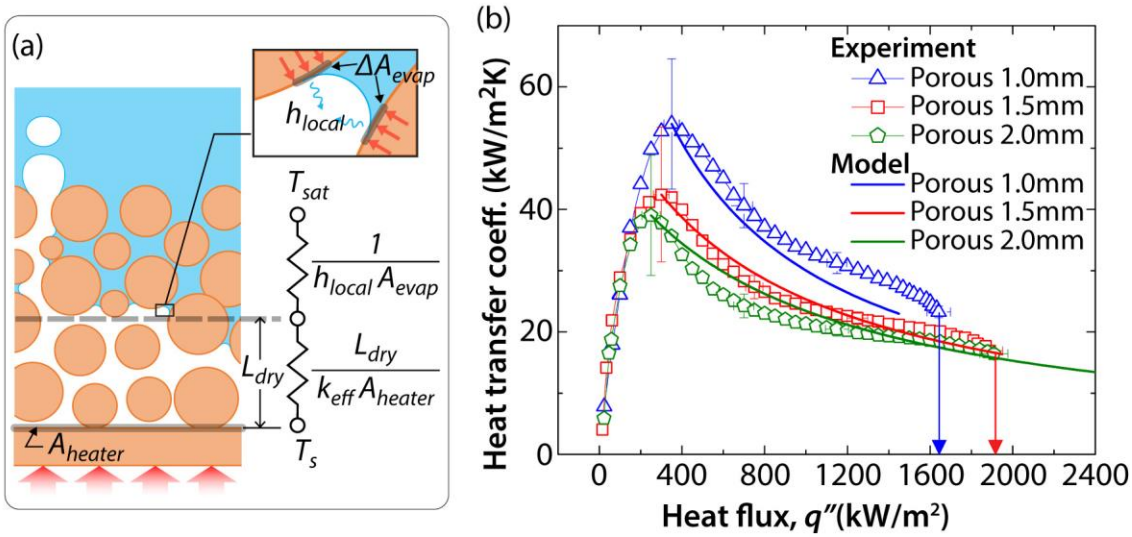

Figure 20 –(a) A schematic of the thermal resistance model, and (b) a comparison between the experimental data and the thermal resistance model.

To further explore this explanation, the vapor-layer growth was modeled using a thermal resistance network model (Figure 20a), postulating that the heat transfer occurs by evaporation at the liquid-vapor interface rather than by nucleation at other sites since it requires more energy to overcome a free energy barrier. For simplicity, we assumed that the vapor layer has a uniform thickness, L_{dry}, over the heater area. Since the thermal conductivity of the vapor is much smaller than that of the microporous coatings, the conduction resistance becomes L_{dry} / (k_{eff} A_{heater}), where k_{eff} is the thermal conductivity of the microporous coatings and A_{heater} is the heater area. The convection resistance can be modeled as *1* / (h_{local} A_{evap}), where h_{local} is the local heat transfer coefficient, and A_{evap} is the total evaporation area. Hence, the effective heat transfer coefficient becomes as shown in Eq.3.14:

$$h_{eff} = \left(\frac{L_{dry}}{k_{eff}} + \frac{A_{heater}}{h_{local} A_{evap}} \right)^{-1} \quad \text{(Eq.3.14)}$$

Since h_{eff} = $h_{q''VL}$ when L_{dry} = 0, where $h_{q''VL}$ is the experimental HTC at the vapor-layer heat flux, then A_{heater} / (h_{local} A_{evap}) in Eq.3.14 is approximated to Eq.3.15:

$$h_{eff} = \left(\frac{L_{dry}}{k_{eff}} + \frac{1}{h_{q''VL}} \right)^{-1} \quad \text{(Eq.3.15)}$$

By fitting the model to the experimental data, the linear relationship between the heat flux increase and the vapor-layer thickness was assumed as Eq.3.16

$$q'' - q''_{VL} = C^* L \quad \text{(Eq.3.16)}$$

where C^* is a constant estimated from the experimental data and 1.10×10^9 W/m^3 was used regardless of the thickness. A comparison between the model and the experimental data is shown in Figure 20b for the thick porous coatings (1.0, 1.5 and 2.0 mm) in which the characteristic of the vapor-layer growth is obvious, and a good agreement has been obtained. Despite the rough assumptions, the model strongly supports the current explanation that the vapor layer forms and grows in the microporous coatings. Also, the model explains that the growth of the vapor layer manifests itself as a decrease in HTC unlike typical surfaces where HTC increases with an increased heat flux.

The possible reason of the vapor-layer growth is shown in Figure 21: The vapor escapes through open pathways while the liquid flows in the microporous coatings. The vapor layer at the bottom of the porous coatings is sustained by the capillary pressure of the meniscus, p_c. In that condition, the capillary pressure is larger than the sum of the pressure drop of the vapor flow, Δp_v, and the liquid flow, Δp_l. as Eq.3.17:

$$p_c = \left(p_{sat} + \Delta p_v \right) - \left(p_{sat} - \Delta p_l \right) = \Delta p_v + \Delta p_l \qquad \text{(Eq.3.17)}$$

As the heat flux increases, the pressure drop of the vapor flow increases since the vapor evaporation increases and so does the mass flow rate of the vapor. The change in the pressure drop of the liquid flow is much smaller than that of vapor flow due to the difference in the specific volume. If the sum of the pressure drop exceeds the capillary pressure, the meniscus will break, and the vapor layer will advance upward. This will cause either an increase in the number of the vapor-escape paths or an increase in vapor-layer thickness. Those two phenomena may occur simultaneously, and the pore size are

distributed due to the random packing of the particles, therefore, the vapor-layer thickness, L_{dry}, would vary over the heater area, which makes an accurate analysis difficult.

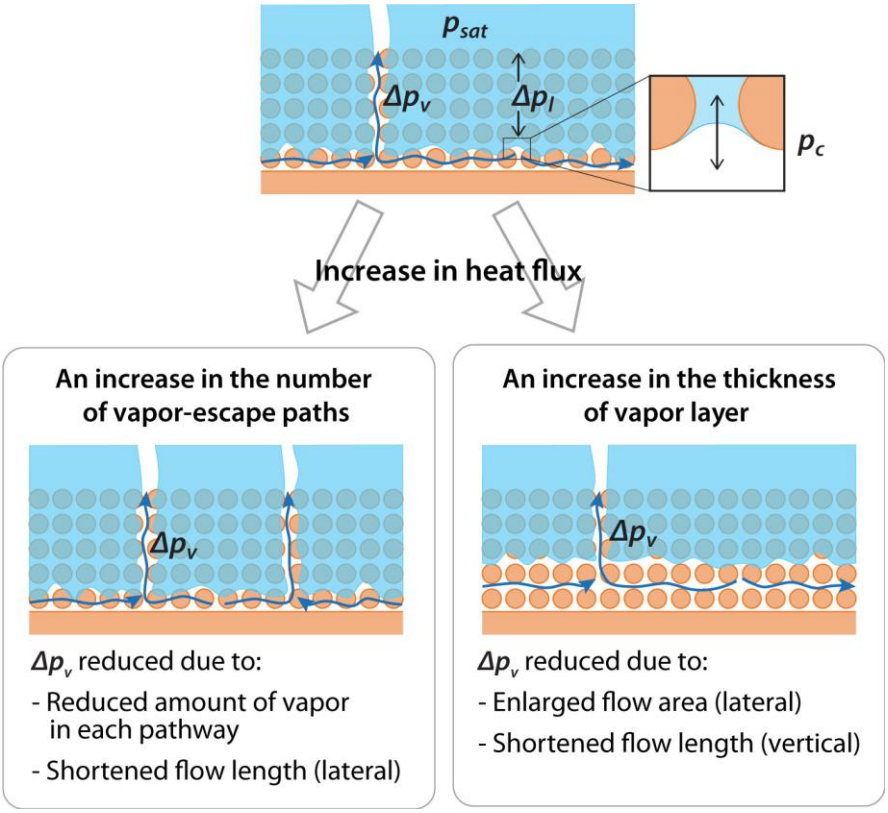

Figure 21 – A schematic for the explanation on the vapor-layer growth

The optimal thickness as well as the enhancement in HTC using the microporous surfaces are possibly related to the nonuniform thickness of the vapor-layer formation: The optimal thickness may be understood as the maximum thickness of the microporous coatings in which the vapor layer does not form, and therefore the slope change does not occur. The enhancement in HTC using the microporous surfaces possibly relies on the effect of the extended surface as the liquid-vapor interface stretches over the nonuniform thickness of the vapor layer as well.

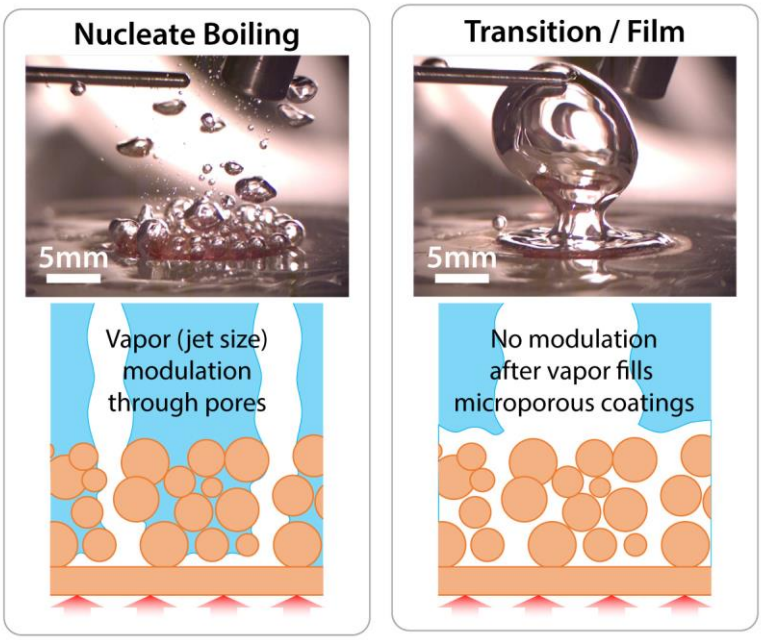

Figure 22 –High-speed imaging and schematics that explain the CHF mechanism on microporous surfaces.

Accepting the mechanism of the vapor-layer formation and growth in the microporous coatings, we can postulate that the CHF of microporous surfaces occurs when the vapor fills the microporous coatings as shown in Figure 22, which explains thickness dependency of CHF as well. Until CHF is reached, the modulation of the vapor-jet occurs through the pore network, and therefore a higher CHF is enabled due to small vapor-jet size. However, the modulation is no longer available after the vapor fills the microporous coatings, and sudden transition boiling occurs. High-speed imaging of the experiment supports the present explanation. During nucleate boiling, the vapor-jet (or bubble) departure diameter on the porous surface was around 1 mm. During transition to film boiling, however, the vapor covered the microporous surfaces, and the departure of large vapor slugs (~ 10 mm) was observed.

3.3 Summary

A pool boiling mechanism on our reference plain microporous surfaces was studied and explained in this chapter. A typical boiling curve of microporous surface is shown Figure 23. The boiling curve shows two distinct slopes when the coating thickness is larger than the optimal thickness. At low heat flux, bubble nucleation is believed to occur at the bottom of microporous coatings due to the high surface superheat. As the heat flux increases, a vapor layer forms and grows from the bottom of the microporous coatings due to the viscous-capillary flow of liquid and vapor phase. We defined the heat flux at which the vapor layer initiates as the vapor-layer heat flux, which may be predicted by Udell's correlation. Since the evaporation line is lifted from the heater surface due to the vapor layer, a large thermal resistance is introduced owing to the low thermal conductivity of the microporous structure. The vapor-layer growth manifests itself as a slope change in the boiling curve (the plot of heat flux vs. superheat) or the decrease in HTC (the plot of HTC vs. heat flux). Regardless of the large superheat, a higher CHF is achieved compared to the flat surfaces due to the modulation of vapor jets—the vapor flow through the microporous coatings results in smaller size of the vapor-jet than that of the flat surface, therefore hydrodynamic instability is delayed. Practically, the CHF of the microporous surfaces is a resulted of the dryout of the microporous coatings as a large size of the vapor-jet is formed without the modulation after vapor fills the microporous coatings. The CHF by hydrodynamic instability, $q''_{CHF,h}$, may predict the limit of CHF that is achievable. As the thickness of microporous coating increases, the vapor-layer heat flux decreases, and the CHF increases with an extended partial dryout zone, resulting in a large superheat. A further increase in the coating thickness may result in CHF being controlled by

hydrodynamic instability rather than by the dryout of the microporous coatings, also resulting a large superheat.

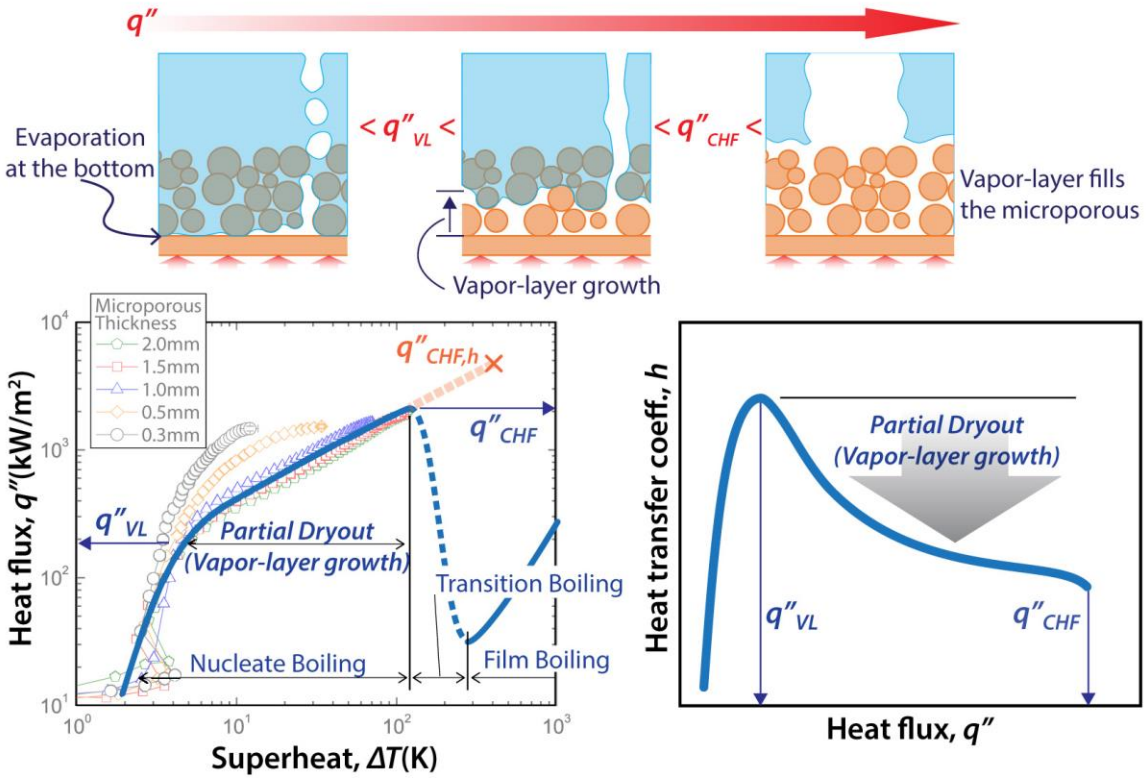

Figure 23 –Typical pool boiling characteristic of the plain microporous surfaces. The present experimental data with different thickness was overlaid with the schematic of the boiling curve.

Recent studies mostly focus on the optimal thickness of the microporous coatings since it maximizes HTC, which is achieved with relatively thin coatings as 2 – 4 times of the particle diameter when spherical particles are used. In light of the present study, the optimal thickness can be understood as the maximum thickness of the microporous coatings in which the vapor layer does not form due to the nonuniform thickness of the vapor layer in its practical formation. Nonetheless, the optimal thickness exhibits relatively low CHF compared to the thick microporous coatings, and therefore, an enhancement in

both CHF and HTC will be presented with the structural modification of thick microporous coatings.

CHAPTER 4. POOL BOILING CHARACTERISTICS OF MICROPOROUS SURFACES WITH VAPOR CHANNELS

4.1 Background

Although the plain microporous surfaces significantly enhance the boiling heat transfer, there is a trade-off between CHF and HTC with respect to the coating thickness—as the microporous coating thickness increases, CHF increases while HTC decreases. Based on the understanding in Chapter 3, the plain microporous surfaces will be structurally modified to achieve an enhancement both in CHF and HTC, which will be done by disrupting the formation of the vapor-layer through the fabrication of vapor channels onto the microporous coatings. Patterned microporous surfaces, which are similar to the microporous surfaces with the vapor channels in the present study, were studied by researchers to enhance the boiling heat transfer [16, 51, 59-61]. While the experiments exhibited an enhancement, the mechanism of the enhancement is not well understood. Like the plain microporous surfaces, the CHF mechanism of the patterned microporous surfaces was studied in terms of viscous-capillary flow and hydrodynamic instability. Liter and Kaviany [51] stated that CHF is reached by the hydrodynamic instability since the limit by viscous-capillary flow is generally much higher than that while Mori and Okuyama [16] stated that CHF is determined by the viscous-capillary flow rather than hydrodynamic instability. We will briefly review those two studies to lead a better understanding on the boiling mechanism on the patterned microporous surfaces.

4.1.1 Liter and Kaviany's Study

A conical pattern in microporous surfaces was studied through viscous-capillary analysis as well as hydrodynamic analysis, which were referred as the analysis of "viscos-drag liquid-choking limit" and "hydrodynamic liquid-choking limit" respectively in their study. For the viscous-capillary flow, a similar analysis like the plain microporous surface was conducted through a numerical method since the shape of the pattern was modelled to two dimensions. They assumed that the liquid flows along the surface of the conical pattern rather than flows through the pores, and the evaporation occurs on the surface at the bottom edge of each conical structure. The hydrodynamic instability analysis was done by using the modulated wavelength, λ_m, substituting for the Rayleigh-Taylor (RT) wavelength, λ_{RT}, in the Zuber's correlation (Eq.1.1), which can be rewriten as Eq.4.1:

$$q''_{CHF} = \frac{\pi}{8} h_{fg} \left(\frac{\sigma \rho_v}{\lambda} \right)^{1/2} \qquad \text{(Eq.4.1)}$$

$$\lambda = \lambda_{RT} = 9 \left[\frac{\sigma}{g(\rho_l - \rho_v)} \right]^{1/2} \qquad \text{for flat surface} \qquad \text{(Eq.4.2)}$$

$$\lambda = \lambda_m \qquad \text{for modulated surfaces} \qquad \text{(Eq.4.3)}$$

where h_{fg} is the latent heat of vaporization, σ is the surface tension, ρ is the density, g is the gravitational acceleration, λ is the wavelength of the vapor-jet, and the subscript, *l* and *v*, denotes the liquid and the vapor phase respectively. Eq.4.1 is the same with Eq.3.11 in that $\lambda=2D$. The wavelength on the flat surfaces is given by RT instability through Zuber's analysis as Eq.4.2 while the modulated wavelength is directly given by the structural pattern of the microporous surfaces as Eq.4.3. A detail of the hydrodynamic instability will

be discussed in Chapter 5. Based on the analysis, they stated that CHF is determined by hydrodynamic instability since the CHF prediction by viscous-capillary analysis is an order of magnitude higher than that by hydrodynamic instability analysis. An experiment was conducted to validate the analysis using Pentane at 1 atm. The microporous surfaces were fabricated by sintering 200 μm spherical Cu particles, and the patterning on the microporous surfaces were achieved using different shapes of sintering molds. Two patterned surfaces were tested, and the comparison to the theories are shown in Table 5. One agreed well while the other did not, presenting 4.6% and 22.7% discrepancy respectively. The discrepancy was explained given that a stable wavelength had not necessarily developed between the nearest distance of the pattern.

Table 5 – A comparison between the theories and the measurement by Liter and Kaviany [51]. The particle size, d_p, is 200 μm, and the porosity is 0.4. The properties of Pentane is tabulated in Appendix A.2.

λ_m	**Predicted CHF (kW/m^2)** *using Eq.4.1 and Eq.4.3*	**Measured CHF (kW/m^2)**	**Discrepancy (%)**
$5d_p$ (100 μm)	921.3	712	22.7
$8d_p$ (160 μm)	728.4	762	4.6

4.1.2 Mori and Okuyama's Study

A patterned porous plate, which is commercially available for the use of gas filtration, was tested by attaching it to the heater surface. The porous plate was made of ceramic compounds ($CaO{\cdot}Al_2O_3$, SiO_2, and TiO_2), and the average and the median pore radius were measured to be 37 nm and 130 nm respectively with 0.248 of the porosity. The porous plate has an array of hole of $1.3 \times 1.3 mm^2$ with 1.7mm pitch. Three samples were

tested in the variation of the plate thickness: 1.2 mm, 5.0 mm and 10.0 mm. The experiment was conducted for DI water at 1 atm, and the result is shown in Table 6. The viscous-capillary analysis was studied by considering the capillary pressure, the flow pressure drop of liquid an vapor, and the acceleration pressure drop. The assumption was made that the liquid flows through the porous layer, that the vapor flows through the hole array, and that the evaporation occurs at the bottom corner of the porous plate where it contacts the heater surface. After comparing the experimental result to their analysis and to the Liter and Kaviany's model in Eq.4.1 and Eq.4.3, they stated that CHF is determined by the viscous-capillary flow rather than hydrodynamic instability. Also, the flow pressure drop of the liquid is dominant for their structure, and CHF can be simplified and predicted as Eq.4.4:

$$q''_{CHF} = \frac{2\kappa\sigma h_{fg}}{r_{eff}\delta\nu_l}\left(\frac{A_l}{A}\right) \qquad \text{(Eq.4.4)}$$

where κ is the permeability, r_{eff} is the effective pore radius, δ is the thickness of the porous, ν is the kinematic viscosity, and A_l/A is the ratio of the wetted area (the contact area of the porous plate to the heater surface) to the heater surface. The CHF by the theories and the measurement are compared in Table 6. Although the viscous-capillary model predicts the decrease in CHF with respect to the porous thickness, a significant discrepancy was found compared to the measurement.

Table 6 – A comparison between the theories and the measurement by Mori and Okuyama [16]. For Eq.4.4, κ and r_{eff} were taken as shown in the reference, and A_l/A was assumed to be ~3.7. For Eq.4.1, the pitch of 1.7mm was used for λ_m.

Plate Thickness, δ (mm)	**Predicted CHF** (kW/m^2)		**Measured CHF** (kW/m^2)
	Hydrodynamic Instability Model in Eq.4.1	Viscous-Caipllary Model in Eq.4.4	
1.2	4033	4160	2510
5.0	"	998.4	1400
10.0	"	499.2	1040

Those two studies compared two scenarios that may cause CHF in the patterned microporous surfaces and reported the opposite conclusion. In this chapter, we will propose a unified explanation on the boiling characteristics of the patterned microporous surfaces, by analyzing the present experimental data and by adopting Liter and Kaviany as well as Mori and Okuyama's studies based on the boiling mechanisms of the plain microporous surfaces from Chapter 3. Also, we will suggest an enhanced structure to validate the present explanation.

4.2 Procedure, Result and Discussion

4.2.1 Fabrication of Vapor Channels: A Visual Investigation of Vapor Removal

The plain microporous surfaces were fabricated first by sintering spherical particles (Cu, 125-150 μm in the particle diameter) to be 15.95 cm in the sample diameter (2 cm^2 of the area). The details of the sample fabrication are shown in Chapter 2. Then, the vapor channels were fabricated in the plain microporous surfaces as shown in Figure 24a to remove the vapor layer that is formed at the bottom of the microporous coatings. The

channel fabrication was conducted using dicing saw or micro milling mahcine by removing the particles being separated at the necks rather than by cutting the particles. The high-speed imaging during the pool boiling experiment clearly showed the vapor escape through the channels (Figure 24b), generating the flow pattern as the vapor escapes through the vapor channels and the liquid flows through the microprous coatings.

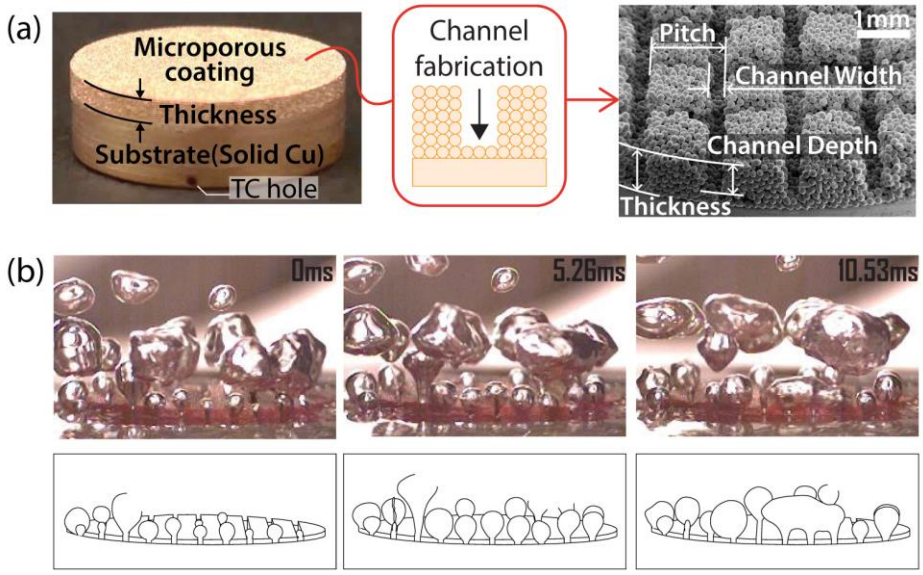

Figure 24 –Microporous surfaces with vapor channels: (a) microporous surfaces before and after vapor channel fabrication, and (b) high-speed imaging of the vapor escape through the vapor channels.

4.2.2 Experimental Parametric Study: Variation in Vapor-Channel Dimension

A pool boiling experiment was conducted with respect to the channel demension in the microporous surfaces. The thickness of the microporous coatings was fixed to be 1.5 mm thoughout the experiment, and the channel depth, pitch, and width were varied. The experiment was conducted for DI water at 50 kPa and the reduced pressure was used to observe CHF at the large superheat. Since we assume that the vapor layer forms and grows from the bottom of the microporous coatings, the effect of the channel depth was

investigated first (Figure 25). Three different channel depths were examined: 0.3, 0.6, and 1.2 mm, and the pitch and the width were fixed to be 1.5 mm and 0.35 mm, respectively. The channel depth is limited to less than 1.2 mm due to the difficulties in the fabrication. As the depth of the vapor channel increases, both CHF and HTC were enhanced significantly. Regarding the channel pitch, four variations were examined (Figure 26): 1.5, 2.0, 2.5, and 4.0 mm, and the channel depth and width were fixed to be 1.2 mm and 0.35 mm, respectively. As the channel pitch decreases, both CHF and HTC were enhanced significantly. However, the result of 1.5 mm and 2.0 mm of the pitch shows a negligible difference except the behavior around CHF. Regarding the channel width, three variations were examined (Figure 27): 0.35 mm, 0.70 mm, and 1.0 mm, and the channel depth and pitch were fixed to be 1.2 mm and 2.0 mm, respectively. Unlike other parameters, the channel width hardly affects HTC while CHF decreases as the channel width increases. The sample with 1.0 mm of the channel width presents noticeable reduction in CHF, and the samples with 0.35 mm and 0.70 mm channel widths present similar CHF within the uncertainty range. Among the tested samples, the largest enhancement was achieved with the sample that has 1.2 mm of the channel depth, 1.5mm of the channel pitch, and 0.35 mm of the channel width, to be 3547.5 ± 117.8 kW/m^2 in CHF and 89.9 $kW/(m^2K)$ in average HTC, which is a 88 % enhancement in CHF and a 254 % enhancement in average HTC compared to those of the plain microporous surfaces, and a 347 % enhancement in CHF and a 307 % enhancement compared to those of the flat surfaces. The experiment at 1atm presented over 4000 kW/m^2 in CHF, but could not reach CHF due to the limit of the experimental setup.

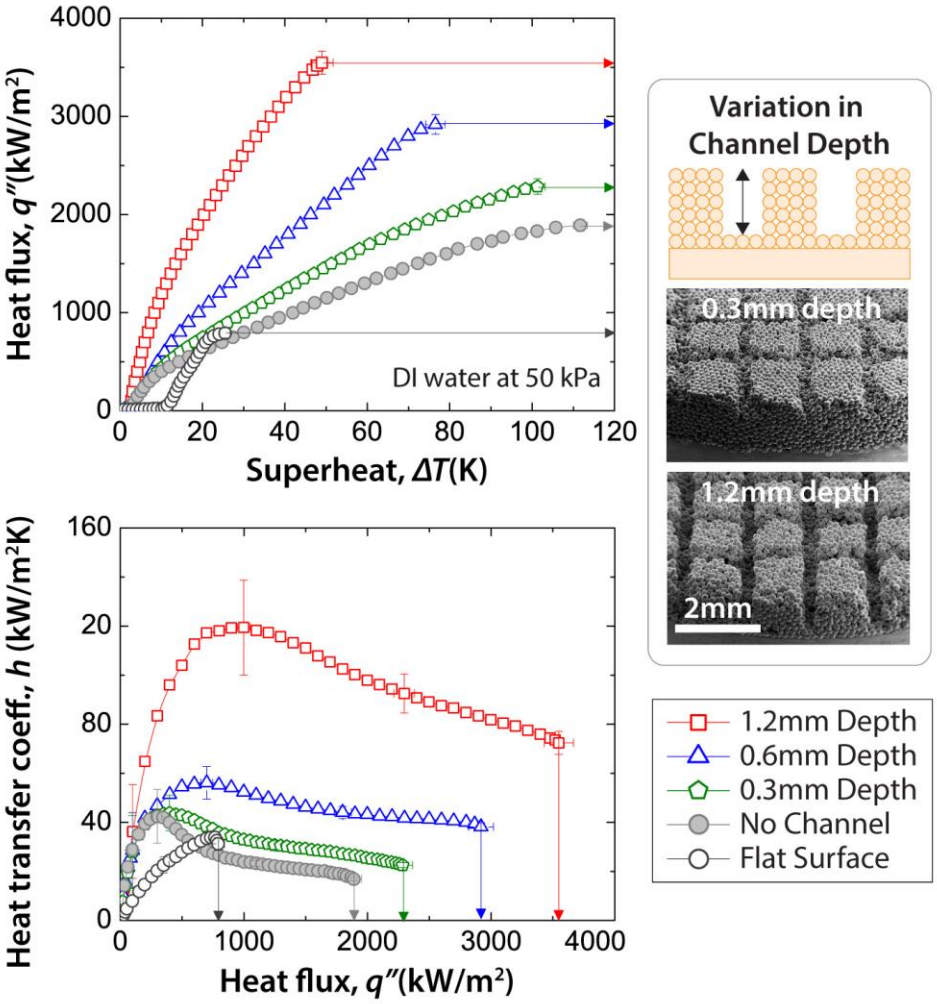

Figure 25 –The effect of the channel depth on pool boiling characteristics. The coating thickness is 1.5 mm, the channel pitch is 1.5 mm, and the channel width is 0.35 mm. The SEM images of some samples are presented. The experiment was conducted for DI water at 50 kPa, and the arrow denotes that CHF was reached.

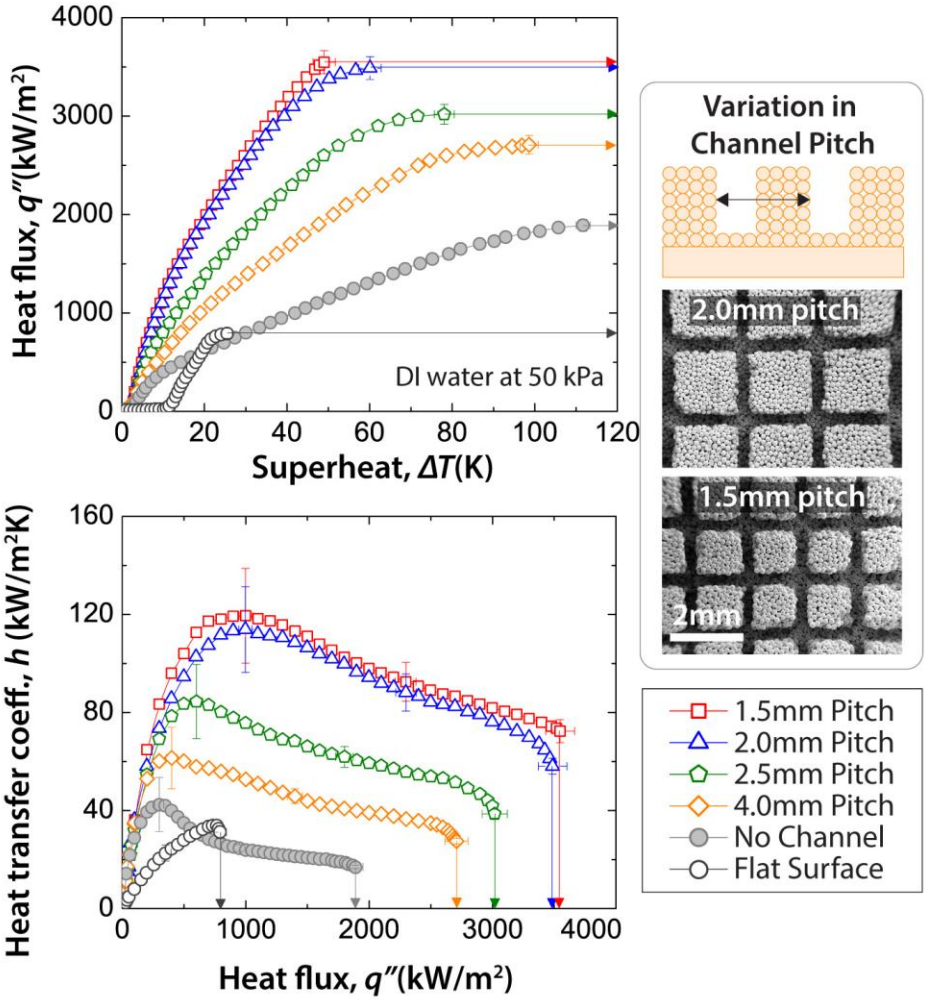

Figure 26 –The effect of the channel pitch on pool boiling characteristics. The coating thickness is 1.5 mm, the channel depth is 1.2 mm, and the channel width is 0.35 mm. The SEM images of some samples are presented. The experiment was conducted for DI water at 50 kPa, and the arrow denotes that CHF was reached.

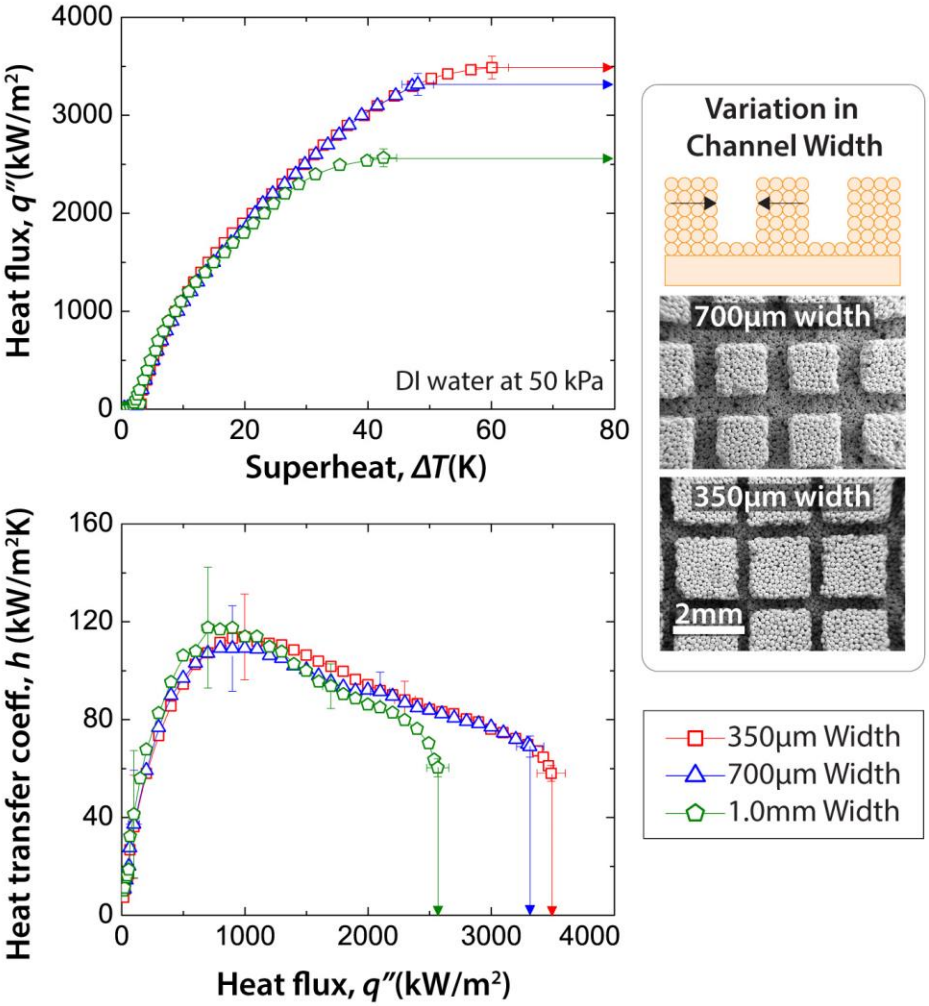

Figure 27 –The effect of the channel width on pool boiling characteristics. The coating thickness is 1.5 mm, the channel pitch is 1.5 mm, and the channel depth is 1.2 mm. The SEM images of some samples are presented. The experiment was conducted for DI water at 50 kPa, and the arrow denotes that CHF was reached.

The experimental parametric study in Figure 25 – Figure 27 shows that the boiling characteristics of the microporous surface is significantly affected by the design of the vapor channels. As the channel depth increases, CHF and HTC are enhanced, indicating that the vapor layer exists at the bottom of the microporous coatings and presenting that deep vapor channels lead to easy escape of the trapped vapor. As the channel pitch decreases, CHF and HTC are enhanced as well, which can be interpreted as either a small

pitch by itself or a large projected area of the vapor channel is beneficial to the vapor escape. According to the result of the channel width variation, however, the projected area of the vapor channel is inversely related to the enhancement in that the smaller width shows higher CHF and HTC. Therefore, the pitch of the vapor channel by itself plays an important role in the enhancement. Another notable aspect throughout the parametric experiment is that the characteristic of the vapor-layer growth was observed even with the fabrication of the vapor channels—a decrease in HTC with an increased heat flux in the plot of HTC vs. heat flux. To understand the reason of the vapor-layer growth as well as the effect of the channel pitch, an analysis was conducted with a simplified model.

4.2.3 Viscous-Capillary Aspect: The Reason of Vapor-Layer Growth

Since the vapor-layer growth in the plain microporous surfaces is caused by viscous-capillary flow, an analysis was conducted in terms of capillary pressure and pressure drop of the flows. For the analysis, it is crucial to define the path of the liquid and vapor flow. While the previous studies assumed that the evaporation occurs around the bottom corner of the vapor channels [16, 51], we postulate that the evaporation occurs at the bottom of the microporous coatings like the plain microporous surfaces (Figure 28). The lateral vapor flow is possibly caused by merging with adjacent bubbles since the travel distance among the bubbles is shorter than that through the thickness of the microporous coatings. Generally, the direction of the vapor flow in the microporous coatings varies with the heater size: While the vapor escape through the side of the microporous coatings is dominant for the smaller heater (8×8 mm^2 square) [15], denoting that the vapor flows laterally, the vapor escape through the thickness of the microporous coatings is noticeable for the larger heater in the present study (1.6 mm in diameter). Since the microporous

surfaces with vapor channels can be considered as an array of small plain microporous surfaces as each of them shown in Figure 25 – Figure 27 is less than a 4 × 4 mm^2 square, the boiling characteristic is expected to be similar to that of the plain microporous surfaces, and therefore the postulate that we made is reasonable.

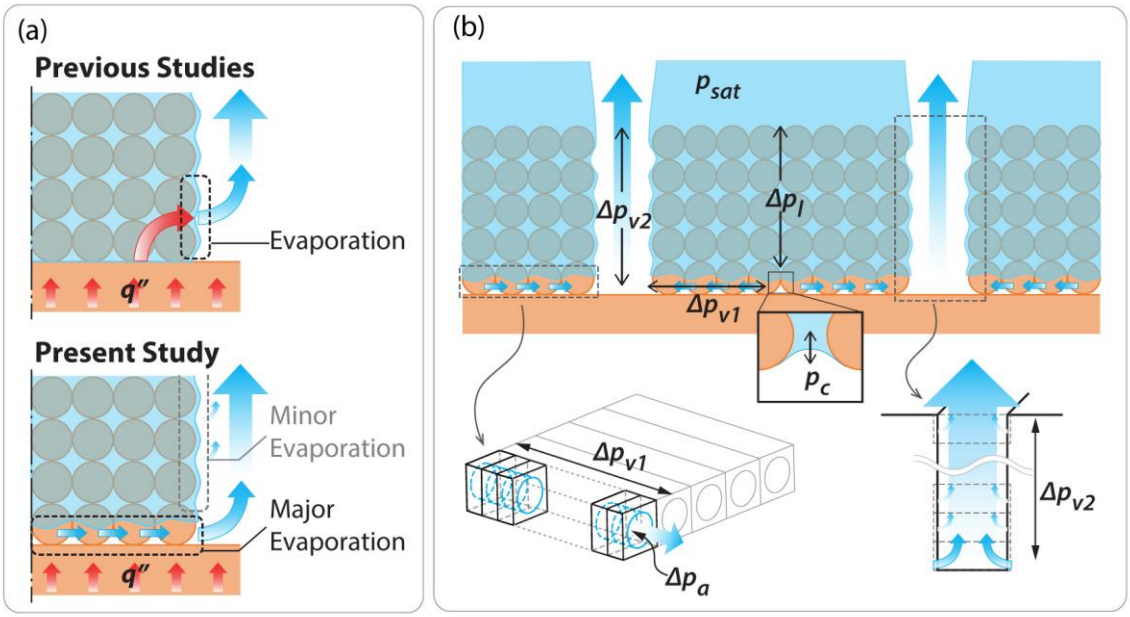

Figure 28 –(a) The evaporation region of the previous studies and the present study, (b) a schematic of the microporous coatings with vapor channels for the estimation of the flow pressure drop.

The problem was simplified as shown in Figure 28. The vapor layer growth is restrained by the capillary pressure, p_c, and when the pressure difference across the meniscus exceeds the capillary pressure, the meniscus will break and the vapor layer will move upward. When the meniscus breaks, the capillary pressure is expressed in terms of the flow pressure drop of the vapor and liquid phase, and the acceleration pressure drop as Eq4.5. Here, we analyzed the case that vapor layer is at the very bottom of the microporous coatings, which correspond to the vapor-layer heat flux.

$$p_c = \Delta p_l + \Delta p_{v1} + \Delta p_{v2} + \Delta p_a \quad \text{(Eq.4.5)}$$

where Δp_l is the pressure drop of the liquid flow through the microporous coatings, Δp_{v1} is the pressure drop of the vapor flow through the pores, Δp_{v2} is the pressure drop of the vapor flow through the vapor channels, and Δp_a is the acceleration pressure drop due to the phase change. The capillary pressure is given as Eq.4.6:

$$\Delta p_c = \frac{2\sigma}{r_{eff}} \quad \text{(Eq.4.6)}$$

where σ is the surface tension, and r_{eff} is the effective pore radius. The pressure drop of the liquid flow is given by Darcy's law as Eq.4.7:

$$\Delta p_l = \frac{\mu_l \dot{m}_l \delta}{\rho_l \kappa A_l} \quad \text{(Eq.4.7)}$$

where μ is the viscosity, ρ is the density, κ and δ is the permeability and the thickness of the microporous coatings repectively. $\dot{m}$ is the mass flow rate, and A is the cross-sectional area of the flow. The subscripts, l and v, denote the liquid and vapor phase. The pressure drop of vapor flow, Δp_v, was simplified to the laminar flow through a cylindrical pipe as Eq.4.8:

$$\Delta p_v = \frac{128 \mu_v \dot{m}_v L}{\pi \rho_v d_v^4} \quad \text{(Eq.4.8)}$$

where ρ is the density, d is the hydraulic diameter, and L is the flow length. For Δp_{v1}, the pore hydraulic diameter in packed spherical particles and the half width of the microporous post were used for d and L, respectively. For Δp_{v2}, the twice of the channel width with the

assumption of infinite channels and the channel depth for d and L, respectively. The acceleration pressure drop of the flow was simplified as Eq4.9:

$$\Delta p_a = \left(\frac{\dot{m}_v}{A_v}\right)^2 \left(\frac{1}{\rho_v} - \frac{1}{\rho_l}\right) \qquad \text{(Eq.4.9)}$$

The acceleration pressure drop through the pores was only considered since the pressure drop through vapor channel was negligible. The details of the analysis are shown in Appendix C2.

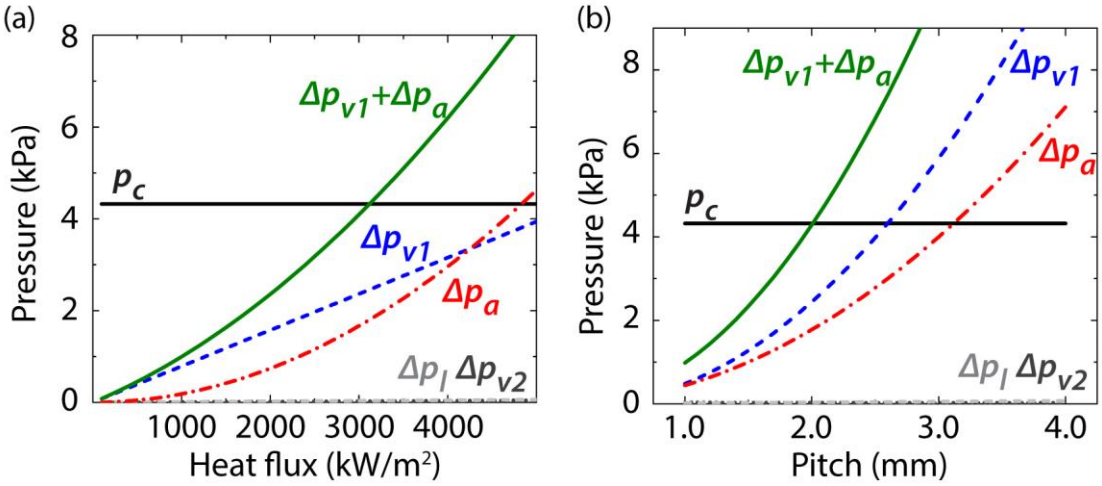

Figure 29 –(a) The pressure drop estimation as a fuction of heat flux for 2.0 mm pitch in Figure 26 and (d) the pressure drop estimation as a fuction of pitch for the heat flux of 3100 kW/m^2.

The pressure drop of each component in Eq.4.5 was estimated as a function of the heat flux (Figure 29a). The sample parameters were used in the analysis as follows: 1.5 mm microporous coating thickness, 1.5 mm channel depth, 2.0 mm channel pitch and 0.35 mm channel width, which is the simplified model of the 2.0 mm pitch sample in Figure 29b. The dominant pressure drop occurs by the vapor flow through the pores, Δp_{v1}, and by the acceleration pressure drop, Δp_a. Therefore, the growth of the vapor layer is believed

due to them. However, the analytical vapor-layer heat flux is around 3100 kW/m^2, which is much larger than the experimental vapor-layer heat flux, 997.4 kW/m^2. The discrepancy is possibly caused by non-uniform heat flux and pore size distribution: A uniform heat flux over the surface was assumed in this analysis, however, practically the heat flux is locally amplified at the site of the bubble nucleation. Also, the pore size is distributed due to the random packing of the particles, and therefore the low capillary pressure at the large pore does not restrain the growth of the vapor layer. Since the pressure drop of the lateral vapor flow, Δp_{v1}, is one of the main reason of vapor layer growth, it is intuitively expected that the smaller pitch is the better for the enhancement. The analysis also presents that the pressure drop is reduced as the pitch decreases (Figure 29b), which prevents the growth of the vapor layer and enhances both CHF and HTC. For the analysis, the fixed heat flux of 3100 kW/m^2, 1.5mm microporous coating thickness, 1.5 mm channel depth, and 0.35 mm channel width were used. The analysis agrees with the experiment of the channel pitch variation in Figure 26 except one case: The result of 1.5 mm pitch does not show a meaningful enhancement compared to that of 2.0 mm pitch, which may be connected to the characteristic shown in the channel width variation in Figure 27. Since the travel distance of the lateral vapor flow is directly proportional to the width of the microporous posts, which is the subtraction of the channel width from the channel pitch, a decrease in the pressure drop is expected as the width of the microporous posts decrease. Nonetheless, the experimental result shows very similar behavior in terms of HTC, which indicates the characteristic of the vapor layer growth is similar as well. The result implies that an upper limit of the enhancement exists by decreasing the pitch (or width of the microporous posts). The reason is not well understood yet. The growth of the vapor layer in the microporous

surfaces even with the vapor channels is evident based on the analysis and the experiment, and therefore we believe that CHF occurs by the dryout of the microporous coatings like the plain microporous surfaces.

4.2.4 Hydrodynamic Instability Aspect

Although the CHF is believed to be caused by the dryout of the microporous coatings, the theoretical CHF by hydrodynamic instability was studied using Eq.4.1 to understand the CHF mechanism more clearly. Assuming that the modulated wavelength, λ_m, is the same as the channel pitch, the theoretical CHF by hydrodynamic instability is computed to be 2808.3 kW/m^2 using 2.0 mm pitch for water at 50 kPa. However, the experimental CHF of 2.0mm pitch is 3487.6 kW/m^2 from the experiment (Figure 26), which is even larger than the theoretical limit. For all other cases in the channel pitch variation, the experimental CHFs are larger than the theoretical hydrodynamic instability limits. The possible reason is that the practical formation of the wavelength is closer than the channel pitch since the vapor channels cross each other perpendicularly. The decrease in CHF in the channel width variation (Figure 27) may be associated to the hydrodynamic instability as well. By Zuber's study [22], the wavelength on the flat surfaces is determined spontaneously to be two times of vapor jet diameter as well as in Liter and Kaviany's study [51] on the patterned microporous surfaces. In the present study, the diameter of the vapor jet is affected by the channel width while the wavelength was formed closer than the pitch (2.0 mm), and therefore, 1.0 mm channel width would present a significant decrease in CHF compared to the other channel widths. Additional study is required to validate the current explanation using the structure that can define the wavelength more clearly, such as the hole-type vapor channels.

4.2.5 Enhanced Structures to Increase Heat Transfer Coefficient

Regardless of the ambiguity in the hydrodynamic instability analysis, it is obvious that the boiling characteristic of the microporous surfaces with the vapor channels is largely governed by the growth of the vapor layer. Although the fabrication of the vapor channels in the microporous coatings significantly enhances both CHF and HTC, a decrease in HTC was observed with an increased heat flux, inferring that the vapor layer is still formed in the microporous coatings. Based on the analysis, the vapor-layer formation despite the vapor channels was possibly caused by the pressure drop of the lateral vapor flow through the pores or by the acceleration pressure drop due to the phase change. Since the method to decrease the pitch of the vapor channel in the microporous coatings shows the upper limit of the enhancement, alternative approach has been made by fabricating the vapor channels in the solid Cu: The solid channel provides shorter distance of the lateral vapor flow as well as space to reduce the acceleration pressure drop. The schematics and the SEM images of the structures are shown in see Figure 30 and the dimensions are listed in Table 7. Two different structures were examined: Type 1 has straight channels both in the solid Cu and in the microporous coatings, which are perpendicular each other. For the reference, the same structure without the solid channels was tested and compared. Type 2 has two-directional channels in the solid Cu, and has hole-shape channels in the microporous coatings. Different shapes of the vapor channels in the microporous coatings other than those in the parametric study were considered due to the difficulties in sample fabrication. The experiment was conducted for DI water at 1 atm. The surface superheats of the both enhanced structures were estimated from the temperature at the bottom of the solid channels.

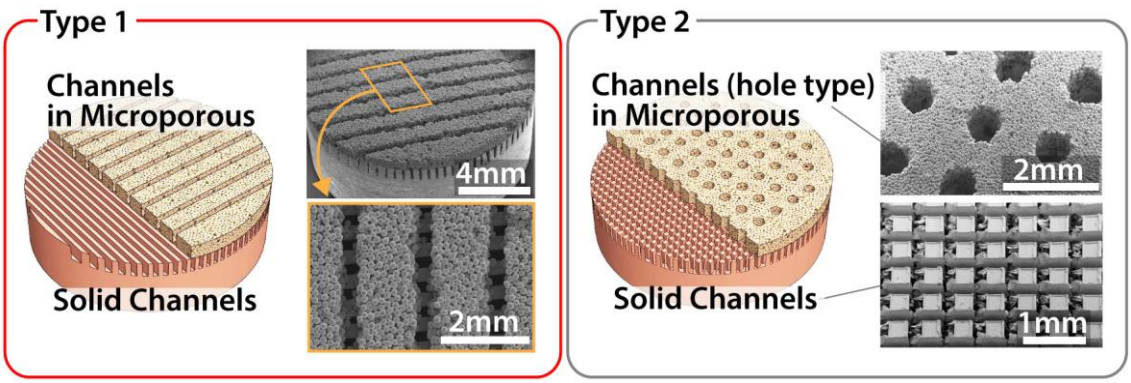

Figure 30 – Enhanced structures to increase HTC at high heat fluxes. Type 1 has one directional straight channels both on the solid and microporous surfaces, which are perpendicular each other, and Type 2 has two directional straight channels in solid surface and hole type channels in microporous surfaces.

Table 7 – Dimensions of the enhanced structures

Units (mm)	**Solid Cu**	**Microporous Coatings**	
	Channel Depth / Width / Pitch	**Thickness**	**Channel (Hole) Depth / Width(Dia.) / Pitch**
Ref. for Type 1	None	1.0	1.0 / 0.35 / 1.50
Type 1	1.0 / 0.20 / 0.50	1.0	1.0 / 0.35 / 1.50
Type 2	1.0 / 0.20 / 0.50	1.0	1.0 / (0.50) / 1.50

Type 1 structure exhibits 133.3 kW/(m^2K) in average HTC, which is a 29% enhancement compared to that of the reference structure, especially pronounced in high heat flux. The enhanced structure exhibits almost constant HTC from a heat flux of 1000 kW/m^2 to 3000 kW/m^2, validating the present explanation, while the reference structure shows a continuous decrease in HTC as heat flux increases. A schematic comparison between Type 1 and its reference structure is shown in Figure 32. The minimum distance of the vapor flow is 0.58 mm in the reference structure while that of the enhanced structure

is 0.15 mm. Due to the short flow distance, the vapor flows into the solid channel first, and then flows out of the structure through the channels in the microporous coatings. The flow pressure drop through the solid channel can be neglected since the hydraulic diameter of the solid channel, 0.33 mm, is much larger than that of the pores, 69 μm. The slight decrease in HTC after the maximum value around the heat flux of 800 kW/m^2 would be due to the formation of an initial vapor layer as the vapor fills the solid channels establishing the vapor escape path. Although a slight decrease in CHF was observed for Type 1 to be 3327.4 ± 110.3 kW/m^2, it is still within the measurement uncertainty compared of the reference value. Since the CHF was suddenly occurred without showing the characteristic of the vapor-layer growth, it is believed to be caused by hydrodynamic instability.

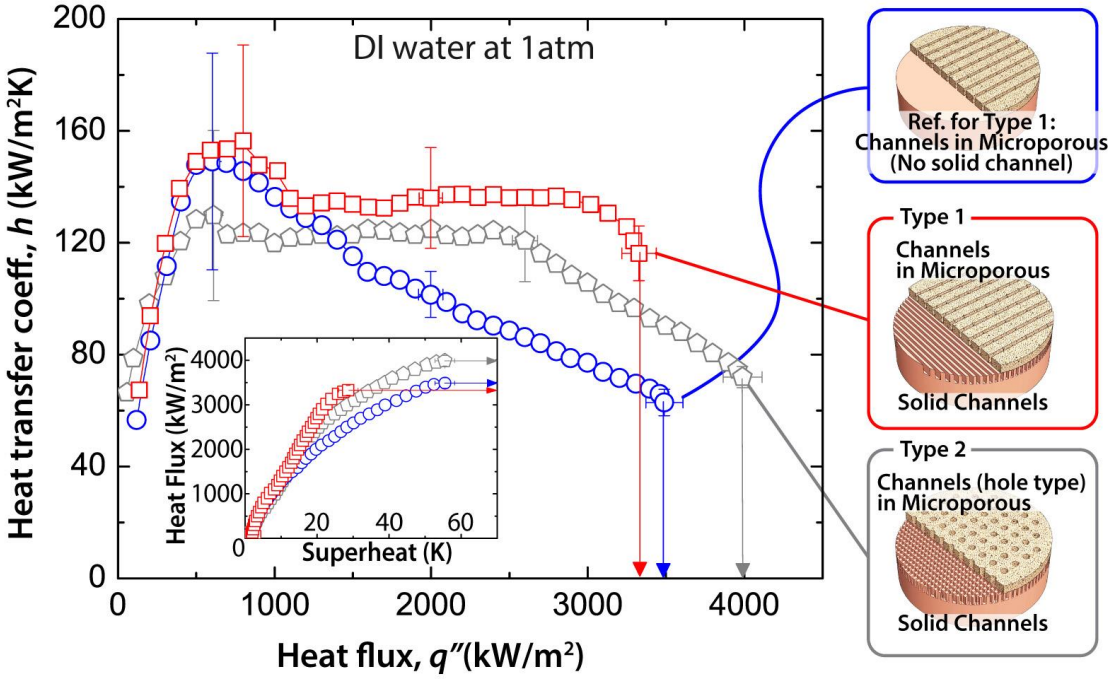

Figure 31 – Enhanced structures to increase HTC at high heat fluxes. The experiment was conducted for DI water at 1 atm. The arrow denotes that CHF was reached.

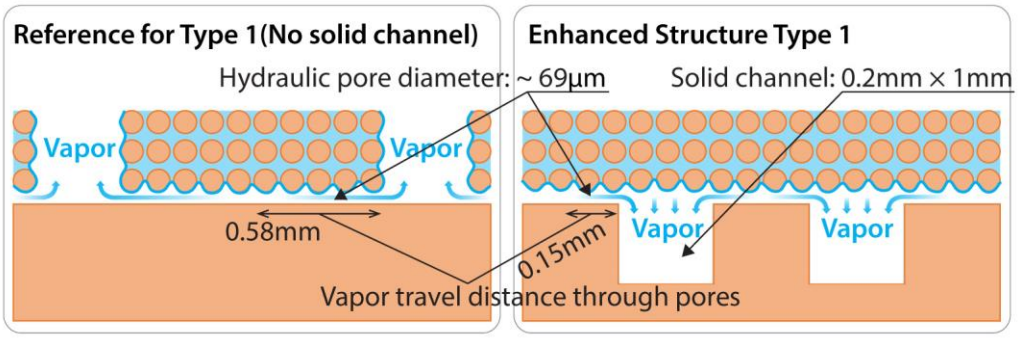

Figure 32 – A schematic of the cross-section of the Type 1 enhance structure and the reference structure.

Type 2 structure exhibits 111.0 kW/(m^{2}K) in average HTC, and the value is almost constant at low and medium heat flux. However, a decrease in HTC is observed as the heat flux exceeds 2500 kW/m^2, indicating that the vapor layer forms and grows in the microporous coatings. The possible reason of the vapor-layer growth is the imperfections of the solid channels—a lot of burrs in solid channel were created during the fabrication of two directional channels, which could not be easily removed, and may interrupt the vapor flow. A slightly lower HTC of Type 2 compared to Type 1 is thought to be due to the reduction of heat flux area in the solid Cu as well as in the contact between the solid Cu and the microporous coatings. The CHF of Type 2, 3989.3 ± 118. 0kW/m^2, is possibly caused by the dryout of the microporous coatings since the characteristic of the vapor-layer growth is observed at the heat flux larger than 2500 kW/m^2. Also, CHF by hydrodynamic instability is easily estimated since the hole-type vapor channels generate a very controlled pattern of the flow, to be to be 4292.4 kW/m^2 with λ_m = 1.50 mm for water at 1atm, which is larger than the measured CHF.

4.2.6 Comments on the Previous Studies

In Liter and Kaviany's study, one experiment (the coating thickness is eight times of the particle diameter, $\delta = 8d_p$) agreed well with their model while the other ($\delta = 6d_p$) did not. Since the slope change is not clearly observed in the boiling curve, the experimental CHF is believed to occur by hydrodynamic instability. The possible reason of the discrepancy is the thin thickness of the patterned microporous coatings, $6d_p$, which is close to the optimal thickness, and therefore the modulation of wavelength did not occur as intended due to the non-uniform evaporation line along the thickness. An increase in the coating thickness will help to control the wavelength along the surface pattern, however, may induce the growth of the vapor layer.

In Mori and Okuyama's study, since neither the slope change in the boiling curve nor the decrease in HTC was observed, the CHF did not occur by the dryout of the porous structure. The measured CHF decreases as the porous thickness increases, which is contrary to the present study in Chapter 3, and therefore they possibly measured the vapor layer heat flux rather than CHF. Since the ceramic porous structure is expected to have very low thermal conductivity, the elevated evaporation line due to the vapor layer would cause a significant increase in the surface superheat, which may cause a confusion in their measurement. Nevertheless, the measured values are too large to be a vapor-layer heat flux considering the pore size and the porous thickness. The possible explanation would be that a few microns gap was introduced between the porous structure and the heater surface since it was attached to the heater surface by pressing it using a wire net, and that the gap behaves like the solid channel under the microporous coatings in the enhanced structure. This would be possible even with a few micron gaps because the pore radius is very small—the average

and the median pore radius in their study are 37 nm and 130 nm respectively. The experimental study regarding loop heat pipes also supports the present explanation[62] in that the heat transfer coefficient was maximized when introducing a 20 μm gap between the wicks (1.2 μm of the mod pore radius) and the evaporator surface.

4.3 Summary

This chapter has presented that the enhancement in boiling heat transfer of the microporous surfaces can be achieved by preventing the growth of the vapor layer in the microporous coatings, which can be accomplished through the fabrication of the vapor channels. The experimental parametric study reveals that both CHF and HTC increase as the channel depth increases and as the channel pitch decreases. The effect of the channel width is not clearly understood, but the wide channels around half of the channel pitch result in a decrease of CHF. A significant enhancement has been achieved through the fabrication of the vapor channels in microporous coatings, up to 3547.5 ± 117.8 kW/m^2 in CHF and 89.9 kW/(m^{2}K) in average HTC for DI water at 50 kPa, which is a 88 % enhancement in CHF and a 254 % enhancement in average HTC compared to those of the plain microporous surfaces, and a 347 % enhancement in CHF and a 307 % enhancement compared to those of the flat surfaces. The enhancement is a comparable HTC to that of the optimum thickness along with more than twice larger CHF.

Despite the significant enhancement, the characteristic of the vapor-layer growth has been observed with the vapor channels. The analysis reveals that the growth of the vapor layer is caused by the lateral vapor flow through the pores as well as by the acceleration of the vapor flow due to the phase change. Although the distance of the lateral vapor flow can

be reduced with a decrease in the channel pitch, the upper limit of the enhancement was observed experimentally and difficulties in the fabrication exists as well. The fabrication of additional vapor channels in the solid Cu resolves the issue by providing a shorter distance of the lateral vapor flow as well as a space to reduce the acceleration pressure drop, which was validated through the experiment that presents a relatively constant HTC throughout the heat flux. Although the analytical determination of the channel dimension is complicated due to the locally amplified heat flux, the present study indicates that the length scale (the pitch and the hydraulic diameter) of the solid channels is less than a few hundred microns to prevent the vapor-layer growth with the present porous structures (50 – 70 μm in the pore diameter). The length scale is thought to be related to the pore size since the capillary pressure of the meniscus retains the growth of the vapor layer. The enhancement with the fabrication of the vapor channel is believed not only due to the removal of the vapor layer in the microporous coatings, but also due to the controlled flow-pattern of liquid and vapor that is related to hydrodynamic instability. We will discuss the effect of the hydrodynamic instability in Chapter 5.

CHAPTER 5. INVESTIGATION OF HYDRODYNAMIC INSTABILITY IN BOILING ON MICROPOROUS SURFACES

5.1 Background

A theoretical model of hydrodynamic instability during boiling on flat surfaces was developed by Zuber [22], postulating that transition and film boiling is caused by Kelvin-Helmholtz (KH) instability. The KH instability occurs when two fluids flow parallel to the interface, having different densities and velocities. A wave develops at the interface due to the velocity difference and the wavelength decreases as the velocity difference increases. The wavelength is called KH wavelength or λ_{KH}. If the wavelength reaches a critical value, $\lambda_{KH,crit}$, the interface becomes unstable and transition boiling occurs. The relationship between KH wavelength and the velocity of the vapor-jet, u_v, is given as Eq.5.1:

$$\lambda_{KH} = \frac{2\pi\sigma}{\rho_v u_v^2} \qquad \text{(Eq.5.1)}$$

where σ is the surface tension, ρ_v is the density of vapor, and u_v is the velocity of vapor. For a circular jet, the critical KH wavelength is reached when it becomes equal to the circumference of the jet as Eq.5.2:

$$\lambda_{KH,crit} = \pi D \qquad \text{(Eq.5.2)}$$

where D is the diameter of vapor-jet. Therefore, the critical vapor velocity, $u_{v,crit}$, that develops KH instability is obtained from Eq.5.1 and Eq.5.2 as shown in Eq.5.3:

$$u_{v,crit} = \left(\frac{2\sigma}{\rho_v D} \right)^{1/2} \qquad \text{(Eq.5.3)}$$

To estimate the heat flux that corresponds to the critical vapor velocity, a unit cell of liquid and vapor flow needs to be defined. Although the vapor jet develops randomly on the surface, it was assumed that the jets are developed with a certain regularly spaced distance. Therefore, a square unit cell that has a side length of λ_{RT} was considered as shown in Figure 33a. The Rayleigh-Taylor (RT) wavelength, λ_{RT}, will be defined later.

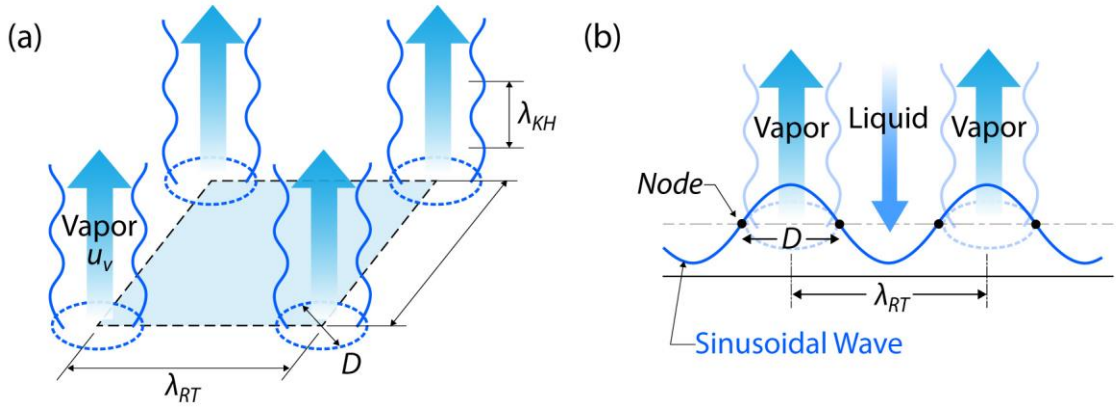

Figure 33 – (a) A schematic of a unit cell used in the CHF estimation by Zuber and (b) the relationship between the vapor-jet diameter and the wavelength.

The heat flux through a unit cell is given by the power used in the phase change, Q, over the unit area, A_o, as given in Eq.5.4:

$$q'' = \frac{Q}{A_o} = \frac{\dot{m}_v h_{fg}}{A_o} = \rho_v u_v h_{fg} \frac{A_v}{A_o} \qquad \text{(Eq.5.4)}$$

where h_{fg} is the latent heat of vaporization, $\dot{m}_v$ is the mass evaporation rate, and A_v is the area of the vapor-jet on a unit cell. Zuber assumed that the diameter of the vapor-jet is half

of the RT wavelength near CHF, $\lambda_{RT} = 2D$, based on the experimental observation during transition boiling by Westwater and Santangelo [63] that showed that vapor rods departed by breaking at the nodes of sinusoidal waves of the vapor blanket (Figure 33b). Therefore, A_v and A_o are given as Eq.5.5 and Eq.5.6:

$$A_o = \lambda_{RT}^2 \tag{Eq.5.5}$$

$$A_v = \frac{\pi D^2}{4} = \frac{\pi \lambda_{RT}^2}{16} \tag{Eq.5.6}$$

Substituting Eq.5.3 and Eq.5.5 – Eq.5.6 into Eq.5.4, CHF on a flat surface is obtained as given by Eq.5.7:

$$q''_{CHF} = \frac{\pi}{8} h_{fg} \left(\frac{\rho_v \sigma}{\lambda_{RT}} \right)^{1/2} \tag{Eq.5.7}$$

Eq.5.7 was used by Liter and Kaviany [51] to predict CHF on their patterned microporous surfaces with a known modulated wavelength, λ_m which was substituted for the RT wavelength, λ_{RT}.

When vapor underlies the liquid, the interface becomes unstable with the development of the wavelength, and the vapor blanket breaks at the RT wavelength, given by Eq.5.8:

$$2\pi \left[\frac{\sigma}{g(\rho_l - \rho_v)} \right]^{1/2} \leq \lambda_{RT} \leq 2\pi \left[\frac{3\sigma}{g(\rho_l - \rho_v)} \right]^{1/2} \tag{Eq.5.8}$$

Although the RT instability is related to transition boiling, Zuber assumed that a similar phenomenon occurs near CHF, and determined the RT wavelength as shown in Eq5.9 to be around the arithmetic mean of the range given in Eq.5.8

$$\lambda_{RT} = 9\left[\frac{\sigma}{g\left(\rho_l - \rho_v\right)}\right]^{1/2} \qquad \text{(Eq.5.9)}$$

Substituting Eq.5.9 into Eq.5.7, Zuber's correlation in Eq.1.1 is obtained. Although Zuber's correlation was developed with a lot of assumptions, numerous studies have reported good agreement between the theory and their experiment for the various working fluids on the flat surfaces. Therefore, we accept the assumptions and the derivation from Zuber's study, and will use them in this study to attempt to predict the CHF by hydrodynamic instability on the patterned microporous surfaces.

In Chapter 3 and 4, the CHF on the microporous surfaces was a result of dryout of the microporous coatings rather than hydrodynamic instability even with the fabrication of the vapor channels. The CHF by hydrodynamic instability may predict the limit of the CHF that is achievable, however, it has not been clearly observed in Chapter 4 because the modulated wavelength was not defined well with the straight vapor channels (see Figure 34a). Although Liter and Kaviany [51] showed that the CHF on the patterned microporous surfaces was reached by hydrodynamic instability, only one experimental validation was provided for a different working fluid (Pentane) than the current study. In this chapter, we will examine if the CHF by hydrodynamic instability can be reached on patterned microporous surfaces for DI water. Instead of the straight vapor channels, hole-type vapor channels will be used to define the wavelength more clearly (see Figure 34b). Since the

boiling characteristics in variation of the channel width in the Chapter 4 cannot be explained with viscous-capillary flow and that may be related to hydrodynamic instability, the effect of the channel size will be investigated. A parametric experimental study will be conducted with respect to the hole diameter with a fixed pitch, and then the optimal channel diameter will be found for the given pitch, which dictates the wavelength and controls CHF by hydrodynamic instability. Whether the experimental CHF is reached by hydrodynamic instability or not will be determined by comparing it to the theory as well as by investigating the characteristics of the vapor-layer growth in boiling curves.

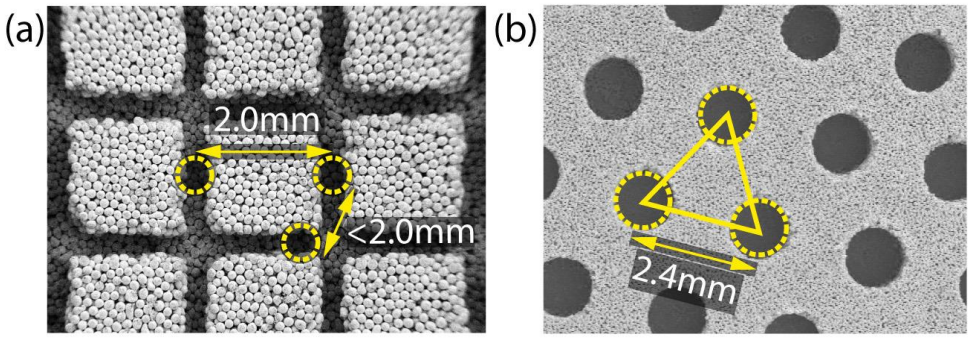

Figure 34 – (a) A SEM image of microporous surfaces with straight vapor channels and (b) microporous surfaces with hole-type vapor channels. While the vapor jet on the straight channels can be formed anywhere along the channels, the jet on the hole-type channel is expected to be formed only at the hole, clearly defining the wavelength.

5.2 Procedure, Result and Discussion

5.2.1 Triangular Unit Cell

The assumption of the square unit cell by Zuber provides a good approximation for the random formation of the vapor-jet on flat surfaces. Nonetheless, if a unit cell can be manipulated by controlling the vapor-jet formation, a triangular unit cell will present a higher CHF compared to a square unit cell since it has a larger vapor-jet area per unit area

with a given wavelength. A unit cell of an equilateral triangle with side length of λ_m is considered as shown in Figure 35. The unit cell area, A_o, and the vapor-jet area, A_v, is computed as Eq.5.10 and Eq.5.11 respectively:

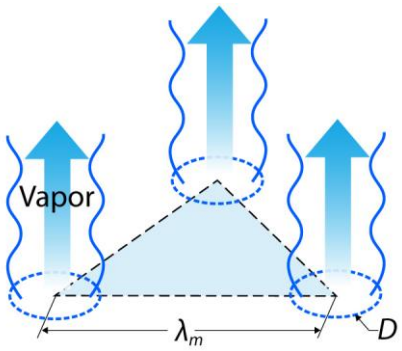

Figure 35 – A schematic of a triangular unit cell.

$$A_o = \frac{\sqrt{3}\lambda_m^2}{4} \quad \text{(Eq.5.10)}$$

$$A_v = \frac{\pi D^2}{8} = \frac{\pi \lambda_m^2}{32} \quad \text{(Eq.5.11)}$$

The critical heat flux on the triangular unit cell is given as Eq.5.12, by substituting Eq.5.10 and Eq.5.11 into Eq.5.4.

$$q''_{CHF} = \frac{\pi\sqrt{3}}{12} h_{fg} \left(\frac{\rho_v \sigma}{\lambda_m} \right)^{1/2} \quad \text{(Eq.5.12)}$$

The CHF by Eq.5.12 is larger than that on the square unit cell by 15.5 % for the same wavelength. In this study, samples will be fabricated based on a triangular unit cell, and the experimental results will be compared to the prediction by Eq.5.12.

5.2.2 Sample Preparation

The plain microporous surfaces were fabricated with the same procedure shown in the Chapter 2.1. The spherical copper particles of 63 – 75 μm in the diameter were used in this study instead those of 125 – 150 μm used in the previous study due to the improvement in the fabrication of round holes when the smaller particles were used. The thickness of the microporous coatings was fixed to be 1.5 mm for all samples. The vapor hole was fabricated on the plain microporous surfaces using a micro milling machine by removing the particles down to the copper surfaces. The pitch of the vapor hole is 1.4 mm for all samples, so the modulated wavelength is expected to be 1.4 mm as well. Five different diameters of the vapor hole, D_{ch}, were examined: 0.8, 1.3, 1.65, 2.1, and 2.2 mm, and the SEM images of the samples are shown in Figure 36.

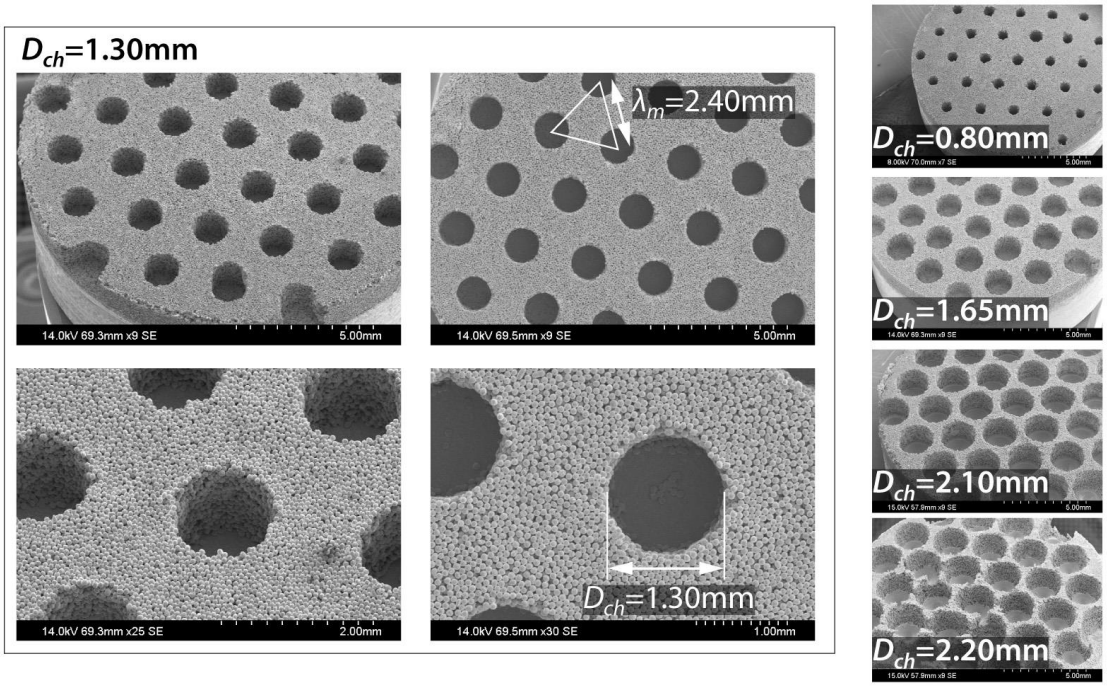

Figure 36 – SEM images of microporous surfaces with hole-type vapor channels

5.2.3 Visual Investigation of the Vapor Departure from the Vapor Holes

To compare the experimental CHFs to the theory, the modulated wavelength should be defined clearly. The wavelength is expected to be the same with the pitch of the vapor hole, however, the assumption is only valid when the vapor-jets form at the holes. The vapor departure was investigated using high speed imaging (see Figure 37): At a low heat flux around 15 kW/m^2, which is slightly higher than ONB, the vapor departure was only observed through the vapor holes even though not all the holes were active. At higher heat fluxes, although the imaging is not presented here, the vapor departure occurred at all the holes within the range of observation. Therefore, we will assume that the modulated wavelength is the same with the hole pitch in this study.

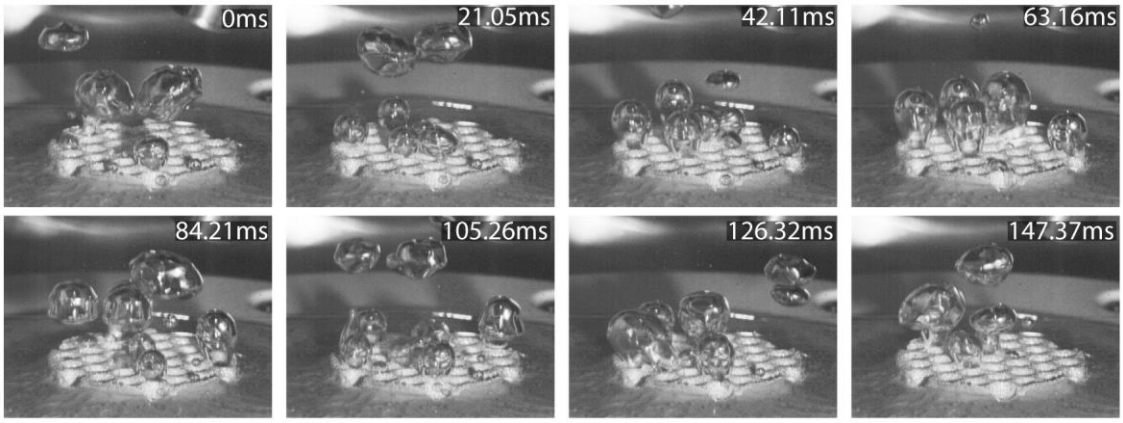

Figure 37 – High speed imaging of the vapor departure through the vapor holes. The experimental details are follows: D_{ch} = 2.10mm, q''~ 15 kW/m^2, for DI water at 1 atm.

5.2.4 Parametric Experimental Study with respect to Hole Diameter

A pool boiling experiment was conducted with variation of the vapor-hole diameter for DI water at 1 atm, and the result is shown in Figure 38—separate plots are provided for the thickness of 0.80 mm – 1.65 mm and 1.65 mm – 2.20 mm to present the trend clearly.

As the diameter increases up to 1.65 mm, both CHF and HTC increase significantly, but decreases after the hole diameter exceeds 1.65 mm. For the small hole diameters, 0.80 mm and 1.30 mm, the characteristic of the vapor-layer growth is clearly seen as the HTC decreases with an increased heat flux. Also, the experimental CHFs, 2097.1 kW/m^2 and 2986.2 kW/m^2 for 0.80 mm and 1.30 mm respectively, are much smaller than the theoretical prediction, 3918.8 kW/m^2 using Eq.5.12. Therefore, the CHFs for the small hole diameters are believed to be a result of the dryout of the microporous coatings. This is because the large pressure drop of the lateral vapor flow through the pores occurs with small diameter vapor channels introducing long travel distance of the flow. For the hole diameter of 1.65 mm, although the characteristic of the vapor-layer growth is seen, the CHF, 3802.7 kW/m^2, is close to the theoretical prediction with 3 % discrepancy. Therefore, the CHF is believed to be reached by hydrodynamic instability. For the large hole diameters, 2.10 mm and 2.20 mm, the CHF decreases as the hole diameter increases, however, the HTCs remain almost the same. This characteristic was also observed from the experiment of the channel width variation in Chapter 4—the CHF decreases while the HTC remains similar as the channel width increases. Since the characteristic of the vapor-layer growth is not seen for the hole diameter of 2.10 mm and 2.20 mm, the decrease in the CHF may be caused by hydrodynamic instability given that the large vapor-jets disturb the development of a proper sinusoidal wave. Otherwise, it may be caused by the limitation of the liquid supply. The further experiment and analysis are required to make it clear.

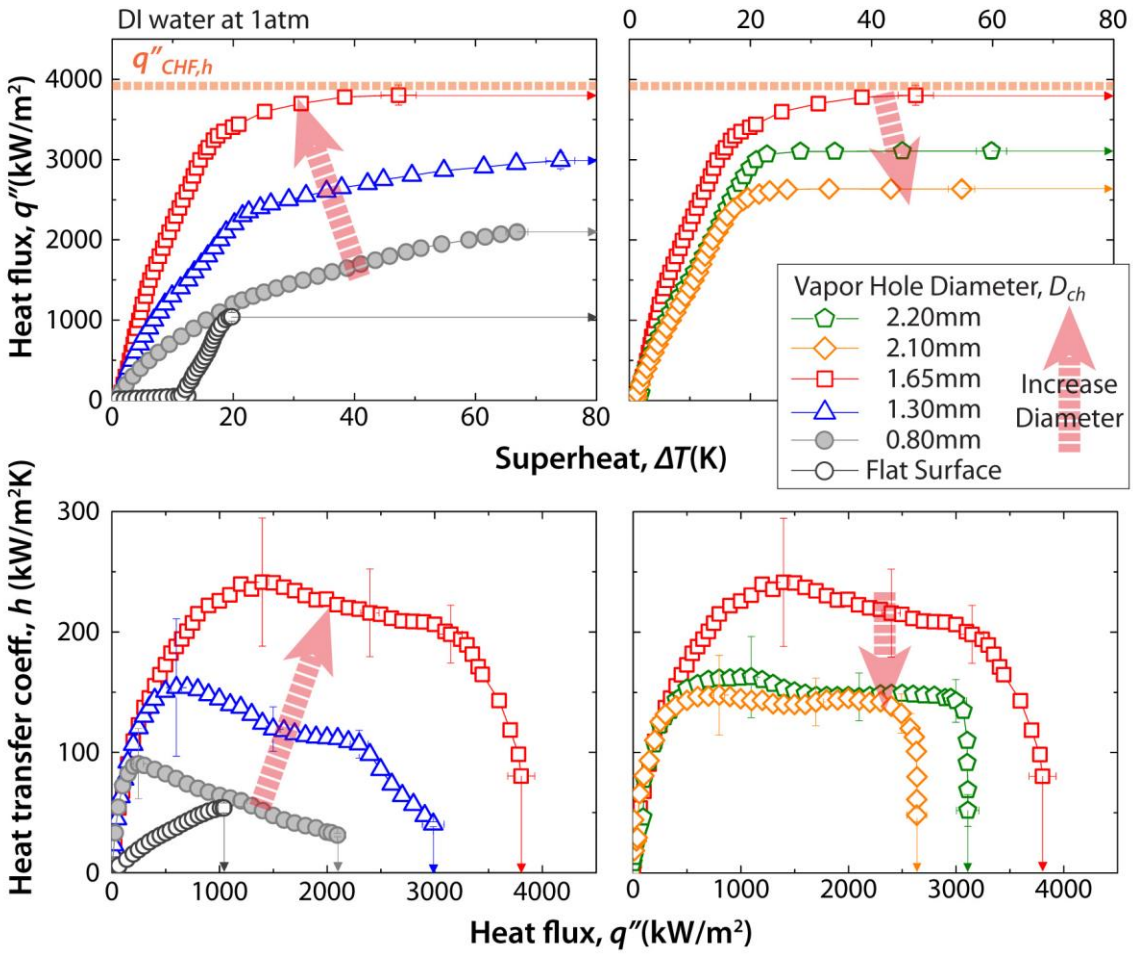

Figure 38 – Pool boiling curve and heat transfer coefficient of microporous surfaces with vapor holes with respect to the hole diameter. The experiment was conducted for DI water at 1atm, and the arrow denotes that CHF was reached.

Therefore, the vapor-hole diameter should be around or less than 1.65 mm not to disturb the development of the wavelength and/or not to limit the liquid supply, although the vapor-jet diameter is expected to be 1.2 mm, for the given wavelength of 2.4 mm by hydrodynamic instability analysis. In the view of viscous-capillary flow, the vapor-hole diameter should be larger than 1.65 mm to prevent the vapor-layer growth. Hence, the optimal hole diameter for the current structure can be determined to be around 1.65 mm. The CHF and the average HTC with the optimal hole diameter were obtained to be 3802.7

kW/m^2 and 175.3 $kW/(m^2K)$, corresponding a 265 % and 426 % enhancement compared to those on flat surfaces respectively. Since the characteristic of the vapor-layer growth is still seen with the optimal hole diameter, additional channel fabrication in the solid surface will improve the HTC at high heat flux as shown in Chapter 4.2.5.

Two characteristics that have not been seen in the previous chapters are shown with the present experiment. For the large hole diameters, 2.10 mm and 2.20 mm, the superheat continuously increased around CHF without increasing the heat flux, and then a sudden transition boiling occurred with a small increase in the heat flux. This is thought to be related to hydrodynamic instability but is not well understood yet. Another characteristic is shown with the vapor-layer growth for the hole diameter of 1.30 mm and 1.65 mm: The decrease in HTC was seen with two slopes in the plot of HTC vs. heat flux. While the first decreasing slopes are similar to those in the previous chapters, the second decreasing slopes are steeper than those. This would be because the dominant pressure drop of the viscous-capillary flow changes with the heat flux. Figure 29a shows the pressure drop estimation as a function of heat flux—although the geometry is different, we can get a general idea of the pressure drop. While the vapor flow through pores causes the most dominant pressure drop at low heat flux, the acceleration pressure drop becomes more dominant at high heat flux. This is because the acceleration pressure drop is proportional to the square of the heat flux while the flow pressure drop is proportional to the heat flux. Therefore, the second decreasing slope is believed to be the regime that the acceleration pressure drop becomes dominant, which is pronounced at high heat flux with small pore size.

The theoretical CHF by hydrodynamic instability was computed as a function of the wavelength with respect to two different unit cells (see Figure 39). The effectiveness

of a triangular unit cell can be validated with the present result: the CHF of the present structure (λ_m = 2.4 mm and D_{ch} = 1.65 mm), 3918.8 kW/m^2, exceeds the theoretical prediction using a square unit cell 3393.8 kW/m^2 by Eq.4.1, but is comparable to the prediction using a triangular unite cell, 3918.8 kW/m^2 by Eq.5.12. A further validation can be provided with the experiment using a square unit cell with the same wavelength and hole size. A high CHF by hydrodynamic instability is achievable with a small modulated wavelength. For a 0.5 mm wavelength, the CHFs by hydrodynamic instability are expected to be 8586 kW/m^2 for the triangular unit cell and 7435 kW/m^2 for the square unit cell. The minimum value of the wavelength is not yet understood but is also limited by the fabrication technique.

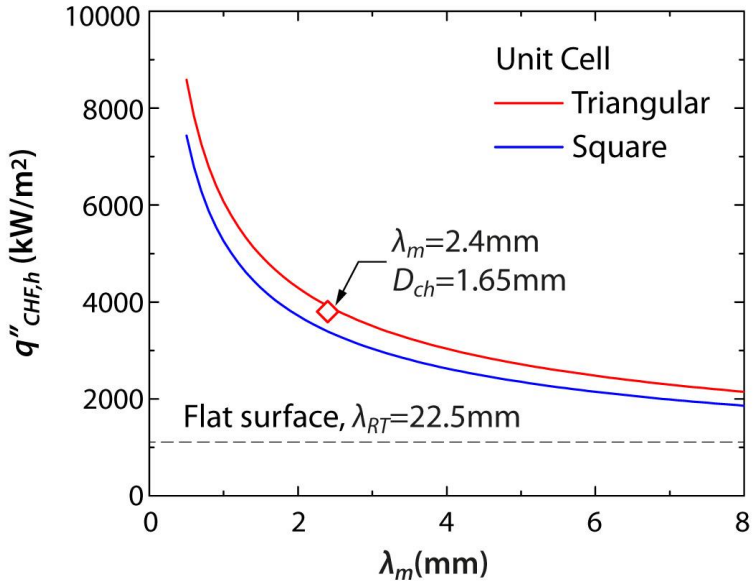

Figure 39 – The CHF by hydrodynamic instability as a function of the wavelength for water at 1 atm.

5.3 Flow Control on Flat Surfaces

The boiling enhancement using a flow control on flat surfaces was studied by Rahaman *et al*. [47]. The flow control was achieved by embedding lines of a low-conductivity epoxy into a copper substrate (see Figure 40a). They conducted an experimental parametric study in variation of the pitch for DI water at 1atm, and showed that the 2.4 mm pitch maximizes the enhancement both in CHF and HTC. They stated that the maximum enhancement is achieved when the bubbles depart without coalescence, and therefore, the optimal pitch is the same with the bubble departure size. And then the bubble departure diameter was found using the correlations by Firtz [64] as well as Cole and Rohsenow [65] to be around 2.5 mm for water 1 atm. We assume that those predictions may provide the minimum departure size since experimental studies have shown that a significant variation in the bubble departure diameter from a millimeter to few centimeters [66, 67] as well as the present observation.

We believe that the enhancement in CHF is related to the modulated wavelength in the view of hydrodynamic instability, and investigated whether CHF by hydrodynamic instability can be achieved through wavelength control on flat surfaces. The measured CHF is around 2300 kW/m^2 for the 2.4 mm pitch in Rahman *et al.*'s study, the predicted CHF is 3394 kW/m^2 using Eq.4.1 with λ_m = 2.4mm. Like straight vapor channels in our study, since the wavelength is not well defined with their structure, we fabricated circular copper areas that are spatially arranged and tested (see Figure 40b): Seven circular copper posts (1.5 mm in diameter each) were fabricated with a 4.5 mm pitch on a triangular unit cell, and the outside of the posts were filled with an epoxy. And then, the top surface was sanded and flattened. The vapor departure only occurred on the copper surface for the present surface,

however, a significant degradation was seen in boiling heat transfer as if the experiment reaches the film boiling immediately after the ONB. This is believed due to the very low frequency of the bubble departure. The bubble growth was very fast when it is small, however, the growth slowed down significantly as the contact line of bubble reached the boundary of the copper surface. This is because most evaporation occurred in the liquid microlayer underlying the bubble and the large thermal resistance was introduced after the contact line reached the boundary (see Figure 40). With this respect, copper strip surfaces are better than circular surfaces since the liquid microlayer exists along the length of the strip and that a significant degradation was not seen in Rahaman's study.

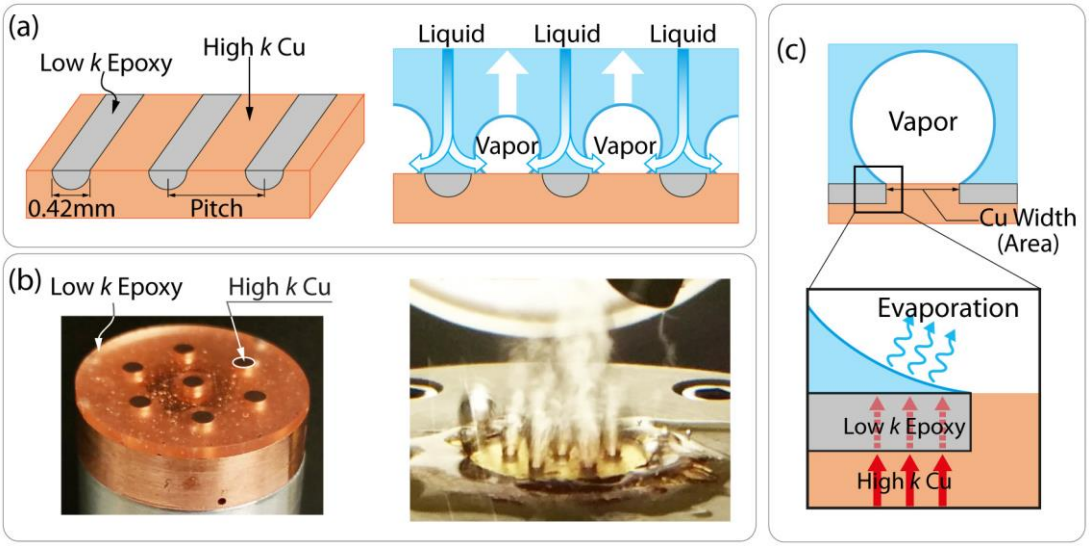

Figure 40 – (a) A schematic of bi-conductive surfaces for the flow control on flat surfaces [47], (b) the pictures of the present sample and the boiling experiment on it, and (c) a schematic to explain the slow-down of the bubble growth.

Although only one experiment was conducted on flat surfaces with the flow control, the enhancement limit on the flat surfaces can be understood. We believe that the CHF on flat surfaces is governed by hydrodynamic instability. Therefore, as the pitch decreases, the wavelength decreases as well as the hydrodynamic instability increases. However,

unlike the microporous surfaces, the minimum pitch is limited by the bubble departure size, which is directly related to the size of the copper area rather than the pitch. Since the diameter should be larger than 1.5 mm from the present study, and around 2.0 mm wide copper strip showed the maximum enhancement in Rahaman's study, the minimum diameter for the bubble departure can be determined around 2mm for water at 1atm. Assuming that the vapor-jet is the same size as the copper area, the minimum wavelength can be achieved on flat surfaces is around 4mm. Therefore, the hydrodynamic instability limit on the flat surfaces would be 2629 kW/m^2 using a square unit cell and 3036 kW/m^2 using a triangular unit cell (see Figure 41). Further enhancement may be achievable if a small bubble departure is obtained through surface treatment.

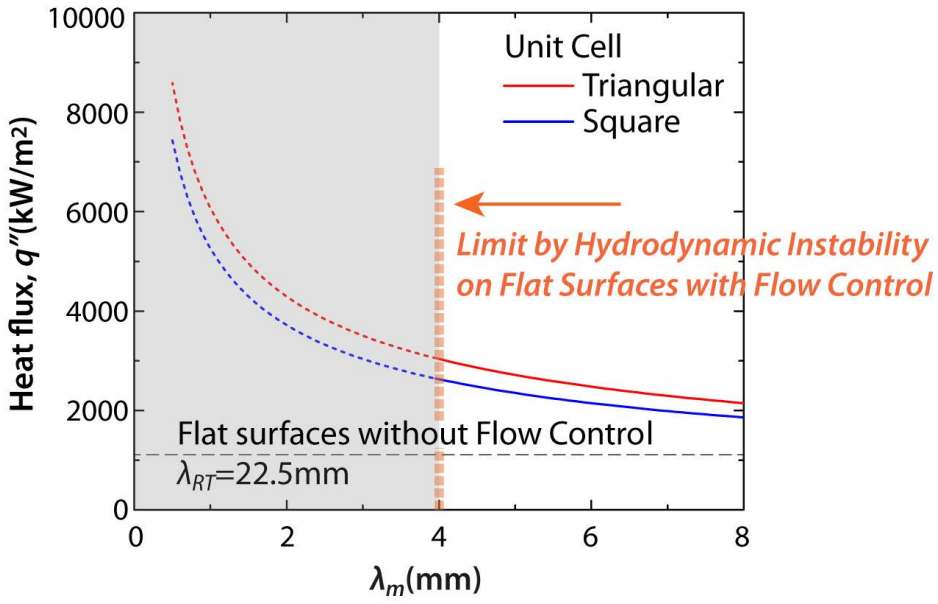

Figure 41 – The upper limit of CHF by hydrodynamic instability on flat surfaces for water at 1atm.

5.4 Horizontal Vapor Dissipation: Not Applicable to Unit Cell Analysis of Hydrodynamic Instability

Experimental studies have reported very high CHF as well as HTC, which that may exceed the hydrodynamic instability limit. Kandlikar showed 3000 kW/m^2 in CHF and 629 kW/(m^{2}K) in the maximum HTC by dissipating the vapor bubbles horizontally using a microfin structure having nucleation sites [68] (see Figure 42a). Bai *et al.* presented over 6000 kW/m^2 in CHF using microporous surfaces with the vapor channels in a solid surface [69], which is similar to the structure shown in Chapter 4.2.5 but the vapor dissipates horizontally through the solid channels without the vapor channels in the microporous coatings (see Figure 42).

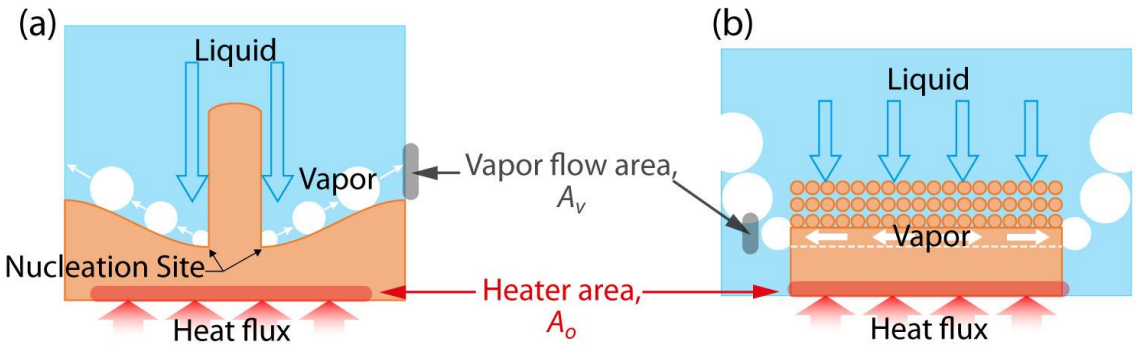

Figure 42 – (a) A schematic of the microfin structure used in Kandlikar's study [68] and (b) a schematic of the microporous structure used in Bai *et al.*'s study [69].

Recalling Eq.5.4, higher CHF is achieved with the larger area of vapor flow, A_v. The vapor-flow area is a part of the unit cell, and determined as its diameter is half of the side length of the unit cell. Therefore, the CHF is limited by hydrodynamic instability.

$$q'' = \rho_v u_v h_{fg} \frac{A_v}{A_o} \qquad \text{(Eq.5.4)}$$

In the structures shown in Figure 42, however, the vapor-flow areas are perpendicular and independent to the unit cell areas, therefore, the higher CHF can be achieved with an increased area of the vapor-flow. Also, the present hydrodynamic analysis using a unit cell is no longer valid, and a new analysis should be performed using Eq.5.3 and Eq.5.4 after defining a proper area of the liquid and the vapor flow.

Although a high CHF is achievable by dissipating the vapor horizontally, the method is limited by the heater size. The dimensions from the previous studies are approximately 1mm × 3mm in the area and 0.5 mm in the depth for the microfin structure (Figure 42a) and 10 mm in diameter for the microporous structure (Figure 42b). Enlarging the size of those structures causes the large heat spreading resistance as well as the large flow pressure drop, therefore an array of those structures will be required, which results in vertical vapor flow and provides the hydrodynamic instability limit.

5.5 Summary

This chapter presented that the CHF by hydrodynamic instability can be achieved on patterned microporous surfaces. The hole-type vapor channels were used to control the wavelength. Based on the understanding of Zuber's study, a triangular unit cell was suggested, which theoretically increases the CHF by 15.5 % compared to a square unit cell that was used in Zuber's analysis. A parametric experimental study was conducted with respect to the vapor-hole diameter with the fixed pitch for DI water at 1 atm. It was found that the small hole diameters induce the vapor-layer growth, which causes the CHF by the dryout of the microporous coatings, while the large hole diameters disturb the development of the proper wavelength in the view of hydrodynamic instability and/or limit the liquid

supply, which results in the decrease in CHF. The optimal hole diameter was determined around 1.65 mm for the given pitch, 2.4 mm, presenting 3802.7 kW/m^2 in CHF and 175.3 kW/(m^{2}K) in HTC, which is 265 % and 426 % enhancement compared to those of flat surfaces, respectively. The measured CHF agrees well with the prediction using λ_m = 2.4 mm showing 3 % discrepancy, therefore, the CHF is believed to be reached by hydrodynamic instability. The characteristics of the vapor-layer growth were still shown with the optimal hole diameter, and the fabrication of additional vapor channels in solid surfaces will resolve it, improving HTC at high heat flux. The CHF enhancement on flat surfaces using the flow control is also believed to be governed by hydrodynamic instability. Unlike microporous surfaces, the enhancement on the flat surfaces is limited by the bubble departure size, therefore, the minimum wavelength would be around 4 mm, which corresponds to less than 3000 kW/m^2 in CHF for water at 1 atm. For small heater sizes, approximately less than 1 cm^2, a higher CHF is achievable by dissipating the vapor horizontally with the separation of the vapor-flow area from the unit cell area. For large heater sizes, the unit cell analysis of hydrodynamic instability is valid providing the upper limit of CHF since the vertical vapor flow is necessary.

CHAPTER 6. HYSTERESIS, WETTABILITY, AND BOND NUMBER

6.1 Hysteresis

Hysteresis in the boiling curve was seen for microporous surfaces (see Figure 43). At the heat flux lower than the vapor layer heat flux, the hysteresis was not seen. At heat fluxes higher than the vapor layer heat flux, when decreasing the heat flux, the boiling curve moved toward ONB rather than following the path seen by increasing the heat flux. The hysteresis is related to the vapor-layer growth since it is seen above the vapor-layer heat flux. The physical mechanism can be more intuitively understood with the plot of HTC vs. heat flux. When decreasing the heat flux, HTC remains almost constant. Recalling the thermal resistance model in Figure 20, a constant HTC implies that the thickness of the vapor layer does not change. This can be explained with the hysteresis of the capillary pressure in microporous media.

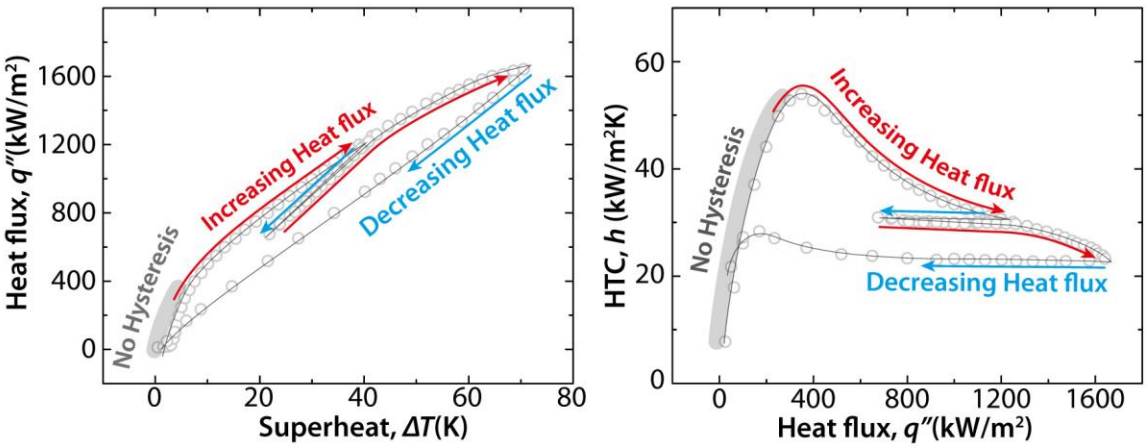

Figure 43 – Hysteresis in the boiling curve for microporous surfaces. The boiling curve of the 1.0 mm coating thickness sample in Chapter 3 is shown.

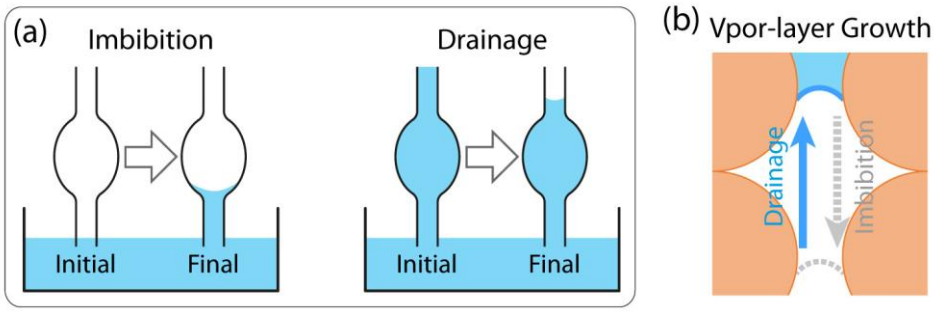

Figure 44 – (a) Capillary pressure hysteresis by imbibition and drainage process, and (b) a schematic of the vapor-layer growth that causes the hysteresis in boiling curve.

Typical porous media presents different capillary pressures during imbibition and drainage process due to the variation in the pore geometry (see Figure 44a). The same phenomena occur during the boiling heat transfer. The vapor-layer growth with increasing heat flux is governed by drainage process due to the pressure increase inside the meniscus. Once the meniscus advances to the upper pore, rolling back to the previous pore does not readily occur with decreasing heat flux due to the pore geometry, which is governed by imbibition process. This is additional evidence of the vapor layer growth in the microporous coatings during boiling heat transfer. Since hysteresis is disadvantageous when boiling heat transfer is applied to applications of electronics cooling, where the power fluctuates rather than monotonically increases, the removal of the vapor layer is important. All boiling curves presented in this study were obtained with increasing heat flux.

6.2 The Effect of Wettability

Nanoparticle coatings were considered since the enhancement in CHF has been presented on flat surfaces [12, 14]. The coatings are used to alter wettability and provide nanoporosity for wicking fluid. SiO_2 nanoparticles were deposited using a layer-by-layer method [70], which is based on a dip coating process, alternatively depositing negatively

charged particles and positively charged particles using electrostatic force. A calcination process after the coating removes organic material of the positive particles as well as provides strong adhesion between particles by fusing them. The calcination step was not conducted in the present study since it may affect the porosity of the microporous coatings as the process is performed at higher than 500°C for multiple hours. Nonetheless, the nanoparticle coatings remain after the boiling experiment, which was validated using SEM imaging and contact angle measurements. A bilayer consists of a single negative layer and a positive layer. For these samples, 6 bilayers and 12 bilayers were tested. The SEM image of the coated nanoparticles are shown in Figure 45a, and the average particle diameter was measured to be 25 nm. The static contact angle is significantly reduced to 10° on the nanoparticle coated Cu compared to that on bare Cu, 80° (see Figure 45b). Prior to applying the nanoparticles to the microporous coatings, a boiling experiment was conducted on the flat surfaces with the nanoparticle coatings (Figure 45c). The 6 bilayer SiO_2 coatings enhanced the CHF by 24 % but induced a slightly larger superheat, compared to those on the bare surface, which agrees well with previous studies [14].

The nanoparticle coatings were applied to the plain microporous surfaces that have thickness of 0.3 mm, 0.5 mm, and 1.5 mm. Full coverage of the nanoparticles throughout the microporous coatings was validated with SEM imaging and X-ray photoelectron spectroscopy (XPS) analysis. The boiling experiment was conducted for DI water at 50 kPa, and the results are compared with those of microporous surfaces without the nanoparticle coatings (see Figure 46). Unlike the results on the flat surfaces, the nanoparticle coatings show a negligible enhancement or a reduction in CHF within the uncertainty range (~ 5 %).

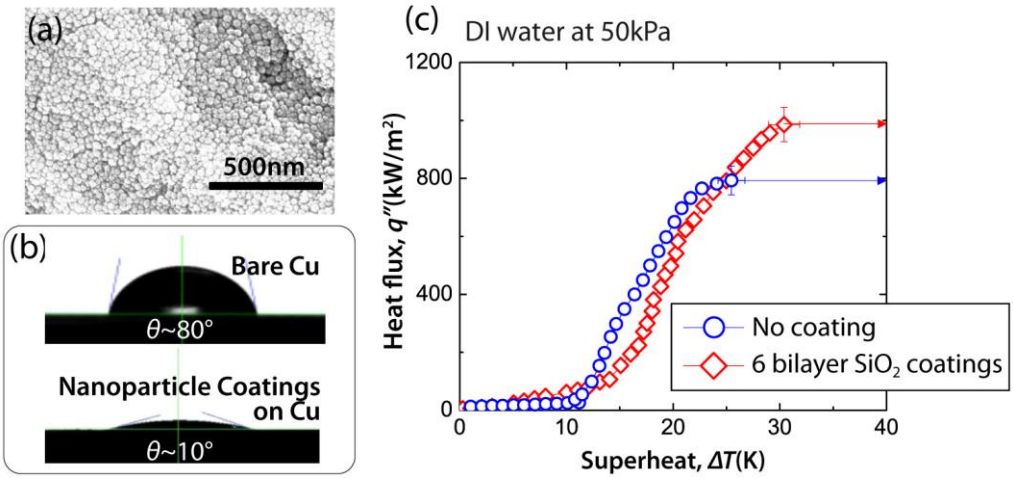

Figure 45 – (a) A SEM image of the nanoparticles coated on Cu, (b) contact angle measurement on bare Cu and on nanoparticle coated Cu, and (c) boiling curves of bare Cu and SiO_2 nanoparticle coated Cu.

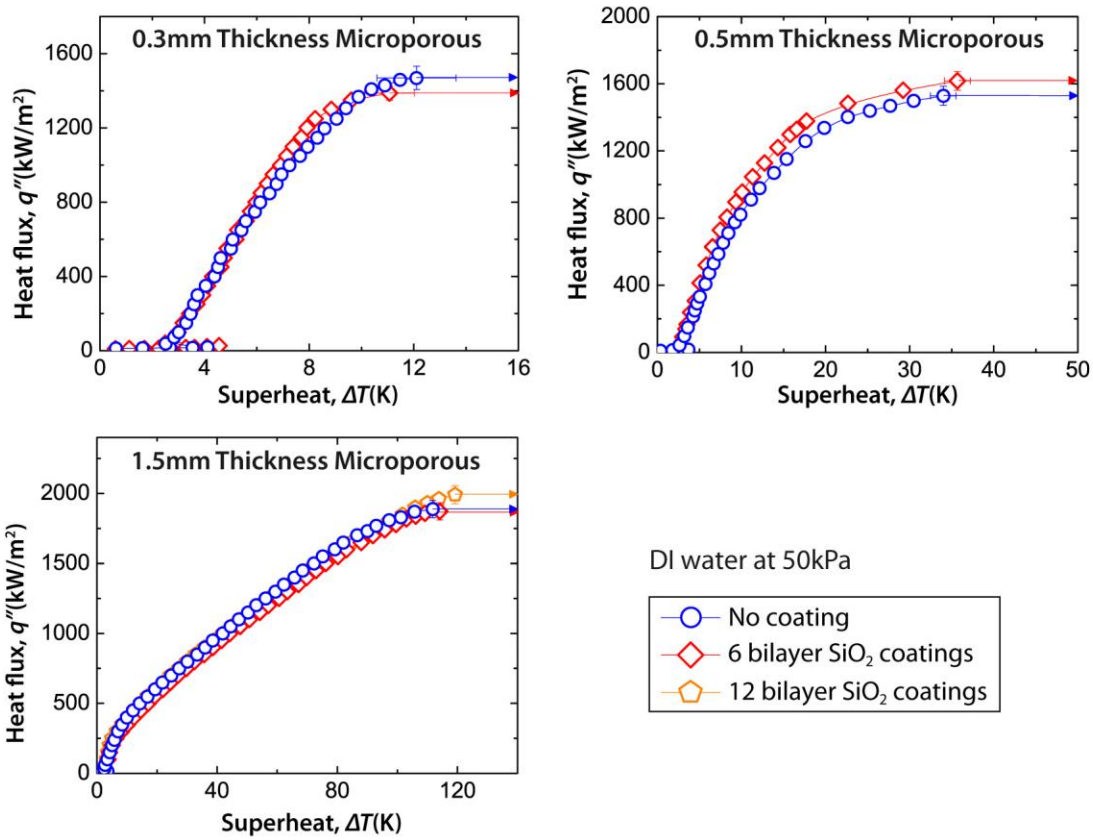

Figure 46 – Comparisons of boiling curves of the microporous surfaces with and without SiO_2 nanoparticle coatings.

Although the present explanation on the boiling mechanism is associated with the wettability in that the vapor layer growth is prevented by the capillary pressure, no meaningful enhancement was seen with the nanoparticle coatings. This is possibly caused by the following two reasons: The receding contact angle on bare Cu has reported from 0° – 70° [71-74] due to the native oxide layer and contaminants. The present measurement showed that the receding contact angle on flat Cu surfaces is less than 20° although it varies with the surface condition. Assuming that the receding contact angle on Cu particles is less than 20°, the difference in the capillary pressure between the bare surface (θ = 20°) and the nanoparticle coated surface (θ = 0°) is less than 6 % in the capillary tube (see Figure 47). Also, the difference becomes less than 4 % as the spherical geometry is considered. An insignificant enhancement or reduction around 5 % may be caused by those reasons.

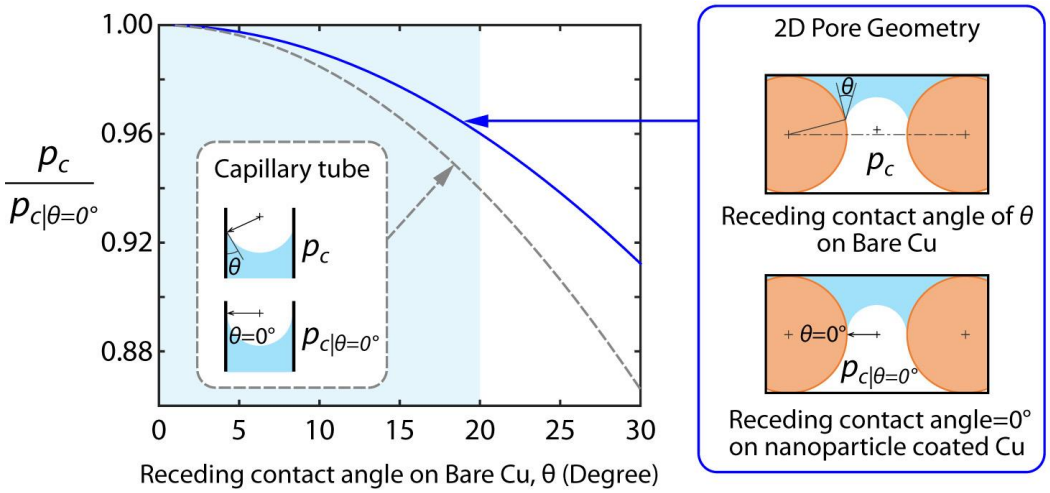

Figure 47 – A comparison between the capillary pressure on bare Cu and nanoparticle coated Cu: the capillary pressure on bare surfaces over the capillary pressure on nanoparticle coated surfaces (θ = 0°) was plotted as a function of receding contact angle on bare surfaces. Two geometries were considered: capillary tube (dashed line) and 2D circular surface (solid line). For the circular surface, 137.5 μm particle diameter and 69 μm space between the particles were assumed.

The capillary pressure estimation of heat pipes may be associated to the present explanation, which is generally estimated using a particle diameter (for wick structures sintered with spherical particles) [52], implying that the contact angle variation with different materials has insignificant effect. However, this is contradictory to the result of capillary pressure measurement using rate-of-rise method [75, 76] because the nanoparticle coated microporous media enhanced the capillary pressure by 2.5 times (see Figure 48). The possible explanation is that the capillary pressure hysteresis is amplified with the nanoparticle coatings as it improves an imbibition process while merely altering the drainage capillary pressure. The rate-of rise method measures imbibition capillary pressure and the vapor-layer growth during boiling is governed by drainage capillary pressure. A further investigation is required for the validation.

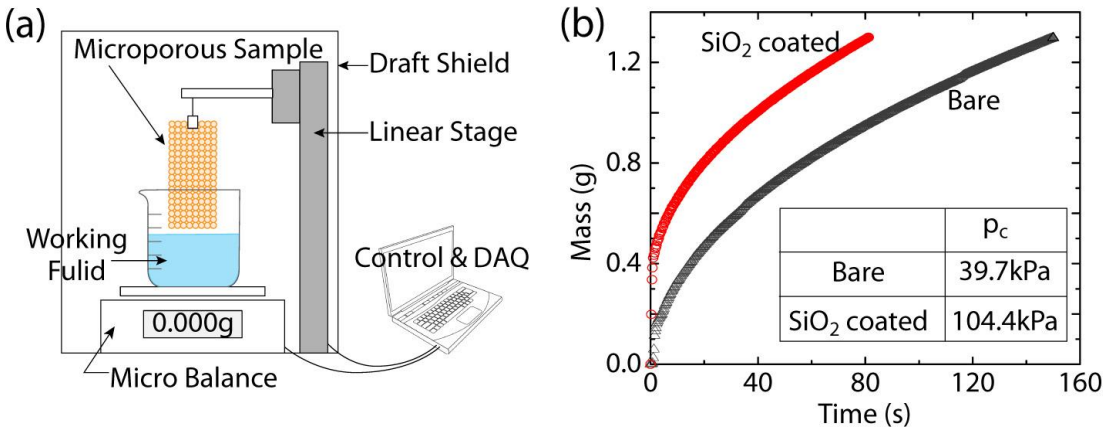

Figure 48 – (a) A schematic of the experimental setup for the rate-of-rise measurement and (b) the measurement and the capillary pressure estimation. The sample was fabricated by sintering spherical Cu particles of 53 – 63 μm in diameter. The porosity was estimated to b 0.475. Although the method has ability to estimate the permeability along with the capillary pressure, the constant permeability of 1×10^{13} m^2 was assumed due to the significant measurement uncertainty was introduced during the measurement.

6.3 Bond Number

Since the experiment and analysis in this study was conducted with respect to water, it is of interest to investigate whether the present study is still valid with other fluids or not. Kaviany [50] provided a good reference through a Bond number analysis using the experimental data of Fukusako *et al.* [49]. The Bond number, *Bo*, is a dimensionless number that measures the ratio of the body force to the surface tension force as shown in Eq.6.1:

$$Bo = \frac{g\left(\rho_l - \rho_v\right)L^2}{\sigma} \qquad \text{(Eq.6.1)}$$

where g is the gravitational acceleration, ρ is the density, σ is the surface tension, and the subscript, l and v, denotes liquid and vapor phase. L is the characteristic length. Kaviany defined the characteristic length as the square root of the ratio of the permeability, κ, to the porosity, ε, and therefore, the Bond number becomes as Eq.6.2:

$$Bo_{Kaviany} = \frac{g\left(\rho_l - \rho_v\right)\kappa/\varepsilon}{\sigma} \qquad \text{(Eq.6.2)}$$

Instead of using Eq.6.2, we will use a different characteristic length to provide more intuitive understanding. Eq.6.1 can be rewritten as Eq.6.3:

$$Bo = \left(\frac{L}{\lambda_c}\right)^2 \qquad \text{(Eq.6.3)}$$

where λ_c is the capillary length, which is defined as Eq.6.4:

$$\lambda_c = \sqrt{\frac{\sigma}{g\left(\rho_l - \rho_g\right)}} \qquad \text{(Eq.6.4)}$$

The capillary length is the maximum length that can maintain the spherical shape of the drops (Figure 49). For large drops, spreading occurs having a large radius of curvature, which significantly reduces the pressure difference that can be retained by the meniscus.

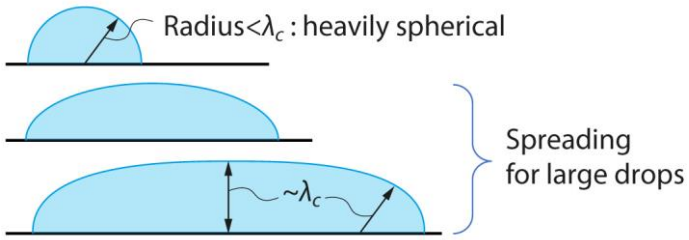

Figure 49 – Spreading of drops larger than capillary length.

The same phenomena occur during boiling on porous surfaces although the vapor is in high pressure in that case. If the pore size is larger than the capillary length, the meniscus does not retain the vapor layer, and therefore, the vapor will readily escape from the porous coatings. In that reason, we will relate the characteristic length to the pore diameter. Several different estimates of the pore radius are shown Eq.3.7 – Eq.3.9. We will use the hydraulic the pore diameter, d_h, as Eq.6.5:

$$L \sim d_h = \frac{2\varepsilon}{3\left(1-\varepsilon\right)} d_p \qquad \text{(Eq.6.5)}$$

where d_p is the particle diameter. Therefore, the *Bo* number in the present study is defined as:

$$Bo = \left(\frac{d_h}{\lambda_c} \right)^2 \qquad \text{(Eq.6.6)}$$

The effective radius in Eq.3.9 gives a comparable estimation in *Bo* number as well. In that way, the transition in the shape of the boiling curve occurs around 1, which is validated with the experimental data by Fukusako *et al.* Using Eq.6.6, the Bond number was computed with respect to several different working fluids (see Figure 50). The Bond number analysis shows that if the particle diameter is less than 700 μm, the shape of the boiling curves will resemble those of microporous surfaces in the present study for the all working fluids that are considered in Figure 50. It can be generalized that the vapor-layer growth necessarily occurs during boiling on microporous surfaces that have a pore size smaller than few hundred microns and have a coating thickness greater than the optimal thickness for typical working fluids.

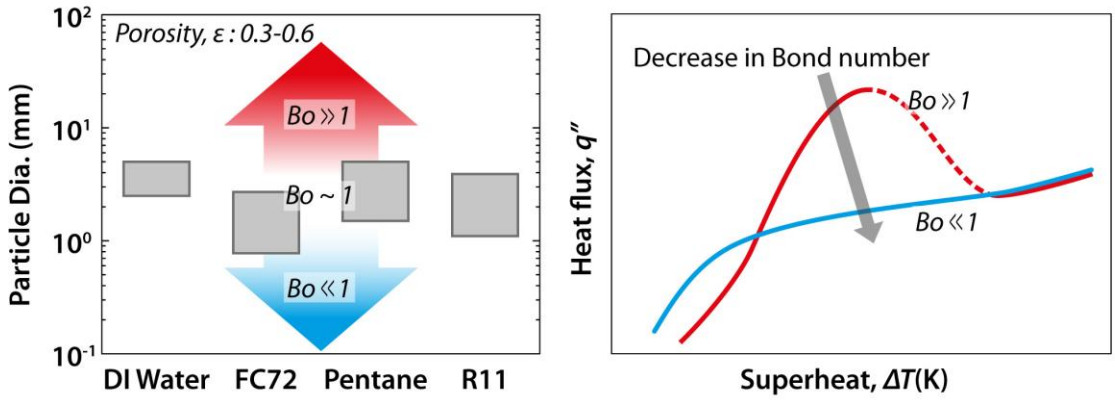

Figure 50 – Effect of the Bond number on the shape of boiling curve.

CHAPTER 7. CONCLUSION AND FUTURE WORK

7.1 Conclusion

In this study, the boiling characteristics of microporous surfaces have been explored and a better understanding of the boiling mechanism has been achieved based on the present experiment leveraging the theories used by previous studies. For plain microporous surfaces, the vapor-layer growth occurs in the microporous coatings, which significantly degrades HTC if the coating is thicker than the optimal thickness. Although the optimal thickness maximizes HTC, it has relatively low CHF compared to thick microporous coatings. Therefore, enhancing both CHF and HTC have been achieved with the fabrication of vapor channels by removing the vapor layer. The experimental parametric study has shown that both CHF and HTC are enhanced as the channel depth increases and as the channel pitch decreases. Nonetheless, the vapor channel fabrication in the microporous coatings has not completely removed the vapor layer, which is also limited by fabrication technique. The viscous-capillary analysis reveals that the vapor-layer growth is caused by the flow pressure drop through pores as well as the acceleration pressure drop due to phase change. A fabrication of additional vapor channels in solid surfaces beneath the microporous coatings helps to reduce both pressure drops, which also provides a benefit with easy fabrication. The CHF on the microporous surfaces practically occurs due to dryout of the microporous coatings, and the hydrodynamic instability provides the upper limit of CHF that can be achievable. To maximize CHF, the size and location of the vapor-jets should be controlled to reach the hydrodynamic instability limit as well as the vapor should be efficiently removed to prevent vapor-layer growth. The experimental study with

hole-type vapor channels has shown that the hydrodynamic instability limit can be achieved with the hole diameter of 1.65 mm and the wavelength (or pitch) of 2.4 mm for the present structure. The hysteresis in the boiling curve of the microporous surfaces is caused by the vapor layer growth due to the nonuniform pore geometry. The vapor-layer growth is expected to occur for microporous surfaces thicker than the optimal thickness regardless of the working fluids. Therefore, vapor channels are necessary for boiling on microporous surfaces.

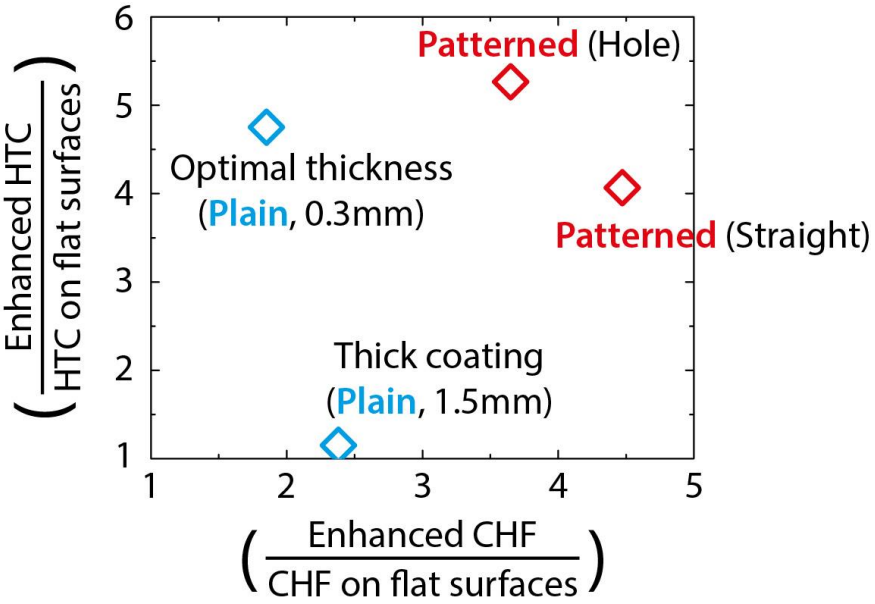

Figure 51 – Normalized enhancement in CHF and HTC. The patterned microporous surfaces are compared to the plain microporous surfaces with the optimal thickness and thick coating.

The enhancement using the patterned microporous surfaces are compared to that of the optimal thickness (see Figure 51). The maximum enhancement using the straight channels was achieved with 1.2 mm channel depth, 1.5 mm channel pitch, and 0.35 mm channel width, to be 3547.5 kW/m^2 in CHF and 89.9 kW/(m^{2}K) in average HTC for DI water at 50 kPa. increasing the CHF by 347 % and the average HTC by 307 % compared

to those of the flat surfaces. The maximum enhancement using the hole channels was achieved with 1.65 mm channel diameter and 2.4 mm channel pitch to be 3802.7 kW/m^2 in CHF and 175.3 $kW/(m^2K)$ in average HTC for DI water at 1 atm, increasing the CHF by 265 % and the average CHF by 426 % compared to those on the flat surfaces respectively. Since the straight channels are around the fabrication limit but the hole channels are not, a further enhancement is available using the hole vapor channels. Also, the vapor-layer growth was seen with the optimal hole channels, therefore, additional channel fabrication on the solid surface will enhance the HTC as well.

The contributions of this work are to provide the explanation of the boiling mechanism on microporous surface, which differs from previous studies, as well as to provide appropriate approaches for the enhancement with the experimental validation. The details include:

- This study has defined a vapor-layer heat flux, which differs from CHF.
- This study has shown that the CHF on microporous surfaces practically occurs by the dryout of the microporous coatings, and explained its physical mechanism.
- This study has shown that the vapor-layer growth is induced by the pressure drop of vapor flow through pores as well as by the acceleration pressure drop, neither of which was considered in previous studies.
- This study, based on the mechanism of vapor-layer growth, has suggested and experimentally validated the enhanced structures, which have additional vapor channels on solid surfaces.

- This study has suggested a triangular unit cell for hydrodynamic instability analysis, which theoretically increases the CHF by 15.5% compared to the conventional square unit cell.
- This study has shown that the hydrodynamic instability limit, which is the upper limit of CHF, can be achieved by modulating the wavelength of vapor-jets as well as by preventing the growth of vapor layer in the microporous coatings through the experimental study for DI water.

7.2 Future Work

Since patterned microporous surfaces significantly enhance boiling heat transfer both in CHF and HTC, it is of interest applying them to practical cooling applications that involve boiling heat transfer such as direct immersion cooling and thermosyphon. For example, to increase the efficiency of electric vehicles (EVs), an effort has been made to reduce the size and weight of inverters and converters, which necessarily causes large heat fluxes on them. Therefore, two phase heat transfer like thermosyphon is considered one of the promising solutions to remove such large heat fluxes. Integrating the patterned microporous surfaces to the evaporator of the thermosyphon will enhance the performance. Therefore, experimental validation of its performance is an interesting research subject. Also, since those cooling applications are frequently operated with dielectric fluids, an experimental investigation with respect to various working fluids will provide helpful information for the practical application.

The analysis conducted in this study can be applied to enhance the performance of heat pipes as well as vapor chambers. Although their operating mechanism differs from that of pool boiling as liquid level remains at the top of the wick structures, we believe that the viscous-capillary analysis in this study is still valid for them if sintered particle wicks are used. Therefore, the vapor-layer growth occurs in the wicks during their operation, which is induced by the pressure drop of the vapor flow through pores as well as the acceleration pressure drop due to phase change. Although the vapor channels are commonly used in loop heat pipes (LHPs), inappropriate dimensions and locations are typically seen such as few millimeter pitch with few micron pore size as well as the vapor channels in the middle of wicks. Those are against the understanding in this study, therefore, designing and positioning appropriate vapor channels in the wick structures based on the present understanding will enhance its performance.

APPENDIX A. PROPERTIES USED IN THE ANALYSIS

A.1 Temperature Dependent Thermal Conductivity of Copper

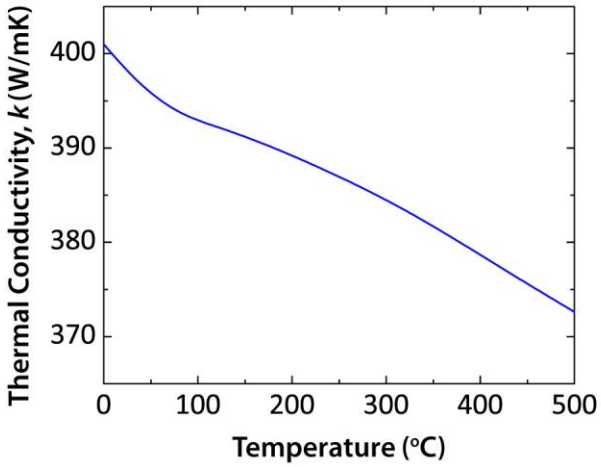

Figure A.1 - Temperature dependent thermal conductivity of copper[77]

A.2 Thermophysical Properties of the Typical Working Fluids

The properties are at the saturation condition.

Water [78]

Saturation Pressure, p (kPa)	**Saturation Temp., T_{sat} (°C)**	**Density (kg/m^3)**		**Latent heat, h_{fg} (kJ/kg)**	**Surface tension, σ (N/m)**	**Viscosity (μPa/s)**	
		Vapor ρ_v	**Liquid ρ_l**			**Vapor μ_v**	**Liquid μ_l**
50	81.32	0.3086	971.0	2304.7	0.0624	11.654	350.76
75	91.76	0.4510	964.1	2278.0	0.0605	12.007	309.94
101.3	100	0.5975	958.4	2256.6	0.0589	12.287	283.33

FC72 [79]

Saturation Pressure, p (kPa)	Saturation Temp., T_{sat} (°C)	Density (kg/m^3)		Latent heat, h_{fg} (kJ/kg)	Surface tension, σ (N/m)	Viscosity (µPa/s)	
		Vapor ρ_v	Liquid ρ_l			Vapor μ_v	Liquid μ_l
101.3	56	13.01	1620.9	84.73	0.00948	(5-15)*	447

**A viscosity of the vapor was assumed to be a typical range of values since it is unknown.*

Pentane [51]

Saturation Pressure, p (kPa)	Saturation Temp., T_{sat} (°C)	Density (kg/m^3)		Latent heat, h_{fg} (kJ/kg)	Surface tension, σ (N/m)	Viscosity (µPa/s)	
		Vapor ρ_v	Liquid ρ_l			Vapor μ_v	Liquid μ_l
101.3	36.05	3.00	610.2	358.2	0.0143	6.9	196

APPENDIX B. UNCERTAINTY ANALYSIS

The uncertainties were computed by the propagation of the measurement uncertainties.

B.1 Uncertainty Analysis for Porosity of the Microporous Coatings

The porosity of the microporous coatings, ε, is computed as:

$$\varepsilon = 1 - \frac{\rho_{Porous}}{\rho_{Cu}} \tag{Eq.B.1}$$

Since ρ_{Cu} is a constant, the propagation of the uncertainty becomes:

$$U_{\varepsilon} = \sqrt{\left(\frac{\partial \varepsilon}{\partial \rho_{Porous}} U_{\rho_{Porous}}\right)^2} = \frac{U_{\rho_{Porous}}}{\rho_{Cu}} \tag{Eq.B.2}$$

where U_{ξ} is the measurement or propagated uncertainty of ξ. The density the porous coatings are computed from the measurement quantities of the powder mass, m_{porous}, the coating diameter, d, and coating thickness, δ, as:

$$\rho_{Porous} = \frac{4m_{Porous}}{\pi d^2 \delta} \tag{Eq.B.3}$$

Therefore, the uncertainty of ρ_{Porous} is computed as:

$$\begin{aligned} U_{\rho_{Porous}} &= \sqrt{\left(\frac{\partial \rho_{Porous}}{\partial m} U_m\right)^2 + \left(\frac{\partial \rho_{Porous}}{\partial d} U_d\right)^2 + \left(\frac{\partial \rho_{Porous}}{\partial \delta} U_{\delta}\right)^2} \\ &= \frac{1}{\rho_{Porous}} \sqrt{\left(\frac{U_m}{m}\right)^2 + \left(\frac{2U_d}{d}\right)^2 + \left(\frac{U_{\delta}}{\delta}\right)^2} \end{aligned} \tag{Eq.B.4}$$

B.2 Uncertainty Analysis for Pool Boiling Experiment

The heat flux is computed using the thermal conductivity of copper, *k*, and the temperature gradient, *a*:

$$q'' = -ka \qquad \text{(Eq.B.5)}$$

Therefore, the uncertainty of the heat flux becomes:

$$U_{q''} = \sqrt{\left(\frac{\partial q''}{\partial k}U_k\right)^2 + \left(\frac{\partial q''}{\partial a}U_a\right)^2} = \sqrt{\left(\frac{U_k}{k}\right)^2 + \left(\frac{U_a}{a}\right)^2} \qquad \text{(Eq.B.6)}$$

U_k is assumed to be ±5W/mK. The temperature gradient is estimated using a simple linear regression as:

$$a = \frac{\sum_{i=1}^{n} x_i T_i - \frac{1}{n}\sum_{i=1}^{n} x_i \sum_{i=1}^{n} T_i}{\sum_{i=1}^{n} (x_i)^2 - \frac{1}{n}\left(\sum_{i=1}^{n} x_i\right)^2} \qquad \text{(Eq.B.7)}$$

The measured quantities are the position, *x*, and the temperature, *T*, therefore U_a becomes:

$$U_a = \sqrt{\sum_{i=1}^{n}\left(\frac{\partial a}{\partial T_i}U_T\right)^2 + \sum_{i=1}^{n}\left(\frac{\partial a}{\partial x_i}U_x\right)^2} \qquad \text{(Eq.B.8)}$$

U_T is assumed to be ±0.5K for T-type Thermocouple with Special Limits of Error (SLE) Thermocouple wire. Although the thermocouple holes were machined with ±0.025mm

tolerances, U_x is assumed to be ±0.254mm considering the position of the thermocouple tip inside the hole.

The superheat is computed as:

$$\Delta T = T_S - T_{sat} = \left(T_4 - \frac{q'' t_s}{k} \right) - T_{sat} \qquad \text{(Eq.B.9)}$$

We assume that T_{sat} is a constant

$$U_{\Delta T} = U_{T_S} = \sqrt{\left(\frac{\partial T_S}{\partial T_4} U_T \right)^2 + \left(\frac{\partial T_S}{\partial q''} U_{q''} \right)^2 + \left(\frac{\partial T_S}{\partial t_s} U_x \right)^2 + \left(\frac{\partial T_S}{\partial k} U_k \right)^2} \qquad \text{(Eq.B.10)}$$

Since t_s is the thermocouple position, the same value of U_x is used its uncertainty. The heat transfer coefficient is estimated as:

$$h = \frac{q''}{\Delta T} \qquad \text{(Eq.B.11)}$$

Therefore, U_h becomes:

$$U_h = \sqrt{\left(\frac{\partial h}{\partial q''} U_{q''} \right)^2 + \left(\frac{\partial h}{\partial \Delta T} U_{\Delta T} \right)^2} = h \sqrt{\left(\frac{U_{q''}}{q''} \right)^2 + \left(\frac{U_{\Delta T}}{\Delta T} \right)^2} \qquad \text{(Eq.B.12)}$$

Typically, a large uncertainty is introduced in U_h at low superheat due to the second term in the square root of Eq.B.12

APPENDIX C. ANALYSIS DETAILS

C.1 Viscous-Capillary Analysis for the Plain Microporous Surface

The governing equation is given by:

$$-\frac{dp_c}{dx}=\frac{q''}{\kappa h_{fg}}\left(\frac{\nu_v}{\kappa_{rv}}+\frac{\nu_l}{\kappa_{rl}}\right)-\left(\rho_l-\rho_v\right)g \qquad \text{(Eq.C.1)}$$

where v is kinematic viscosity. κ_{rv} and κ_{rl} is the relative permeabilities of the liquid and the vapor. The permeability of the microporous media, κ, can be estimated using the porosity, ε, and the particle diameter, d_p, as:

$$\kappa=\frac{\varepsilon^3}{150\left(1-\varepsilon\right)^2}d_p^2 \qquad \text{(Eq.C.2)}$$

The capillary pressure, p_c, and the relative permeabilities, κ_{rv} and κ_{rl}, can be expressed as a function of the relative liquid saturation, Se, as given in Eq.C.3-Eq.C.5. The relative liquid saturation represents the pore volume occupied by liquid over the total pore volume.

$$\kappa_{rv}=\left(1-Se\right)^2\left(1-Se^m\right) \qquad \text{(Eq.C.3)}$$

$$\kappa_{rl}=Se^n \qquad \text{(Eq.C.4)}$$

$$p_c=\sigma\left(\frac{\varepsilon}{\kappa}\right)^{1/2}f\left(Se\right) \qquad \text{(Eq.C.5)}$$

where σ is the surface tension, ε is the porosity. m and n are given as:

$$m=1+2/\lambda \qquad \text{(Eq.C.6)}$$

$$n = 3 + 2/\lambda \tag{Eq.C.7}$$

where λ is an index of pore size distribution and is determined by experiment. Udell's analysis corresponds to $\lambda = \infty$, therefore, m=1 and n=3. $f(Se)$ is given as Eq.C.8:

$$f\left(Se\right) = C_1\left(1 - Se\right) + C_2\left(1 - Se\right)^2 + C_3\left(1 - Se\right)^3 \tag{Eq.C.8}$$

Where C_1, C_2, and C_3 are constants, and given as 1.417, -2.120, and 1.263, respectively. Separating the variables in Eq.C.1 results in:

$$\frac{dp_c}{\dfrac{q''}{\kappa h_{fg}}\left(\dfrac{\nu_v}{\kappa_{rv}} + \dfrac{\nu_l}{\kappa_{rl}}\right) - \left(\rho_l - \rho_v\right) g} = -dx \tag{Eq.C.9}$$

Since all variables in the left side in Eq.C.9 are only a function of Se, it can be rewritten to Eq.C.10:

$$\int_{Se_a}^{Se_b} \frac{C_1 + 2C_2\left(1 - Se\right) + 3C_3\left(1 - Se\right)^2}{\dfrac{q''}{\kappa h_{fg}}\left(\dfrac{\nu_v}{\kappa_{rv}} + \dfrac{\nu_l}{\kappa_{rl}}\right) - \left(\rho_l - \rho_v\right) g} dSe = \frac{1}{\sigma}\left(\frac{\kappa}{\varepsilon}\right)^{1/2} \times \int_a^b dx \tag{Eq.C.10}$$

where Se_a and Se_b are the values of Se at x=a and x=b, respectively. The dryout heat flux (or vapor-layer heat flux in the present study) can be determined by finding the heat flux that results in the relative liquid saturation of zero at the bottom of the microporous coatings: the heat flux becomes Se=0 at x=0. Therefore, letting Se_a=0 and Se_b=1 as well as a=0 and b=δ, then the coating thickness, δ, that corresponds to q'' can be found by performing numerical integration the left side in Eq.C.10. The MATLAB code for the integration is shown as follows:

```
%% Working Fluid Properties

% Water
rho_v =    ;          % Vapor density[kg/m^3]
rho_l =    ;          % Liquid density [kg/m^3]
h_fg  =    ;          % Latent heat of vaporization [kJ/kg]
sigma =    ;          % Surface tension [N/m]
v_v   =    ;          % Vapor kinematic viscosity, [m2/s]
v_l   =    ;          % Liquid kinematic viscosity, [m2/s]


g     =9.81;          % Gravitational acceleration [m/s^2]

dp       =   ;        % Particle diameter [m]
epsilon  =   ;        % Porosity
K=dp^2*epsilon^3/(150*(1-epsilon)^2);   % Permeability

%% Constants of f(Se)
C1=1.417;
C2=-2.120;
C3=1.263;

%% Constants: relative permeability
m=1;
n=3;

%% Vapor-layer heat flux for very thick microporous
q_VL_thick=K*h_fg*(rho_l-rho_v)*g/v_v*(1+(v_l/v_v)^0.25)^(-4)

%% Heat flux [kW/m^2]
q=[round(q_VL_thick,2):.01:200 201:1:1000 1100:10:20000];

%% Integral: multiple-application trapezoidal rule
ff=@(Se)(C1+2*C2*(1-Se)+3*C3*(1-Se)^2)./...
    (q/(K*h_fg).*(v_v/((1-Se)^2*(1-Se^m))...
     +v_l/(Se^n))-(rho_l-rho_v)*g);

dSe=0.01;
See=[0:dSe:0.95];
sumf=0;
for ii=2:(length(See)-1)
    sumf=sumf+ff(See(ii));
end
sumf=dSe/2*(ff(See(1))+2*sumf+ff(See(length(See))));

%% Finding thickness corresponding the heat flux
delta=sumf*sigma/sqrt(K/epsilon);

%% Plot thickness vs. heat flux
loglog(delta,q)
```

C.2 Viscous-Capillary Analysis for the Patterned Microporous Surfaces

A two-dimensional geometry was considered for the simplicity of the analysis, which has one-directional straight channels through the plain.

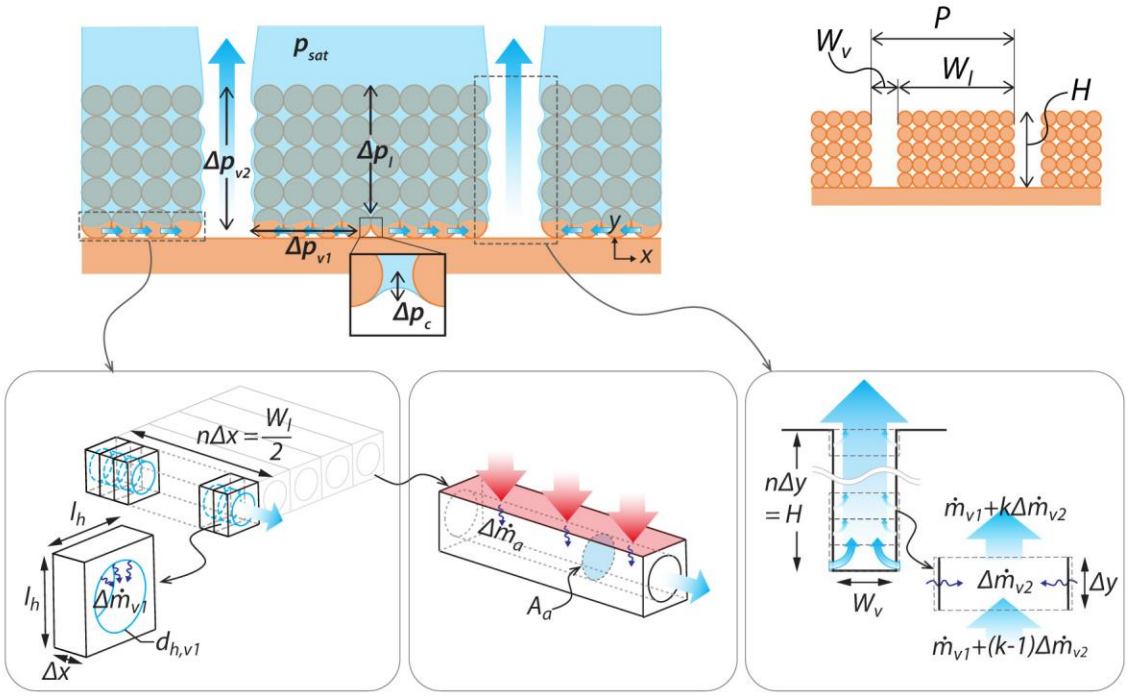

Figure C.1 – A schematic of the geometry for the analysis.

The Laplace pressure across the meniscus, or the capillary pressure, is expressed using the pressure drops of flow as:

$$\begin{aligned} p_c &= \left(p_{sat} + \Delta p_{v1} + \Delta p_{v2} + \Delta p_a\right) - \left(p_{sat} - \Delta p_l\right) \\ &= \Delta p_{v1} + \Delta p_{v2} + \Delta p_a + \Delta p_l \end{aligned} \qquad \text{(Eq.C.11)}$$

Where Δp_l is the pressure drop of the liquid flow through the microporous coatings, Δp_{v1} is the pressure drop of the vapor flow through the pores, Δp_{v2} is the pressure drop of the vapor flow through the vapor channels, and Δp_a is the acceleration pressure drop due to the phase change. The capillary pressure is given as:

$$\Delta p_c = \frac{2\sigma}{r_{eff}} \quad \text{(Eq.C.12)}$$

where σ is the surface tension, and r_{eff} is the effective pore radius. The effective pore radius is given as Eq.C.12, which is typically used in the capillary pressure estimation of the wick structure in heat pipe application for packed spherical particles (Table 3.1 in the reference[52]).

$$r_{eff} = 0.21 d_p \quad \text{(Eq.C.13)}$$

where d_p is the particle diameter. The pressure drop of liquid flow through the microporous coatings is given by Darcy's law as:

$$\Delta p_l = \frac{\mu_l \dot{m}_l \delta}{\rho_l \kappa A_l} \quad \text{(Eq.C.14)}$$

where μ_l and ρ_l is the viscosity and the density of the liquid, respectively. $\dot{m}_l$ is the mass flow rate of liquid, A_l is the projected area of liquid wicking, and δ is the thickness of the porous coatings. κ is the permeability of the microporous coatings, which can be estimated to be Eq.C.15 for packed spherical particles.

$$\kappa = \frac{d_p^2 \varepsilon^3}{150\left(1-\varepsilon\right)^2} \quad \text{(Eq.C.15)}$$

where ε is the porosity of the microporous coatings. With the two-dimensional geometry, the mass flow rate per unit area is given as:

$$\frac{\dot{m}_l}{A_l} = \frac{q''_{Bt} H}{h_{fg} W_l} \quad \text{(Eq.C.16)}$$

where h_{fg} is the latent heat of vaporization, W_l is the width of the liquid flow area, and H is the vapor channel depth, and here we assumed that the channel depth is the same as the microporous coatings thickness. q''_{Bt} is the heat flux at the major evaporation zone. By substituting Eq.C.15 into Eq.C.14, the pressure drop of the liquid flow is given as:

$$\Delta p_l = \frac{\mu_l}{\rho_l h_{fg}} \frac{HP}{\kappa W_l} q''_{Bt} \qquad \text{(Eq.C.17)}$$

The general flow pressure drop per unit length through a pipe is given as Eq.C.18 by Darcy- Weisbach equation:

$$\frac{\Delta p}{L} = 2 f_D \frac{\rho u^2}{d_h} \qquad \text{(Eq.C.18)}$$

where f_D is the friction factor, u is the flow velocity, and d_h is the hydraulic diameter of the pipe. Using f_D=16/Re for laminar flow and the Reynolds number of $(\rho u d_h)/\mu$, the pressure drop of the vapor flow through a pipe is given as:

$$\Delta p_v = \frac{128 \mu_v \dot{m}_v L}{\pi \rho_v d_v^4} \qquad \text{(Eq.C.19)}$$

where L is the flow length. For the estimation of the pressure drop through the pores, Δp_{v1}, d_{v1} is given to be the hydraulic diameter of the pores in packed spherical particles as Eq.C20.

$$d_{v1} = \frac{2\varepsilon}{3(1-\varepsilon)} d_p \qquad \text{(Eq.C.20)}$$

The total pressure drop through a single path of pores is the summation of the pressure drops per unit length, $L=\Delta x$, which is given to be:

$$\Delta p_{v1} = \sum_{k=1}^{n} \frac{128\mu_v \left(k\Delta \dot{m}_{v1}\right)\Delta x}{\pi \rho_v d_{v1}^4} = \frac{n\left(n+1\right)}{2} \times \frac{128\mu_v \Delta \dot{m}_{v1}\Delta x}{\pi \rho_v d_{v1}^4} \qquad \text{(Eq.C.22)}$$

The mass flow rate per unit length is given as:

$$\Delta \dot{m}_{v1} = \frac{q''_{Bt}}{h_{fg}} \frac{l_h P}{2n} \qquad \text{(Eq.C.23)}$$

l_h is assumed to be:

$$l_h = \left(\frac{\pi d_{v1}^2}{4\varepsilon} \right)^{1/2} \qquad \text{(Eq.C.24)}$$

By substituting Eq.C.23 and $\Delta x = W_l/(2n)$ into Eq.C22 with $n \to \infty$, the pressure drop of the vapor flow through the pores becomes:

$$\Delta p_{v1} = \frac{16}{\pi} \frac{\mu_v}{\rho_v h_{fg}} \frac{l_h P W_l}{d_{v1}^4} q''_{Bt} \qquad \text{(Eq.C.25)}$$

For the estimation of the pressure drop through the vapor channel, Δp_{v2}, the parallel plates are considered with $f_D = 24/\mathrm{Re}$. Therefore, Eq.C.18 becomes:

$$\Delta p_{v2} = \frac{48\mu_v u_{v2} L}{d_{v2}^2} = \frac{48\mu_v \dot{m}_{v2} L}{\rho_v d_{v2}^2 W_v} \qquad \text{(Eq.C.26)}$$

where d_{v2} is twice of the channel with, $2W_v$, for the parallel plates. The initial mass flow rate (per unit depth perpendicular to the given geometry), which is the vapor flow out of the pores, is given as:

$$\dot{m}_{v2,i} = \frac{Pq''_{Bt}}{h_{fg}} \qquad \text{(Eq.C.27)}$$

Due to the minor evaporation through the vapor channels, the following mass flux is added per unit length of Δy along the flow:

$$\Delta\dot{m}_{v2} = \frac{Pq''_{Sd}}{h_{fg}n} \qquad \text{(Eq.C.28)}$$

where q''_{Sd} is the heat flux through the minor evaporation zone. The total pressure drop through the vapor channel is the summation of the pressure drops that is estimated using Eq.C.26 per unit length, $L=\Delta y$, which is given to be Eq.C.29 using Eq.C.27-28

$$\Delta p_{v2} = \sum_{k=1}^{n} \frac{48\mu_v \Delta y}{\rho_v d_{v2}^2 W_v}\left(\dot{m}_{v2,i} + \frac{(k-1)}{n}\Delta\dot{m}_{v2}\right) \qquad \text{(Eq.C.29)}$$

By substituting $\Delta y=H/n$ into Eq.C29 with $n\rightarrow\infty$, the pressure drop of the vapor flow through the vapor channels becomes:

$$\Delta p_{v2} = \frac{48\mu_v PH}{\rho_v h_{fg} d_{v2}^2 W_v}\left(q''_{Bt} + \frac{q''_{Sd}}{2}\right) \qquad \text{(Eq.C.30)}$$

The acceleration pressure drop due to the phase change is given as:

$$\Delta p_a = \left(\frac{\dot{m}_a}{A_a}\right)^2 \left(\frac{1}{\rho_v} - \frac{1}{\rho_l}\right) \qquad \text{(Eq.C.31)}$$

where $\dot{m}_a$ is the mass generation rate per a single pore path and A_a is the cross-sectional area of the flow. Therefore, the ratio of them is given as:

$$\frac{\dot{m}_a}{A_a} = \frac{4 l_h P}{\pi h_{fg} d_{v1}^2} q''_{Bt} \qquad \text{(Eq.C.32)}$$

The acceleration pressure drop through the pores is only considered since the pressure drop through vapor channel is negligible.

Although the ratio between the heat flux at the major and at the minor evaporation zone is unknown, no significant difference was seen in the orders of magnitude of the pressure drops with a different ratio of the heat fluxes. In the analysis, we assumed that the heat flux at the major evaporation zone is 70% of the total heat flux.

APPENDIX D. EXAMPLE OF EXPERIMENTAL RAW DATA

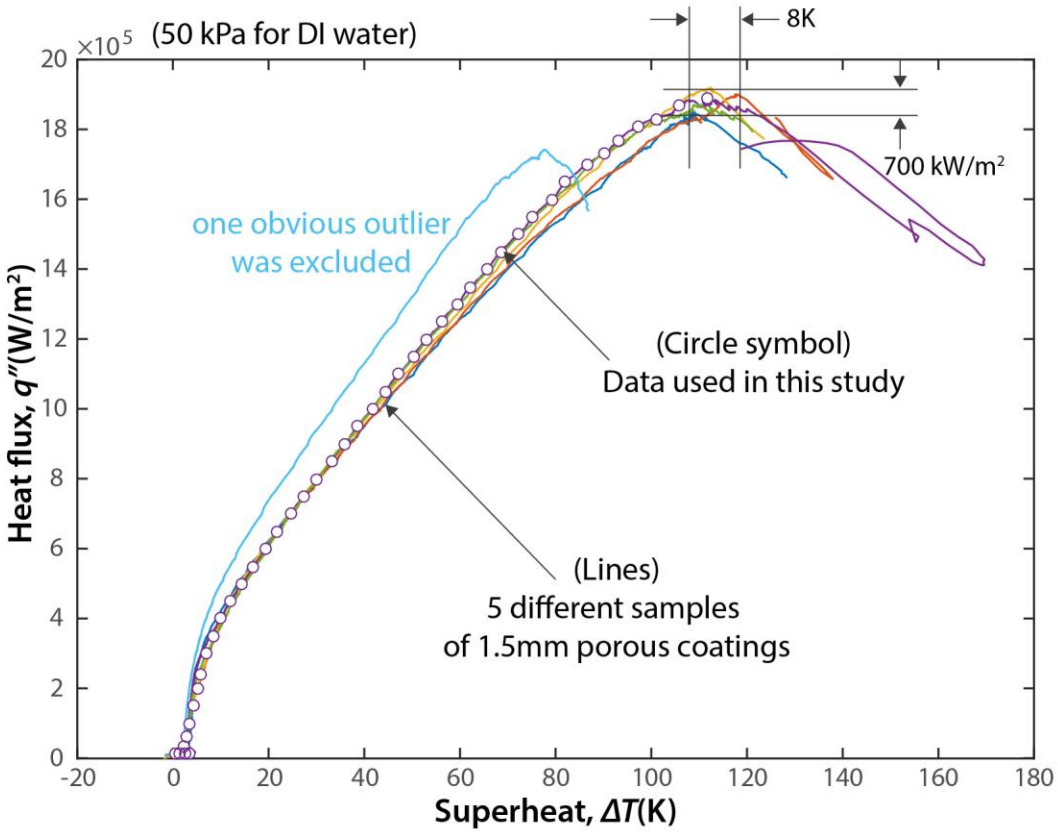

Figure D.1 – A plot of the experimental raw data of 1.5 mm porous coatings in Figure 15.

REFERENCES

1. Bergman, T.L. and F.P. Incropera, *Fundamentals of heat and mass transfer*. 2011: John Wiley & Sons.

2. Dhir, V.K., *Boiling heat transfer.* Annual Review of Fluid Mechanics, 1998. **30**: p. 365-401.

3. Attinger, D., et al., *Surface engineering for phase change heat transfer: A review.* MRS Energy & Sustainability - A Review Journal, 2014. **1**: p. null-null.

4. Barber, J., D. Brutin, and L. Tadrist, *A review on boiling heat transfer enhancement with nanofluids.* Nanoscale Research Letters, 2011. **6**.

5. Sathyanarayana, A., et al., *Pool Boiling of HFE 7200–C4H4F6O Mixture on Hybrid Micro-Nanostructured Surface.* Journal of Nanotechnology in Engineering and Medicine, 2013. **3**(4): p. 041004-041004-7.

6. Fong, R.W.L., et al., *Effects of oxidation and fractal surface roughness on the wettability and critical heat flux of glass-peened Zirconium alloy tubes*. 2003, Atomic Energy of Canada Limited, Chalk River, Ontario (Canada).

7. Ahn, H.S., et al., *Pool boiling CHF enhancement by micro/nanoscale modification of zircaloy-4 surface.* Nuclear Engineering and Design, 2010. **240**(10): p. 3350-3360.

8. O'Hanley, H., et al., *Separate effects of surface roughness, wettability, and porosity on the boiling critical heat flux.* Applied Physics Letters, 2013. **103**(2).

9. Takata, Y., et al., *Pool boiling on a superhydrophilic surface.* International Journal of Energy Research, 2003. **27**(2): p. 111-119.

10. Betz, A.R., et al., *Do surfaces with mixed hydrophilic and hydrophobic areas enhance pool boiling?* Applied Physics Letters, 2010. **97**(14).

11. Feng, B., K. Weaver, and G.P. Peterson, *Enhancement of critical heat flux in pool boiling using atomic layer deposition of alumina.* Applied Physics Letters, 2012. **100**(5).

12. Kim, H.D. and M.H. Kim, *Effect of nanoparticle deposition on capillary wicking that influences the critical heat flux in nanofluids.* Applied Physics Letters, 2007. **91**(1).

13. Chen, R., et al., *Nanowires for enhanced boiling heat transfer.* Nano letters, 2009. **9**(2): p. 548-553.

14. Forrest, E., et al., *Augmentation of nucleate boiling heat transfer and critical heat flux using nanoparticle thin-film coatings.* International Journal of Heat and Mass Transfer, 2010. **53**(1–3): p. 58-67.

15. Li, C. and G.P. Peterson, *Parametric study of pool boiling on horizontal highly conductive microporous coated surfaces.* J. Heat Transfer, 2007. **129**(11): p. 1465-1475.

16. Mori, S. and K. Okuyama, *Enhancement of the critical heat flux in saturated pool boiling using honeycomb porous media.* International Journal of Multiphase Flow, 2009. **35**(10): p. 946-951.

17. Cooke, D. and S.G. Kandlikar, *Effect of open microchannel geometry on pool boiling enhancement.* International Journal of Heat and Mass Transfer, 2012. **55**(4): p. 1004-1013.

18. Chu, K.H., et al., *Hierarchically structured surfaces for boiling critical heat flux enhancement.* Applied Physics Letters, 2013. **102**(15).

19. Rahman, M.M., E. Olceroglu, and M. McCarthy, *Role of Wickability on the Critical Heat Flux of Structured Superhydrophilic Surfaces.* Langmuir, 2014. **30**(37): p. 11225-11234.

20. Jaikumar, A. and S.G. Kandlikar, *Enhanced pool boiling for electronics cooling using porous fin tops on open microchannels with FC-87.* Applied Thermal Engineering, 2015. **91**: p. 426-433.

21. Kim, S., et al., *Effects of nano-fluid and surfaces with nano structure on the increase of CHF.* Experimental Thermal and Fluid Science, 2010. **34**(4): p. 487-495.

22. Zuber, N., *Hydrodynamic aspects of boiling heat transfer (thesis).* 1959, California. Univ., Los Angeles; and Ramo-Wooldridge Corp., Los Angeles.

23. You, S., J. Kim, and K. Kim, *Effect of nanoparticles on critical heat flux of water in pool boiling heat transfer.* Applied Physics Letters, 2003. **83**(16): p. 3374-3376.

24. Vassallo, P., R. Kumar, and S. D'Amico, *Pool boiling heat transfer experiments in silica–water nano-fluids.* International Journal of Heat and Mass Transfer, 2004. **47**(2): p. 407-411.

25. Bang, I.C. and S.H. Chang, *Boiling heat transfer performance and phenomena of Al2O3–water nano-fluids from a plain surface in a pool.* International Journal of Heat and Mass Transfer, 2005. **48**(12): p. 2407-2419.

26. Kim, H., J. Kim, and M.H. Kim, *Effect of nanoparticles on CHF enhancement in pool boiling of nano-fluids.* International Journal of Heat and Mass Transfer, 2006. **49**(25): p. 5070-5074.

27. Jo, H., et al., *A study of nucleate boiling heat transfer on hydrophilic, hydrophobic and heterogeneous wetting surfaces.* International Journal of Heat and Mass Transfer, 2011. **54**(25-26): p. 5643-5652.

28. Betz, A.R., J. Jenkins, and D. Attinger, *Boiling heat transfer on superhydrophilic, superhydrophobic, and superbiphilic surfaces.* International Journal of Heat and Mass Transfer, 2013. **57**(2): p. 733-741.

29. Cooke, D. and S.G. Kandlikar, *Pool Boiling Heat Transfer and Bubble Dynamics Over Plain and Enhanced Microchannels.* Journal of Heat Transfer-Transactions of the Asme, 2011. **133**(5).

30. Ramaswamy, C., et al., *High-speed visualization of boiling from an enhanced structure.* International journal of heat and mass transfer, 2002. **45**(24): p. 4761-4771.

31. Ramaswamy, C., et al., *Effects of varying geometrical parameters on boiling from microfabricated enhanced structures.* Journal of Heat Transfer, 2003. **125**(1): p. 103-109.

32. Ramaswamy, C., et al., *Semi-analytical model for boiling from enhanced structures.* International journal of heat and mass transfer, 2003. **46**(22): p. 4257-4269.

33. Ghiu, C.-D. and Y.K. Joshi, *Visualization study of pool boiling from thin confined enhanced structures.* International Journal of Heat and Mass Transfer, 2005. **48**(21): p. 4287-4299.

34. Launay, S., et al., *Hybrid micro-nano structured thermal interfaces for pool boiling heat transfer enhancement.* Microelectronics Journal, 2006. **37**(11): p. 1158-1164.

35. McHale, J.P., et al., *Pool Boiling Performance Comparison of Smooth and Sintered Copper Surfaces with and Without Carbon Nanotubes.* Nanoscale and Microscale Thermophysical Engineering, 2011. **15**(3): p. 133-150.

36. Dhillon, N.S., J. Buongiorno, and K.K. Varanasi, *Critical heat flux maxima during boiling crisis on textured surfaces.* Nature communications, 2015. **6**.

37. Kutateladze, S., *On the transition to film boiling under natural convection.* Kotloturbostroenie, 1948. **3**(152-158): p. 20.

38. Lienhard, J.H. and V.K. Dhir, *Hydrodynamic Prediction of Peak Pool-Boiling Heat Fluxes from Finite Bodies.* Journal of Heat Transfer-Transactions of the Asme, 1973. **95**(2): p. 152-158.

39. Kandlikar, S.G., *A theoretical model to predict pool boiling CHF incorporating effects of contact angle and orientation.* Journal of Heat Transfer-Transactions of the Asme, 2001. **123**(6): p. 1071-1079.

40. Chu, K.H., R. Enright, and E.N. Wang, *Structured surfaces for enhanced pool boiling heat transfer.* Applied Physics Letters, 2012. **100**(24).

41. Ahn, H.S., et al., *The effect of water absorption on critical heat flux enhancement during pool boiling.* Experimental Thermal and Fluid Science, 2012. **42**: p. 187-195.

42. Udell, K.S., *Heat transfer in porous media considering phase change and capillarity—the heat pipe effect.* International Journal of Heat and Mass Transfer, 1985. **28**(2): p. 485-495.

43. Lu, S.M. and R.H. Chang, *Pool Boiling from a Surface with a Porous Layer.* AIChE Journal, 1987. **33**(11): p. 1813-1828.

44. Polezhaev, Y.V. and S.A. Kovalev, *Modelling heat transfer with boiling on porous structures.* Thermal engineering, 1990. **37**(12): p. 617-621.

45. Chang, J.Y. and S.M. You, *Boiling heat transfer phenomena from microporous and porous surfaces in saturated FC-72.* International Journal of Heat and Mass Transfer, 1997. **40**(18): p. 4437-4447.

46. Li, C., G.P. Peterson, and Y. Wang, *Evaporation/boiling in thin capillary wicks (I) - Wick thickness effects.* J. Heat Transfer, 2006. **128**(12): p. 1312-1319.

47. Rahman, M.M., J. Pollack, and M. McCarthy, *Increasing Boiling Heat Transfer using Low Conductivity Materials.* Scientific reports, 2015. **5**.

48. Jones, B.J., J.P. McHale, and S.V. Garimella, *The Influence of Surface Roughness on Nucleate Pool Boiling Heat Transfer.* J. Heat Transfer, 2009. **131**(12).

49. Fukusako, S., T. Komoriya, and N. Seki, *An Experimental-Study of Transition and Film Boiling Heat-Transfer in Liquid-Saturated Porous Bed.* J. Heat Transfer, 1986. **108**(1): p. 117-124.

50. Kaviany, M., *Principles of heat transfer in porous media*. 2nd ed. 1995: Springer-Verlag.

51. Liter, S.G. and M. Kaviany, *Pool-boiling CHF enhancement by modulated porous-layer coating: theory and experiment.* International Journal of Heat and Mass Transfer, 2001. **44**(22): p. 4287-4311.

52. Faghri, A., *Heat Pipe Science and Technology*. 1995: Taylor & Francis Group.

53. Hsu, Y.Y., *On the Size Range of Active Nucleation Cavities on a Heating Surface.* Journal of Heat Transfer, 1962. **84**(3): p. 207-213.

54. Kruse, C., et al., *Secondary pool boiling effects.* Applied Physics Letters, 2016. **108**(5): p. 051602.

55. Webb, R.L., *Nucleate boiling on porous coated surfaces.* Heat Transfer Engineering, 1983. **4**(3-4): p. 71-82.

56. Sarangi, S., J.A. Weibel, and S.V. Garimella, *Effect of particle size on surface-coating enhancement of pool boiling heat transfer.* International Journal of Heat and Mass Transfer, 2015. **81**: p. 103-113.

57. Jun, S., et al., *Enhancement of pool boiling heat transfer in water using sintered copper microporous coatings.* Nuclear Engineering and Technology, 2016. **48**(4): p. 932-940.

58. Brooks, R.H. and A.T. Corey, *Properties of porous media affecting fluid flow.* Journal of the Irrigation and Drainage Division. **92**(2): p. 61-90.

59. Mughal, M.P. and O.A. Plumb, *An experimental study of boiling on a wicked surface.* International Journal of Heat and Mass Transfer, 1996. **39**(4): p. 771-777.

60. Stubos, A.K. and J.M. Buchlin, *Enhanced cooling via boiling in porous layers: The effect of vapor channels.* Journal of Heat Transfer-Transactions of the Asme, 1999. **121**(1): p. 205-210.

61. Wu, W., et al., *Pool boiling heat transfer and simplified one-dimensional model for prediction on coated porous surfaces with vapor channels.* International Journal of Heat and Mass Transfer, 2002. **45**(5): p. 1117-1125.

62. Nishikawara, M. and H. Nagano, *Parametric experiments on a miniature loop heat pipe with PTFE wicks.* International Journal of Thermal Sciences, 2014. **85**: p. 29-39.

63. Westwater, J. and J. Santangelo, *Photographic study of boiling.* Industrial & Engineering Chemistry, 1955. **47**(8): p. 1605-1610.

64. Fritz, W., *Berechnung des maximalvolume von dampfblasen.* Phys. Z., 1935. **36**: p. 379-388.

65. Cole, R. and W. Rohsenow. *Correlation of bubble departure diameters for boiling of saturated liquids*. in *Chem. Eng. Prog. Symp. Ser*. 1969. 211 213.

66. Cole, R., *Bubble frequencies and departure volumes at subatmospheric pressures.* AIChE Journal, 1967. **13**(4): p. 779-783.

67. Ivey, H., *Relationships between bubble frequency, departure diameter and rise velocity in nucleate boiling.* International Journal of Heat and Mass Transfer, 1967. **10**(8): p. 1023-1040.

68. Kandlikar, S., *Controlling bubble motion over heated surface through evaporation momentum force to enhance pool boiling heat transfer.* Applied Physics Letters, 2013. **102**(5): p. 051611.

69. Bai, L., et al., *Pool boiling with high heat flux enabled by a porous artery structure.* Applied Physics Letters, 2016. **108**(23): p. 233901.

70. Lee, D., et al., *Multilayers of oppositely charged SiO2 nanoparticles: Effect of surface charge on multilayer assembly.* Langmuir, 2007. **23**(17): p. 8833-8837.

71. Schrader, M.E., *Ultrahigh vacuum techniques in the measurement of contact angles. III. Water on copper and silver.* The Journal of Physical Chemistry, 1974. **78**(1): p. 87-89.

72. Raj, R., S.C. Maroo, and E.N. Wang, *Wettability of graphene.* Nano letters, 2013. **13**(4): p. 1509-1515.

73. Szyszka, D. and W. Szczepański, *Contact angle of copper-bearing shales using the sessile drop and captive bubble methods in the presence of selected frothers.* Mining Science, 2015. **22**.

74. Boyes, A. and A. Ponter, *Measurement of contact angles encountered during distillation of binary liquids on a copper surface.* Journal of Chemical and Engineering Data, 1970. **15**(2): p. 235-238.

75. Adkins, D.R. and R.C. Dykhuizen, *Procedures for Measuring the Properties of Heat-Pipe Wick Materials.* Energy Environment Economics: 28th Intersociety Energy Conversion Engineering Conference Proceedings (Iecec-93), Vol 2, 1993: p. 911-917.

76. Holley, B. and A. Faghri, *Permeability and effective pore radius measurements for heat pipe and fuel cell applications.* Applied Thermal Engineering, 2006. **26**(4): p. 448-462.

77. Powell, R., C.Y. Ho, and P.E. Liley, *Thermal conductivity of selected materials*. 1966, DTIC Document.

78. *International Association for the Properties of Water and Steam*. [cited 2018 February 1]; Available from: http://www.iapws.org/.

79. Mudawar, I. and T.M. Anderson, *Parametric Investigation Into the Effects of Pressure, Subcooling, Surface Augmentation and Choice of Coolant on Pool Boiling in the Design of Cooling Systems for High-Power-Density Electronic Chips.* Journal of Electronic Packaging, 1990. **112**(4): p. 375-382.